E.O. Paton Electric Welding Institute of the National Academy of Science of Ukraine
International Association «Welding»

The Paton Welding Journal

12
2023

International Scientific-Technical and Production Journal ◊ Founded in January 2000 (12 Issues Per Year)

EDITORIAL BOARD

Editor-in-Chief
I.V. Krivtsun — E.O. Paton Electric Welding Institute, Kyiv, Ukraine

Deputy Editor-in-Chief
S.V. Akhonin — E.O. Paton Electric Welding Institute, Kyiv, Ukraine

Deputy Editor-in-Chief
L.M. Lobanov — E.O. Paton Electric Welding Institute, Kyiv, Ukraine

Editorial Board Members

O.M. Berdnikova	E.O. Paton Electric Welding Institute, Kyiv, Ukraine
Chang Yunlong	School of Materials Science and Engineering, Shenyang University of Technology, Shenyang, China
V.V. Dmitrik	NTUU «Kharkiv Polytechnic Institute», Kharkiv, Ukraine
Dong Chunlin	Guangzhou Jiao Tong University, Guangzhou, China
M. Gasik	Aalto University Foundation, Finland
A. Gumenyuk	Bundesanstalt für Materialforschung und –prüfung (BAM), Berlin, Germany
V.V. Knysh	E.O. Paton Electric Welding Institute, Kyiv, Ukraine
V.M. Korzhyk	E.O. Paton Electric Welding Institute, Kyiv, Ukraine
V.V. Kvasnytskyi	NTUU «Igor Sikorsky Kyiv Polytechnic Institute», Kyiv, Ukraine
Yu.M. Lankin	E.O. Paton Electric Welding Institute, Kyiv, Ukraine
O.V. Makhnenko	E.O. Paton Electric Welding Institute, Kyiv, Ukraine
S.Yu. Maksymov	E.O. Paton Electric Welding Institute, Kyiv, Ukraine
Yupiter HP Manurung	Smart Manufacturing Research Institute, Universiti Teknologi MARA, Shah Alam, Malaysia
M.O. Pashchin	E.O. Paton Electric Welding Institute, Kyiv, Ukraine
V.D. Poznyakov	E.O. Paton Electric Welding Institute, Kyiv, Ukraine
U. Reisgen	Welding and Joining Institute, Aachen, Germany
I.O. Ryabtsev	E.O. Paton Electric Welding Institute, Kyiv, Ukraine
V.M. Uchanin	Karpenko Physico-Mechanical Institute, Lviv, Ukraine
Yang Yongqiang	South China University of Technology, Guangzhou, China
Executive Director	O.T. Zelnichenko, International Association «Welding», Kyiv, Ukraine

Address of Editorial Board
E.O. Paton Electric Welding Institute, 11 Kazymyr Malevych Str., 03150, Kyiv, Ukraine
Tel./Fax: (38044) 205 23 90, E-mail: journal@paton.kiev.ua, patonpublishinghouse@gmail.com
https://patonpublishinghouse.com/eng/journals/tpwj

State Registration Certificate 24933-14873 ПР from 13.08.2021
ISSN 0957-798X, DOI: http://dx.doi.org/10.37434/tpwj

Subscriptions, 12 issues per year:
$384 — annual subscription for the printed (hard copy) version, air postage and packaging included;
$312 — annual subscription for the electronic version (sending issues in pdf format or providing access to IP addresses).

Representative Office of «The Paton Welding Journal» in China:
China-Ukraine Institute of Welding, Guangdong Academy of Sciences
Address: Room 210, No. 363 Changxing Road, Tianhe, Guangzhou, 510650, China.
Zhang Yupeng, Tel: +86-20-61086791, E-mail: patonjournal@gwi.gd.cn

The content of the Journal includes articles received from authors from around the world in the field of welding, cutting, cladding, soldering, brazing, coating, 3D additive technologies, electrometallurgy, material science, NDT and selectively includes translations into English of articles from the following journals, published in Ukrainian:
- Automatic Welding (https://patonpublishinghouse.com/eng/journals/as);
- Electrometallurgy Today (https://patonpublishinghouse.com/eng/journals/sem);
- Technical Diagnostics & Nondestructive Testing (https://patonpublishinghouse.com/eng/journals/tdnk).

© E.O. Paton Electric Welding Institute of NASU, 2023
© International Association «Welding» (Publisher), 2023

CONTENTS

ORIGINAL ARTICLES

*Translated Article(s) from “Automatic Welding”, No. 11, 2023.

**Translated Article(s) from “Electrometallurgy Today”, No. 4, 2023.

DOI: https://doi.org/10.37434/tpwj2023.12.01

DEVELOPMENT OF PLASMA-ARC TECHNOLOGIES OF SPHERICAL GRANULE PRODUCTION FOR ADDITIVE MANUFACTURING AND GRANULE METALLURGY

V.M. Korzhyk, D.V. Strohonov, O.M. Burlachenko, O.M. Voitenko, D.V. Kunitskyi

E.O. Paton Electric Welding Institute of the NASU
11 Kazymyr Malevych Str., 03150, Kyiv, Ukraine

ABSTRACT

The technological and structural properties of spherical granules and the peculiarities of their production processes using industrial technologies of gas atomization, plasma rotating electrode process and plasma-arc atomization of neutral and current-carrying wires and rods are considered. It was found that among the considered methods of obtaining spherical granules, the most promising in terms of productivity, energy efficiency and simplicity of the equipment used is the method of plasma-arc atomization, which, due to the presence of a large number of technological and structural parameters of the process, allows adjusting the particles size distribution and technological properties of the granules in a wide range. Experimental studies have shown that the particles size distribution, shape factor and technological properties of granules from titanium alloys and stainless steel obtained by plasma-arc atomization of current-carrying wire materials at the E.O. Paton Electric Welding Institute of the NAS of Ukraine, together with LLC R&D PLAZER Center, are at the level of the best foreign analogues. A promising direction of increasing the energy efficiency and productivity of the process of obtaining spherical granules for additive manufacturing and granule metallurgy using the technology of plasma-arc atomization of current-carrying rods with a diameter of more than 50 mm at reverse polarity by plasma trons with a hollow copper anode is proposed.

KEYWORDS: plasma-arc atomization of current-carrying wires and rods, spherical granules, additive manufacturing, selective and direct laser melting and sintering, granule metallurgy

INTRODUCTION

Tendencies in the progress of modern industry in the leading world countries showed that further advances in aerospace, ship-building, power, chemical and biomedical industries are impossible without development and production of new special materials with specified properties and their processing technologies, primarily Additive Manufacturing (AM) [1]. Among the most widely applied AM technologies one should note Bed Deposition technology, which includes the processes of selective and direct laser melting and sintering (Selective Laser Melting (SLM) and Selective Laser Sintering (SLS), DMLS) and Electron Beam Melting (EBM); Direct Energy Deposition technology — a direct energy deposition method, including the processes of laser deposition (Direct Metal Deposition (DMD) and Laser Engineered Net Shaping (LENS) and cold gas-dynamic spraying (Cold Spraying (CS)), and the technology of precision workpiece manufacturing with minimal machining allowance, using the compacting methods of granule metallurgy — Hot Isostatic Pressing (HIP) and oth.

All these methods mainly use specialized spherical granules as the consumable material for forming additive layers and granule composition. These granules should satisfy strict requirements, namely they should have a high degree of sphericity in the absence of satellites and other defects [2, 3], and a certain their size distribution, which for SLM and DMLS processes should be in the range of 15–63 μm, for CS — 15–45 μm, for SLS — 15–80 μm, for EBM — 45–106 μm, for LENS and DMD — 45–150 μm, and for HIP technology — 106–250 μm. Such granules should have minimal porosity and stable chemical and phase composition.

At present, gas atomization is the most widespread technology to produce the granules for additive manufacturing [4]. A certain share in these processes belongs to plasma-arc technologies, featuring a number of advantages [5]. Significant expansion of additive manufacturing application and its transition to a new technological level requires new technologies of producing consumable materials, meeting a number of criteria by their quality, technological characteristics, productivity, cost, etc. In this connection, this work is aimed at solving the following tasks:

- conducting a critical review of the available technologies of producing spherical granules for additive manufacturing and promising directions of their development;
- substantiation of the effectiveness and analysis of new avenues of development of plasma-arc technologies and equipment for producing spherical granules for additive manufacturing and granule metallurgy;

Copyright © The Author(s)

● description of new results in producing spherical granules by plasma-arc atomization of wire materials, as well as rods and large-sized ingots.

REVIEW OF THE AVAILABLE TECHNOLOGIES OF PRODUCING SPHERICAL GRANULES FOR ADDITIVE MANUFACTURING

The main technologies of producing spherical granules for additive manufacturing include: gas atomization (GA) of the melt by inert gas (Free Fall Gas atomization (FFGA), Close-coupled gas atomization (CCGA), Electrode Induction Gas Atomization (EIGA)) and technologies of plasma atomization of wires and rods (Plasma Rotating Electrode Process (PREP) and Plasma Atomization (PA)).

At present GA in the most widely accepted method to produce spherical granules from different metals and alloys for AM. In GA method (Figure 1) the initial material is melted in the shielding atmosphere (vacuum or inert gas) or in air (at open furnace melting).

Then, the produced melt is poured through the atomizer, where the melt flow is fragmented by a flow of high-velocity inert gas (nitrogen, helium, argon), which breaks up the melt into fine drops, which cool down and solidify penetrating inside the atomization chamber, and the dimensions of which can be determined from the following relationship [7]:

$$D_p = \frac{\mathrm{We} \cdot \sigma}{\rho \cdot U^2}, \quad (1)$$

where D_p is the mean particle size, μm; σ is the surface tension force, N/m^2; ρ is the liquid density, kg/m^3; U^2 is the relative velocity between gas and particle, m/s; We is the Weber criterion.

In work [8] it is shown that EIGA atomization at inductor power of 50–70 kW, electrode rotation speed of 15–40 °C/s and atomization pressure of 5–8 MPa allows producing spherical granules from Ti–6Al–4V titanium alloy of 1–400 μm size. Here, the average size of the granules was d_{50} = 145–190 μm, where up to 50 wt.% was made up by granules of 50–180 μm size. It should be also noted that at pressure rise up to 7–8 MPa, the quantity of satellites on individual granules is greatly increased, as a result of individual particles of different size colliding with each other during atomization. Similar results were obtained in [9], where studies of the size distribution of particles from Ti–45Al–2Nb–2Mn titanium alloy, produced by the technology of electric arc melting of the ingot (arc current of 475 A) and further melt atomization at atomization pressure of 5.5 MPa showed that the average granule diameter is d_{50} = 143–168 μm, and less than 35 % of the granules are of < 100 μm size, desirable for AM. The authors [10] note that at inductor power of 240 kW and atomization pressure of 5 MPa at argon flow rate of 18 m^3/min, the productivity of the abovementioned process can be up to 10–75 kg/h for Ti–6Al–4V titanium alloy, and the coefficient of sphericity is not more than 0.83 on average. Here also gas entrapment occurs during granule solidification in GA, which leads to porosity in these granules. Such entrapped pores can greatly increase porosity in parts, made by AM technology, which may reach 0.63 vol.% [11], where even further HIP treatment allows only reducing the pore size and number of pores, but not completely eliminating gas porosity. Thus, despite the high productivity of GA process, the obtained granules are characterized by relatively low coefficient of sphericity, presence of a large number of satellites, and argon-induced porosity, but the particle size distribution of the granules lies in a wide range, where only a small portion is the interval suitable for application in AM.

A wide array of plasma-arc technologies of wire and rod atomization, among which we can highlight PREP and PA methods, belongs to another kind of widely-accepted technologies of producing spherical granules for additive technologies.

During the PREP process the electrode to be atomized is melted by the plasma arc. Under the impact of an off-center force the molten metal spreads radial-

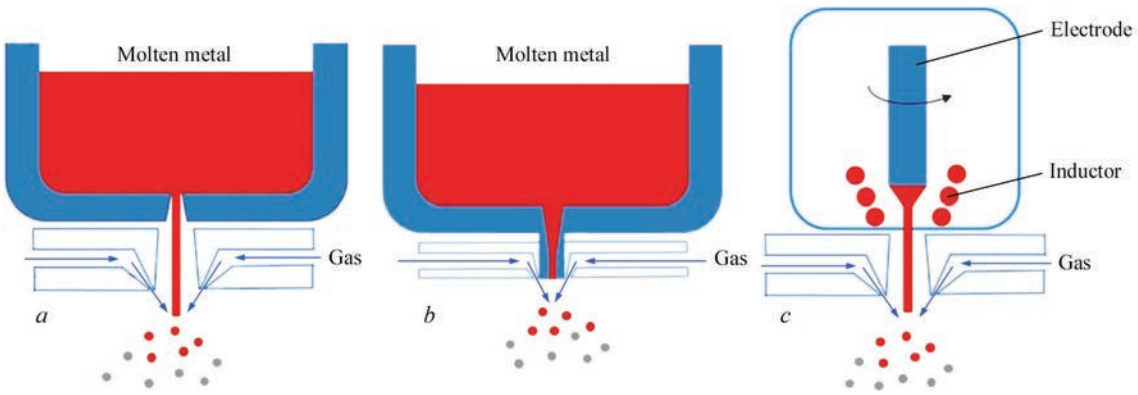

Figure 1. Technological scheme of GA process variants: *a* — FFGA; *b* — FFGA; *c* — EIGA [6]

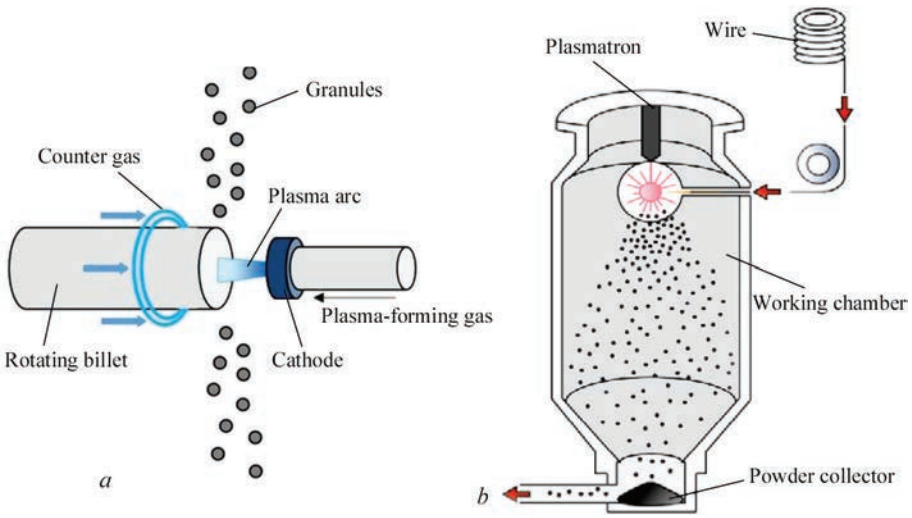

Figure 2. Technological schemes of the processes of plasma-arc atomization of wires and rods: PREP (*a*) and PA (*b*) [16]

ly, forming fine drops, and after that it solidifies into spherical granules, due to the surface tension forces (Figure 2, *a*).

It is known that the billet rotation speed has the greatest influence on the particle size distribution of the granules in the above process [12], where dimensions of atomized granules can be calculated from the following equation:

$$D_p = \frac{K}{\omega} \cdot \sqrt{\frac{\sigma}{\rho \cdot D}}, \qquad (2)$$

where D_p is the mean particle size, μm; σ is the surface tension force, N/m^2; ρ is the liquid density, kg/m^3; ω is the billet rotation speed, rpm; D is the billet diameter, m; K is the correction factor.

In the general case the atomization process is conducted at super high speeds of electrode rotation (up to 9000–25000 rpm), which allows regulation of the particle size distribution in a broad range of 50 to 500 μm. In work [13] it is shown that increase of the billet rotation speed from 9000 to 23000 rpm at PREP atomization of an electrode from Ti–6Al–4V titanium alloy of 55 mm diameter at plasmatron power of 75 kW, allows reducing the average diameter of the granules from d_{50} = 320 to 127 μm. However, there exist considerable difficulties of producing the fine fraction of <75 μm, the proportion of which is not more than 10 wt.%, and which is widely used in additive technology area. That is, the main limitation for PREP is the fact that the available applied rotation speed is not suitable for forming fine granules, which points to a pressing need for designing and producing equipment with a higher speed of electrode rotation. Significant technological difficulties are also encountered in the process of manufacturing the precision billet for atomization, most often using vacuum-induction melting technology, and further machining of the billet. Other drawbacks are impossibility of manufacturing billets from materials of a high hardness and brittleness (Cr–Mo–Fe, Fe–Al, Ni–Al, etc. alloying systems), insufficiently efficient utilization of billet material (stub length is not less than 5 cm on average), low productivity of the process, etc.

A simpler and technologically accessible method of such atomization is plasma atomization of neutral wires and rods of a small diameter, called Plasma Atomization (PA), where melting and dispersion of the material of these wires is caused by the energy and pressure of the plasma jet, generated by three plasmatrons (Figure 2, *b*). It is shown in [14] that the above process can have at least eight adjustable technological and structural parameters of the process, which allow regulation of the particles size distribution of the granules. Here, the granule size can be calculated, using the following equation:

$$D_p = \frac{3.35 \cdot d_n^2}{Q\left(1 + 0.00367 \cdot T\right)} \cdot \sqrt{\frac{d_{dw} \cdot \sigma}{\rho}}, \qquad (3)$$

where Q is the flow rate of plasma-forming gas, m^3/s; d is the plasmatron nozzle diameter, m; T is the mass average temperature of the plasma jet at the nozzle edge, K; d_w is the wire diameter, mm; ρ is the liquid density, kg/m^3; σ is the surface tension force, N/m.

For instance, by changing the plasma-forming gas supply volume, it is possible to change the kinetic energy of the plasma jet, leading to greater or smaller refinement of the melt drops, while change of current supplied to the plasmatron, allows adjustment of the atomized electrode melting rate and volume of the liquid forming at its edge, etc. It should be also taken into account that increase of the atomized electrode diameter, on the one hand, leads to increase of the process productivity, and on the other hand, to lowering of the amount of fine granule fraction of < 80

μm, as at application of large-diameter wires and rods the mass of the melt coming to the atomization zone is increased, and intensity of fragmentation of the initial drops is decreased. Researchers [15, 16] showed that application of a system of three plasmatrons of the total power of 83 kW and plasma-forming gas flow rate of 18–22 m^3/h, allows producing spherical granules from 1.6 mm Ti Grade 2 titanium wire in a rather broad range of 10–300 μm, with average diameter of d_{50} = 189 μm, where O_2 oxygen content is below 0.055 %. The granules are characterized by a minimal number of defective particles, which is not more than 1 wt.% in both the cases, and their porosity is not more than 0.08 vol.%. It should be noted, however, that the maximal productivity of the process for titanium alloys is not more than 1.5 kg/h is the general case.

Critical analysis of the structural, technological and technical-economic characteristics of spherical granules and available technologies of their manufacture showed the following. Presence of a large number of satellites and irregularly-shaped particles, lower coefficient of sphericity for GA technology leads to a difference in some technological characteristics of the granules, compared to PA and PREP. The abovementioned defects create the conditions under which the GA granules "cling" to each other at their mutual displacement (powder feed), which greatly worsens the fluidity values (particularly for the fine fraction of <63 μm), and leads to defect formation in the deposited layers. Intragranular argon-induced porosity for GA granules is impossible to remove by HIP in some cases. In other cases at further heat treatment of the parts the gas opens up the regions in which it is trapped as a result of material heating in the single-phase area, and porosity with ~0.1 % volume fraction forms. Pore opening leads to significant lowering of the values of ultimate strength, impact toughness and other mechanical characteristics of the parts, which are formed by layer-by-layer deposition. Such a microstructural defect is inadmissible for such critical parts as turbine discs, nozzle path parts, etc. Here, the PREP and PA technologies are characterized by a practically complete absence of gas porosity in the granules. PREP and PA methods also feature granule crystallization at super high cooling rates, creating the conditions for formation of a microcrystalline (and in some cases nanocrystalline) structure, which has a positive effect on the mechanical properties of the products made from them. Also important is the fact that for GA process the gas-to-metal ratio (GMR) [17] (flow rate of atomizing gas (argon) required to produce 1 kg of powder) can be from 26 to 110, and for PA and GA processes it is not higher than 8 (for Ti–6Al–4V). PREP equipment operation runs into considerable difficulties related to producing a fine fraction of <100 μm. To achieve more than 50 wt.% yield of the abovementioned fraction, it is necessary to significantly increase the billet rotation speed (more than 30000 rpm), which even more complicates the already not at all simple kinematic diagram of the unit (for lowering the vibration level, designing complex bearing systems, etc). We can also include here the difficulties, associated with producing a cylindrical billet of precise dimensions, which has to be polished with a high precision. At present, the scopes of producing the spherical granules by PA technology do not satisfy the needs of additive manufacturing of products, because of its low productivity, leading to overpriced powders, as well as delays in delivery times. Therefore, it is rational to consider this process now only for use under laboratory conditions, when manufacturing small test batches of powder.

This leads to the conclusion that the technology of plasma atomization has a significant potential for further development and practical application in spherical granule manufacturing. One of its variants is the process of plasma-arc atomization of current-carrying wire materials [14]. The above process is characterized by a higher productivity level [18], which can be up to 12–16 kg/h, and simplicity and mobility of the equipment, which allows application of a wide range of standard consumable materials from solid and flux-cored wires and rods; a large number of technological and structural parameters, permitting regulation of the particle size distribution in a broad range of 15–315 μm. Here, the amount of <100 μm fraction can be up to 90 wt.%.

PWI DEVELOPMENTS IN THE FIELD OF PLASMA-ARC TECHNOLOGIES OF PRODUCING SPHERICAL GRANULES FOR ADDITIVE TECHNOLOGIES. NEW DIRECTIONS IN TECHNOLOGY AND EQUIPMENT DEVELOPMENT

In order to increase the efficiency of the processes of manufacturing spherical granules with the specified particle size distribution and sphericity parameters, at PWI they are currently being developed in two main areas of technology and equipment for:

- plasma-arc atomization of wire materials of 0.8–3.5 mm diameter (solid and composite, for instance with a metal sheath and powder core);
- plasma-arc atomization of rods and ingots of up to 50 mm and larger diameter.

The main technological variants for implementation of the first group of technologies are shown in Figure 3, *a, b*. Here melting of the current-carrying

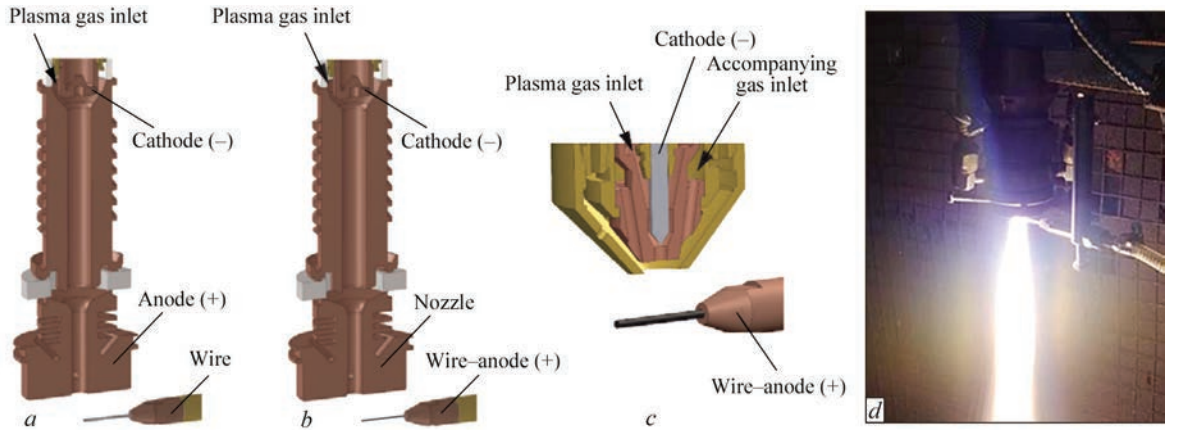

Figure 3. Scheme of the process of plasma-arc atomization of neutral wire (*a*), current-carrying wire without accompanying flow (*b*), current-carrying wire with accompanying gas flow (*c*) and appearance of the atomization process (*d*)

wire-anode, fed into the zone of high-velocity plasma jet, and further dispersion of the melt from the wire edge, are performed. The arc runs between the non-consumable tungsten cathode and current-carrying wire-anode, fed behind the plasmatron nozzle edge, and in the case of neutral wire atomization — between the cathode and plasmatron anode. The working (plasma-forming) gas coming to the working chamber is heated by the electric arc and flows out of the nozzle in the form of a plasma jet.

Results of analysis of energy efficiency and productivity of the processes of plasma-arc atomization of the neutral and current-carrying wires, in the case of atomization of titanium wire of Ti Grade2 at plasma arc power of 15 kW confirmed [19] that atomization of current-carrying wire allows increasing the wire heating efficiency more than 4 times (η = 17 and 4 %, respectively) relative to the method of neutral wire atomization, which in its turn allows increasing the process productivity from 1.5 to 12 kg/h (for titanium wire of Ti Grade2), and energy efficiency up to 6 times. However, despite the relatively low productivity, the method of neutral wire atomization is still widely used in PA technology to produce high-quality commercial spherical powders from reactive, refractory and other high-alloyed metals and alloys (AP&C, Pyrogenesis, Canada [20]).

Note that the method of plasma-arc atomization of current-carrying wire without accompanying gas application can provide a high productivity of the atomization process, which at 20–25 kW power can be equal to 10–12 kg/h for tungsten wire. However, a significant disadvantage of the above process is a wide size distribution of the atomized particles in the range of 40 to 1000 μm [21].

A further development of this process was designing and producing serial UN-126 and KT-088 (PWI) [22] and PLAZER 30-PL-W units (Scientific & Production Center PLAZER, Ukraine) [23], where the abovementioned disadvantages was eliminated by application of an accompanying gas flow (Figure 3, *c*). The accompanying gas flow, directed coaxially to the plasma one, forms the configuration of the latter, promotes its compression and thus reduces the angle of opening of the atomized particle plume, increases the outflow velocity and dynamic pressure of the plasma jet, which in its turn creates the conditions for producing the optimal particle size distribution and chemical composition of the dispersed phase. The data obtained by the results of mathematical modeling [24], showed (Figure 4) that the submerged jet flowing into the atmosphere, rather quickly expands, while mixing intensively with the external gas atmosphere. Plasma jet blowing by a circular laminar flow of cold gas of

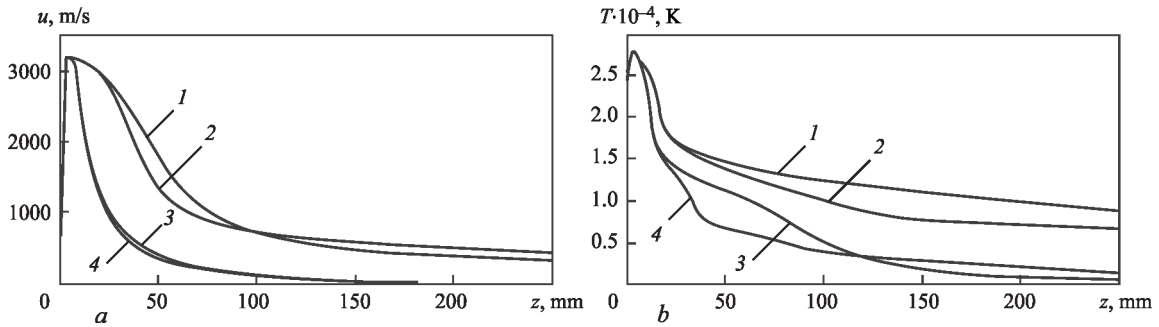

Figure 4. Longitudinal changes of velocity *u* (*a*) and temperature *T* (*b*) of argon plasma flowing out into argon (*1*, *3*) and air (*2*, *4*) atmosphere in different modes of plasmatron operation (current *I* = 200 A), plasma-forming gas flow rate Q_{pl} = 2 m³/h): *1*, *2* — accompanying gas flow rate Q_{ac} = 20 m³/h for argon and air, respectively; *3*, *4* — Q_{ac} = 0 m³/h [24]

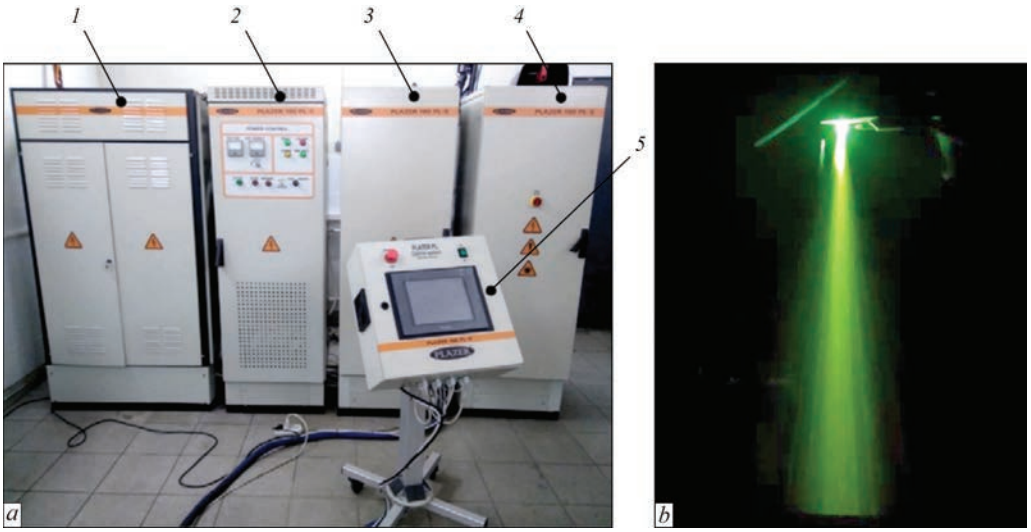

Figure 5. Appearance of PLAZER 50-PL-W laboratory unit (*a*) and two-phase plasma jet (*b*): *1* — transformer power source of the main arc; *2* — thyristor electric drive; *3* — transformer power source of pilot arc; *4* — control and gas preparation cabinet; *5* — mobile operator console with touch panel

the same composition as the plasma-forming one prevents the plasma jet expansion. Here, the turbulence is partially damped by the surrounding circular flow, and the jet energy and pulse are preserved at greater distances than for the submerged jet.

Increase of the velocity of plasma jet outflow in the zone of wire location promotes an increase of gas-dynamic pressure of the jet on the wire edge and transition from vibrational breakup, We = 8–12, and bag breakup, 12 < We < 50, to the mechanism of bag-and-stamen breakup, 50 < We > 100. Here, the intensity of breakup of the melt drops forming at the current-carrying wire edge at its melting, is significantly increased [25]:

$$\mathrm{We} = \frac{\rho_g \cdot u_{rel}^2 \cdot d_p}{\sigma}, \qquad (4)$$

where ρ_g is the gas phase density, kg/m^3; u^2_{rel} is the relative speed between the gas phase and the particle, m/s; d_p is the particle diameter, m; σ is the force of the drop surface tension, N/m.

Experimental data [14] showed that use of accompanying gas flow allows significant reduction of maximal drop dimensions from d_{90} = 1000 to 315 μm, which enables an essential increase of the amount of the fraction suitable for use in AM and granule metallurgy technologies.

Over the recent years development of this technology of plasma-arc atomization consisted in solving tasks related mainly to extension of service life of plasmatron internal parts, improvement of productivity and efficiency of heating and of atomization material utilization. For this purpose, the Scientific & Production Center PLAZER, Ltd. designed and manufactured an experimental-production unit PLA-

Table 1. PLAZER-50-PL-W unit specification

Parameter	Value
Consumed power, kW, not more than	50
Voltage of 50 Hz three-phase AC mains, V	380
Open-circuit voltage, V	160
Range of working current adjustment, A	100–500
Range of working voltage adjustment, V	30–100
Duty cycle, %	100
Air flow rate at 0.6 MPa pressure, nm^3/h	15–60
Argon or helium flow rate at 0.1 MPa pressure, nm^3/h	1–3
Wire feed rate, m/min	2–15
Plasmatron cooling	Air or water
Service life of plasmatron nozzle and cathode, h (machine time)	Not less than 100
Cooling water pressure, MPa	0.3–0.5
Cooling water flow rate, nm^3/h	0.4–0.6
Diameters of applied wire materials, mm	1.0–2.4
Control type	Automated
Controller type	PLC

ZER 50-PL-W (Figure 5), which incorporated a new design of the plasmatron with water cooling and optimized geometry of the nozzle part of reduced overall dimensions, which allowed the abovementioned equipment power to be increased from 30 to 50 kW (Table 1) [18].

This, in its turn, allowed increasing the process productivity to 16–18 kg/h, and intensifying the processes of dispersion of the melt forming at the wire edge. It should be also noted that power increase becomes particularly relevant for the case of flux-cored wire atomization, where increase of flux-cored wire diameter from 1.6 to 2.4 mm and more allows greatly increasing the wire FF (up to 40 %) and, the degree of granule alloying, respectively, but requires ensuring a proper degree of metallurgical interaction of the components, present in the flux-cored wire composition, which leads to lowering of the degree of granule heterogeneity by their chemical and phase composition. The developed unit enhances the technological capabilities of the process of plasma-arc atomization of current-carrying wires, as a specialized control system was developed for this purpose, which includes the measuring, starting and control and signal equipment, in particular, use of a touch panel, programmable logic controller (PLC) and development of the re-

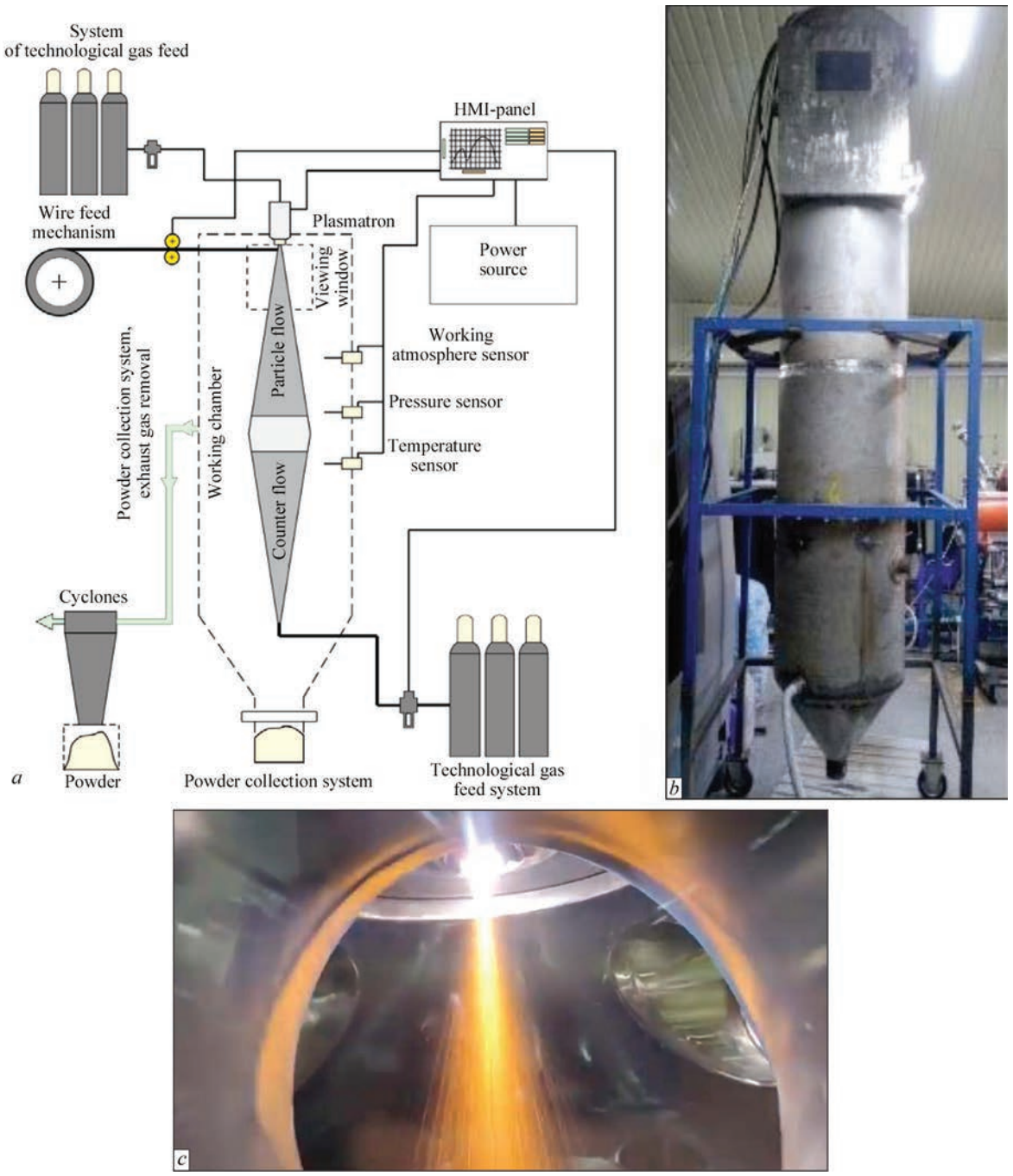

Figure 6. Scheme (*a*) and appearance (*b*) of experimental-production equipment and visualization (*c*) of the process of plasma-arc spheroidization of current-carrying materials with a chamber with protective atmosphere and counter gas flow

spective software. The unit software contains all the functions of control, adjustment, indication and emergency signaling of the unit operation modes. PLC has the function of an executive computing device, which on the basis of the data received from the monitoring system, performs correction of atomization process parameters and equipment operation algorithm, changing current, gas flow rates, wire feed rate, etc.

PWI developed an experimental-production unit for plasma-arc spheroidization of current-carrying materials (Figure 6), where a counter gas flow is used for control and monitoring of the speed and temperature characteristics of the granules. It allows greatly reducing the overall dimensions of the atomization chamber to 3 m chamber height, as the standard production chambers have not less than 10–15 m chamber height, and regulating the rate of particle cooling inside the chamber, in particular for formation of a fine-crystalline structure.

Numerical modeling means were used for calculation of the main structural parameters of this chamber, and for selection of optimal velocities of the counter gas flow. For this purpose, first modeling of the process of outflowing of argon plasma blown by an accompanying gas flow was performed in CFD software, by solving a system of MHD equations (5–12) and using a standard two-parametric *k–e* model of turbulence (13), and gas-dynamic and temperature characteristics of the plasma jet were defined (Figure 7):

1. Law of mass conservation:

$$\nabla \rho \upsilon. \tag{5}$$

2. Law of momentum conservation:

$$\rho\left(\vec{V}\cdot\nabla\vec{V}\right)=\vec{j}\cdot\vec{B}-\nabla p+\frac{2}{3}\mu\left(\nabla\vec{V}\right)+2\nabla\cdot\left(\mu\vec{S}\right). \tag{6}$$

3. Law of energy conservation:

$$\nabla\cdot\left(\rho\vec{V}h\right)=\nabla\cdot\left(\lambda\nabla T\right)+\vec{j}\cdot\vec{E}+\frac{5}{2}\frac{k_B}{e}\vec{j}\cdot\nabla T. \tag{7}$$

4. Maxwell equation:

$$\nabla\cdot\left(-\sigma\nabla\varnothing\right)=0, \tag{8}$$

$$\vec{E}=-\nabla\varnothing, \tag{9}$$

$$\nabla^2\vec{A}=-\mu_0\vec{j}, \tag{10}$$

$$\vec{B}=\nabla\cdot\vec{A}. \tag{11}$$

5. Ohm's law

$$\vec{j}=\sigma\cdot\vec{E}. \tag{12}$$

where ρ is the gas density, kg/m^3; $\vec{V}$ is the gas velocity, m/s; $\vec{j}\cdot\vec{B}$ is the Lorentz force due to electric current vector $\vec{j}$, A/m^2; and electromagnetic induction vector, $\vec{B}$, T; p is the pressure, Pa; μ is the dynamic viscosity of plasma, kg/m.s; $\vec{S}$ is the strain rate tensor; h is the enthalpy, J/kg; $\vec{E}$ is the electric field, V/m; k_B is the Boltzmann constant, J/K^{-1}; e is the elementary charge, C; σ is the electric conductivity of gas, W/m·K; Ø is the electrostatic potential, V; $\vec{A}$ is the vector potential of the electromagnetic field, T·m.

$$\mu_t=\rho C\frac{k^2}{\varepsilon}, \tag{13}$$

where k is the kinetic energy of turbulence, m^2/s^2; ε is the turbulent energy dissipation rate, m^2/s^3; ρ is the medium density, kg/m^3; C = 0.09; μ_t value has the dimension of kg/m·s.

At the next stage the Taylor Analogue Break-up (TAB) model of hydrodynamic break-up of the drops and the derived experimental data were used to model the process of dispersion of the melt forming during plasma-arc atomization at the edge of current-carrying 1.6 mm wire from AISI 316 steel (14–17). TAB model draws an analogy between the mass-spring-damper system and oscillations and deformation of the liquid drops leading to their refinement. In this analogy the surface tension force is represented by the restoring or stabiliz-

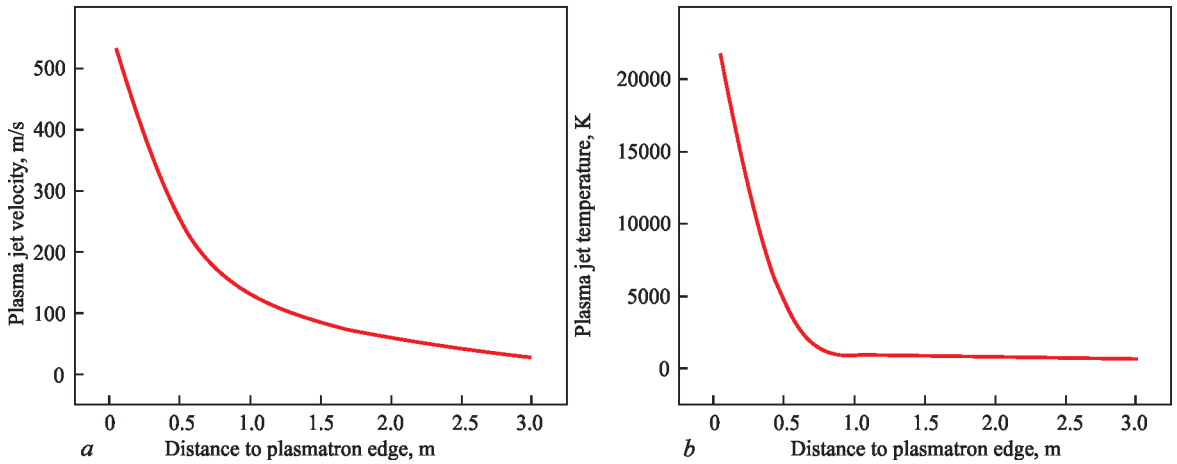

Figure 7. Gas-dynamic (*a*) and temperature characteristics (*b*) of argon plasma, blown by accompanying gas (P = 16 kW)

ing force of the spring, while the aerodynamic force of the gas is the source of external force, or the force, which destabilizes the mass, and the damping force is represented by the liquid viscosity characteristic:

$$m\ddot{x} = F - kx - d\dot{x}, \quad (14)$$

where m, F, k and d are the mass, force, spring constant and damping constant, respectively; x is the displacement of the drop equator from the equilibrium position in the form of a sphere to an oblate ellipsoid (Figure 8).

Using the Taylor's analogy coefficients, the physical dependencies of the coefficients in equation (14) have the following values:

$$\frac{F}{m} = C_f \frac{\rho_g u^2}{\rho_l r}, \quad (15)$$

$$\frac{k}{m} = C_k \frac{\sigma}{\rho_l r^3}, \quad (16)$$

$$\frac{d}{m} = C_d \frac{\mu_l}{\rho_l r^2}, \quad (17)$$

where ρ_l is the drop density, kg/m^3; ρ_g is the density of the continuous phase, kg/m^3; u is the relative speed of the drop, m/s; r is the initial drop radius, m; σ is the drop surface tension force, N/m; μ_l is the drop dynamic viscosity, kg/m·s. Values for dimensionless constants are as follows: $C_f = 0.33$; $C_d = 5$ and $C_k = 8$.

It was found that during atomization, particles the dimensions of which can be in the range of 20 to 500 μm, are formed. Investigations of these particles movement and their heat exchange with the atmosphere inside the atomization chamber (Figure 9) showed that at 3 m distance from the plasmatron edge their speed can be in the range of 8–30 m/s, depending on the calculated dimensions, and their temperature can be equal to 400–1200 K. This, in its turn, leads to particle deformation and formation of defective

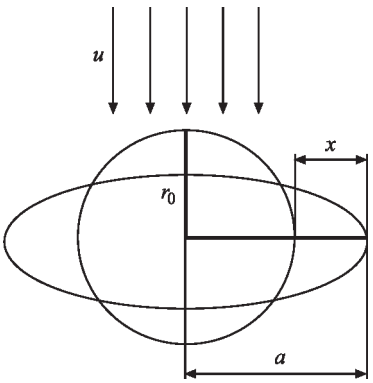

Figure 8. Drop deformation mechanism in keeping with TAB model

products at their collision with the walls of powder collector (at calculated chamber height, equal to 3 m).

It is shown that the counter gas flow allows performing processing in atomization chambers of not more than 3 m length, due to intensification of particle braking processes, and increasing the rate of heat exchange between the atmosphere and the particles (Figure 10).

Experimental studies of the sphericity coefficient of granules from AISI 316 stainless steel (Figure 11), produced at atomization in different atmospheres, showed that compared to atomization in air, use of chambers with a shielding argon atmosphere and counter gas flow allows increasing the sphericity coefficient of the granules from 0.73 to 0.85.

PWI is also performing studies of the processes of plasma-arc spheroidization of neutral (Figure 12, *a*) and current-carrying wires (Figure 12, *b*) and rods, using plasmatrons with a hollow copper anode, operating at reverse polarity.

It was found that the method of reverse polarity plasma-arc atomization (by the "wire–cathode" and neutral wire scheme) has a number of advantages among the currently available plasma spheroidization technologies, which are of wide practical interest, as:

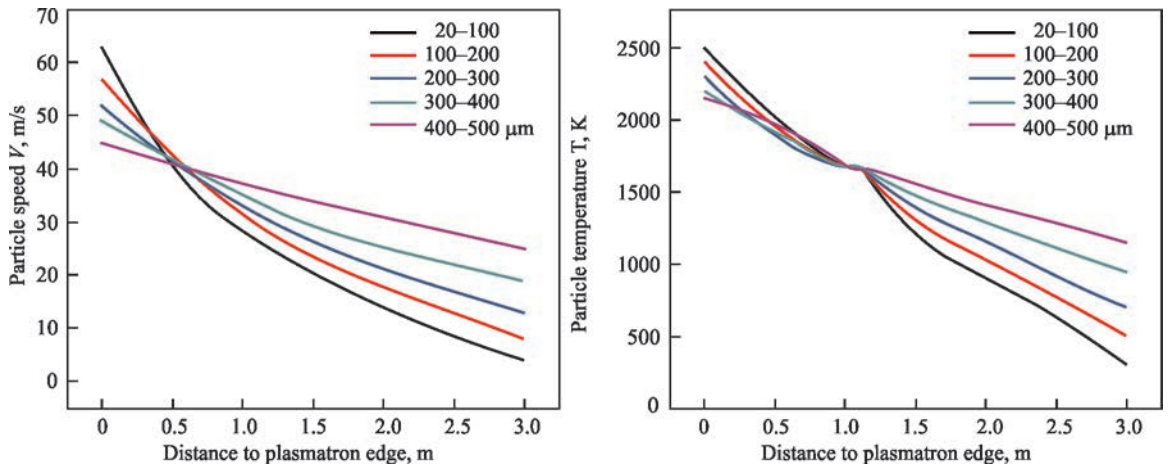

Figure 9. Dependence of the change in particle speed V (*a*) and temperature T (*b*) at a certain distance from plasmatron edge (without using counter gas flow)

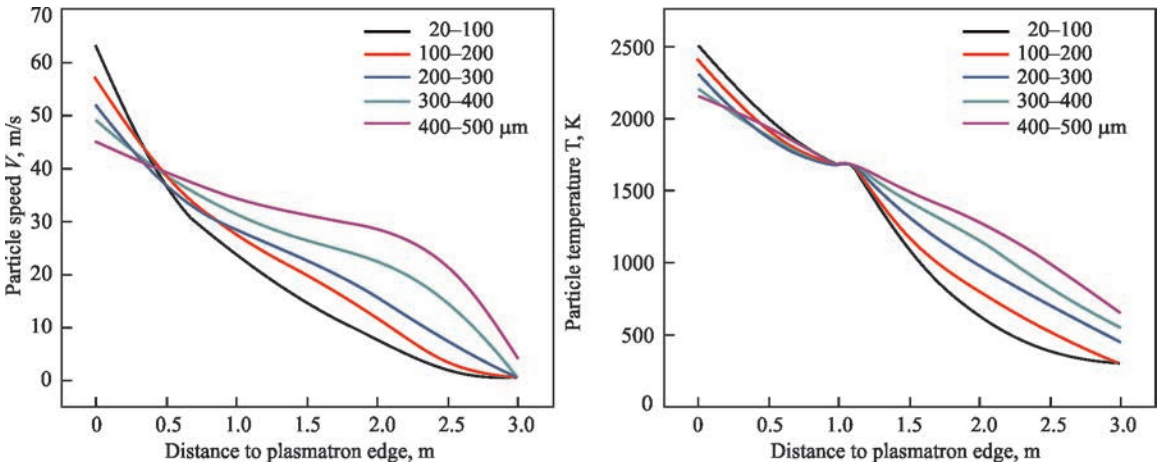

Figure 10. Dependence of the change in particle speed *V* (*a*) and temperature *T* (*b*) at a certain distance from plasmatron edge (using counter gas flow)

● they allow increasing electric power (up to 200 kW) due to "elongation" of the arc (from 150 to 550 V) in the copper electrode cavity owing to a change of the jet gas-dynamic characteristics, unlike plasmatrons operating at straight polarity, where increase of electric power is achieved by increasing the working current (from 400 to 1000 A), using high capacity power sources, which intensifies erosion of the nozzle and the electrode, or using plasmatrons of a more complex design (water-cooled IEI etc.)

● they enable dispersion of a wide range of sprayed materials (from large-diameter solid and flux-cored wires to rods of 50 mm and greater diameter, etc.);

● plasmatron design allows generation of a supersonic plasma jet with the velocity in the range of (1.5–4.0)·10^3 m/s, which greatly intensifies the processes of dispersion of the melt, forming at the spraying electrode edge, and increases the amount of the produced fine fraction (<80 μm) of the granules [26];

● a low rate of erosion (0.01 nanogram/C at 40 kW) of the electrode is achieved, which does not have any limitations as to the number of its operation starts, which also greatly prolongs the plasma equipment service life;

● thermal efficiency of plasmatrons with a hollow copper cathode is on the level of 0.80–0.85, here the power transferred to the product by the plasma flow, P_{pl} at the same operation modes is 1.2 to 1.5 times greater, than at straight polarity. It results in improvements of the process efficiency, allowing a significant reduction of the amount of energy consumed in melting one unit of the wire volume [27].

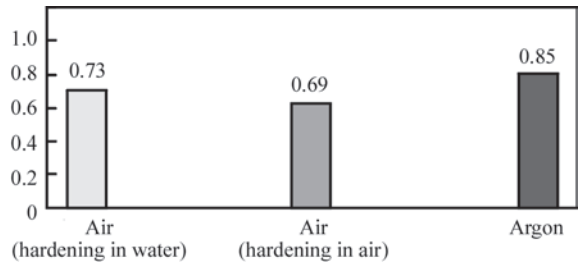

Figure 11. Dependence of sphericity parameters of sprayed particles from AISI 316 stainless steel of 20–100 μm fraction on ambient atmosphere type (*P* = 16 kW): *1* — air (hardening in water); *2* — air (hardening in air); *3* — argon

The data obtained at numerical modeling of the abovementioned process (Figure 13) confirmed that at plasmatron operation at reverse polarity current, arc voltage *U* is much higher than when working at straight polarity, $U_{RP} \approx (1.1–1.5)U_{SP}$ (U_{RP} is the constricted arc voltage at plasmatron operation at reverse polarity, U_{SP} is the constricted arc voltage during plasmatron operation at straight polarity), resulting in higher productivity of the plasmatron [28].

In accordance with that a line of plasmatrons were developed for atomization of neutral and current-car-

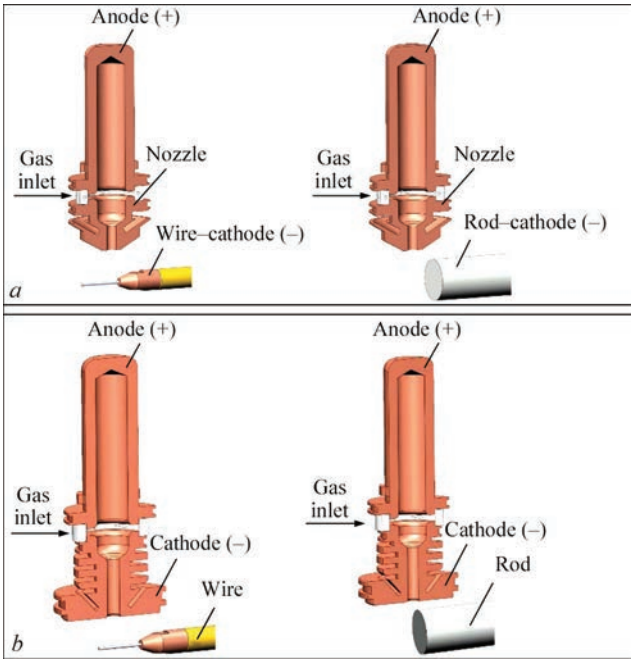

Figure 12. Scheme of plasma-arc atomization process at reverse polarity using plasmatrons with a copper hollow anode: current-carrying (*a*) and neutral (*b*)

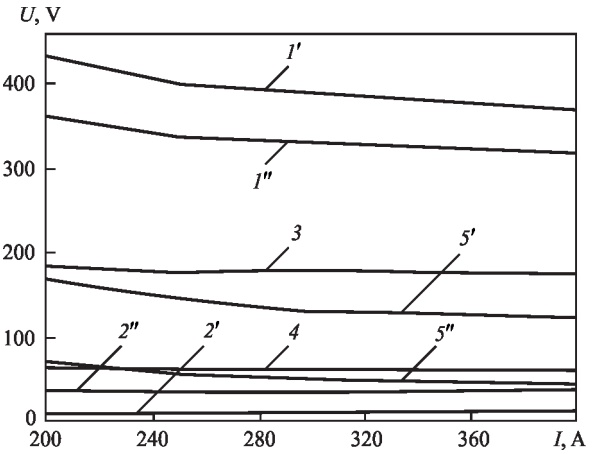

Figure 13. Dependence of constricted arc voltage on current: *1* — total arc voltage; *2* — voltage inside hollow electrode; *3* — voltage in the nozzle plasma-forming channel; *4* — voltage in open section of the arc; *5* — voltage in the cut cavity at plasmatron operation at reverse (*1′*, *5′*) and straight polarities (*1″*, *5″*)

rying materials, using approaches established when designing and manufacturing the plasmatrons for reverse polarity cutting.

PRODUCING SPHERICAL GRANULES BY PLASMA-ARC ATOMIZATION OF WIRE MATERIALS

Experiments on atomization of various types and grades of current-carrying compact (Figure 14, *a*) and flux-cored wires (Figure 14, *b*) were performed in PLAZER-50-PL-W unit with further analysis of the technological and structural features of the produced granules.

So, investigation of particle size distribution of granules (Figure 15) produced at atomization of current-carrying compact wire from AISI 316 stainless steel, showed that owing to a large number of regulated parameters the above equipment allows producing spherical granules in the size range of 15–315 μm. Here, in certain atomization modes it is possible to obtain a large amount of fine fraction. The main fraction is 15–100 μm, which makes up to 90 wt.%,

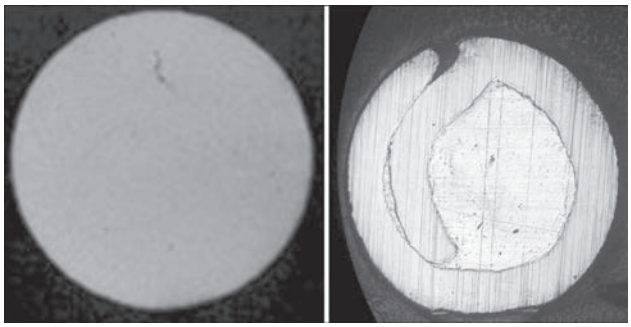

Figure 14. SEM images of the cross-section of compact wire from AISI 316 stainless steel (*a*) and flux-cored wire of Fe–Al(86Fe + 14Al wt.%) alloying system (*b*)

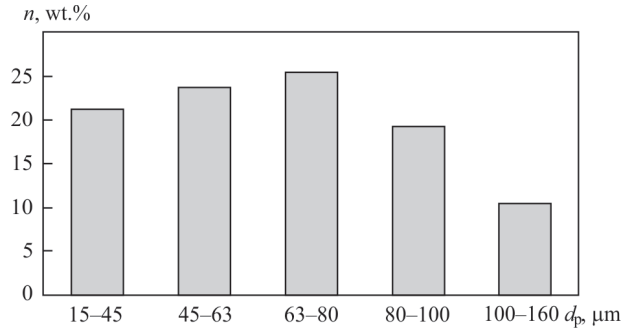

Figure 15. Particle size distribution of granules produced at atomization of compact wire from AISI 316 stainless steel

where the proportion of 15–45 μm fraction is equal to 21.2 wt.%, that of 45–63 μm fraction — 23.7 wt.%, that of 63–80 μm fraction — 25.4 wt.%, that of 80–100 μm fraction — 19.2 wt.%, that of 100–160 μm fraction — 10.5 wt.%, and the average diameter d_{50} = 63 μm.

Investigations of the shape of these granules showed that on the whole they are of a regular spherical shape (Figure 16, *a*) with sphericity coefficient S = 0.83 and higher, while the proportion of irregularly-shaped particles is not more than 1 wt.%.

Results of investigations of the technological properties of the abovementioned granules showed that their fluidity (in the case of –45; +15 μm frac-

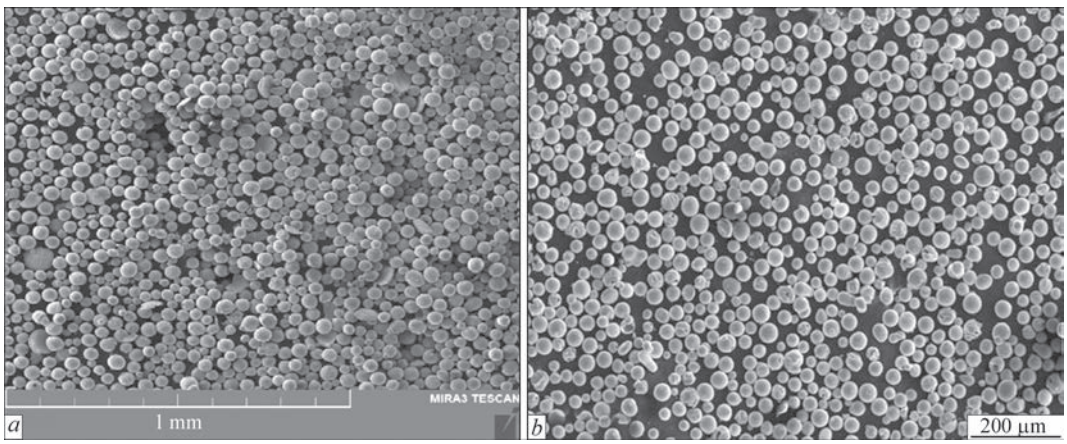

Figure 16. SEM image of granules produced at atomization of compact wire from AISI 316 stainless steel (*a*) and Ti Grade2 titanium (*2*) [31]

Table 2. Particle size distribution and fluidity of granules of different grades from 316 L stainless steel

Powder brand and production method	Fraction size, μm	d_{90}, μm	d_{50}, μm	d_{10}, μm	Fluidity, s/50 g
MetcoAdd 316-A, GA	–45; +15	46	30	19	<20
PLAZER-30, PA	–45; +15	43	28	17	18
GA [29]	–45;+15	45	22	8	29

Table 3. Particle size distribution of granules, produced at atomization of current-carrying compact wires of different chemical composition

Number	Material	Wire diameter, mm	Power, kW	Average granule diameter d_{50}, μm
1	Cu–ETP copper	1.2	21	52
2	AISI 316 stainless steel	1.0	18	63
3	NiCr-3 nickel alloy	2.0	21	184
4	Inconel 625 nickel alloy	1.2	22	87
5	Ti Grade 2 titanium	1.6	14	152

tion) is at the same level as that of another commercial powder of MetcoAdd 316-A grade (Oerlicon AM Co., Ltd, Germany), widely used by SLM and DMLS methods and it is equal to 18 s/50 g.

It should be also noted that the productivity of the abovementioned process for this mode of atomization of current-carrying wire from AISI 316 stainless steel (plasma arc power P = 18 kW and total argon flow rate Q = 25 m^3/h) is equal to 10.5 kg/h with further possibility of its increase. Table 3 gives the results of analysis of particle size distribution of granules produced at atomization of current-carrying compact wires of different chemical composition.

Investigations of the process of plasma-arc atomization of current-carrying flux-cored wire of Fe-Al alloying system, showed that the above process al-

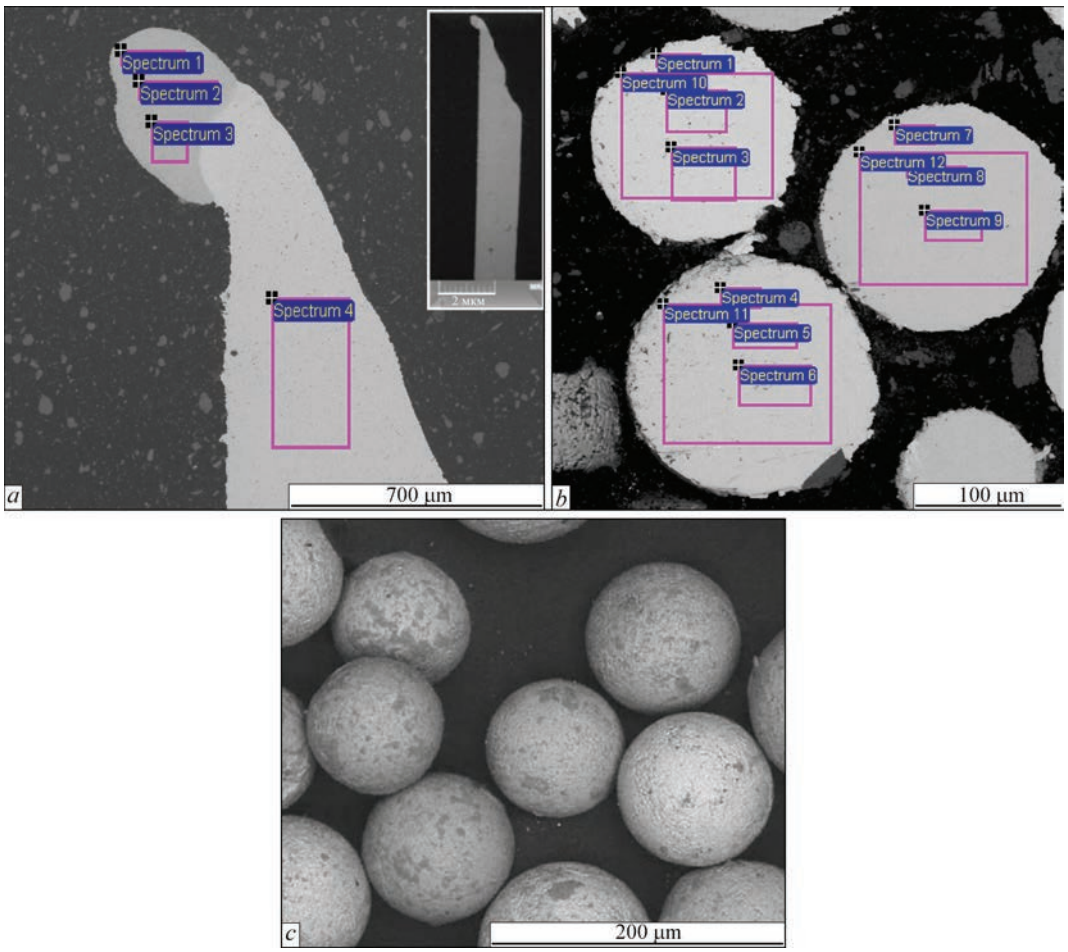

Figure 17. SEM image of Fe–Al wire edge after an abrupt extinguishing of the arc during plasma-arc atomization (*a*), granule microstructure (*b*) and appearance of particles (*c*): spectra 1–3 — zone of metallurgical interaction of the wire material at its melting and atomization; spectrum 4 — wire zone not subjected to thermal impact; spectra 1–12 — zone with granule cross-section

Table 4. Chemical composition of local zones at the edge of flux-cored wire–anode Fe–Al after an abrupt extinguishing of the arc during plasma-arc atomization and granule microstructure

Local zone number (spectrum)	Image	Chemical composition of local zones, at.%			
		Fe	Al	Si	O
1	Figure 17, *a*	76.49	23.51	–	–
2		75.49	24.51	–	–
3		74.15	25.85	–	–
4		99.64	–	0.36	–
1	Figure 17, *b*	82.92	16.04	0.55	0.49
2		82.67	16.31	0.70	0.32
3		83.01	16.44	0.21	0.34
4		74.07	25.09	0.63	0.21
5		74.78	24.62	0.46	0.14
6		74.44	24.94	0.43	0.19
7		71.67	27.71	0.20	0.42
8		72.52	27.52	0.00	0.23
9		71.59	28.01	0.13	0.27
10		83.17	16.22	0.24	0.37
11		74.10	25.03	0.71	0.16
12		71.75	27.85	0.12	0.28

lows producing spherical granules from high alloys (Figure 17, *c*), which are difficult or impossible to produce by the traditional methods (nickel, titanium, iron intermetallics and other alloys). Such granules further on can be used to manufacture products of a complex geometry, for instance by the technology of cold gas-dynamic spraying and further HT or TMT. The paper presents the results of experimental investigations of the processes of heating, melting and interaction of 86Fe + 14Al wt.% flux-cored wire, consisting of a steel sheath from St-08rim low-carbon steel and powder filler (aluminium of PA-4 grade) at optimal parameters of the atomization mode (18 kW power) in PLAZER-50-PL-W equipment. These studies showed that the above process allows producing spherical granules of a chemical composition, which practically does not differ from the composition of the initial material (flux-cored wire), while the proportion of granules with external and internal defects is not higher than 1.0–1.5 wt.% (Table 4) at average diameter d_{50} = 115 μm and up to 45 wt.% proportion of fine fraction of <100 μm.

Studies of melted-off edge of the flux-cored wire after an abrupt extinguishing of the arc, using X-Ray microspectral analysis (Tescan MIRA 3 LMU) showed that at the wire edge metallurgical interaction of the molten metal sheath and the aluminium filler takes place, leading to formation of a melt, the integral chemical composition of which corresponds to intermetallic of Fe_3Al type (Figure 7, *a*, Table 4). Investigation of the heterogeneity of intermetallic granules of different fractions (Table 4) showed a small inhomogeneity of chemical composition of the produced granules. So, Al proportion can vary from 16 to 28 at.%. At the same time, however, investigation of the granule phase composition by the method of X-Ray diffraction phase analysis (DRON-3M, CuK_α-radiation) showed that the proportion of Fe_3Al intermetallic phase can be up to 85 wt.%.

PRODUCING SPHERICAL GRANULES BY PLASMA-ARC ATOMIZATION OF RODS AND INGOTS

Experiments on atomization of current-carrying compact wire of 1.6 mm diameter from low-carbon steel of ER70S-6 grade and stationary rod of 50 mm diameter from low-carbon Q235 steel at 120 kW power of the plasma arc were performed in PLAZER-50-PL-W unit, upgraded for plasma atomization at reverse polarity.

Analysis of particle size distribution of granules (Figure 18) produced at atomization of current-carrying wire showed that during atomization spherical granules in the size range of 15–630 μm are

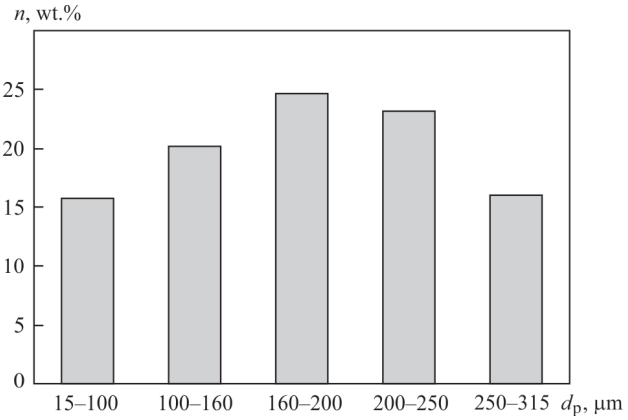

Figure 18. Particle size distribution of granules produced at atomization of current-carrying compact ER70S-6 wire of 1.6 mm diameter by plasmatron at reverse polarity and 120 kW power

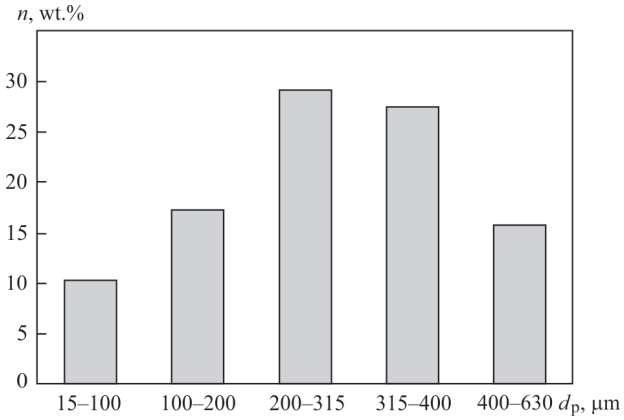

Figure 19. Particle size distribution of granules produced at atomization of a current-carrying stationary rod from low-carbon Q235 steel rod of 50 mm diameter by a plasmatron at reverse polarity and 120 kW power

formed, with the following percentage of fractions: 15–100 μm — 15.8 wt.%, 100–160 μm — 20.2 wt.%, 160–200 μm — 24.7wt.%, 200–250 μm — 23.2 wt.%, 250–315 μm — 16.1 wt.%, and the average diameter is d_{50} = 183 μm.

Analysis of particle size distribution of the granules (Figure 19), produced at atomization of current-carrying wire, showed that during atomization spherical granules in the size range of 15–630 μm are formed, with the following percentage of fractions: 15–100 μm — 10.3 wt.%; 100–200 μm — 17.2 at.%; 200–315 μm — 29.2 wt.%, 315–400 μm — 27.5 wt.%, 400–630 — 15.8 wt.%, average diameter being equal to d_{50} = 282 μm.

Study of the produced granules shape (Figure 20) showed that on the whole they have a regular spherical shape (Figure 20, *a*) with sphericity coefficient S = 0.75 and more, and the proportion of irregularly-shaped particles is not more than 5 wt.%. The productivity of atomization process at 120 kW power can be up to 16 kg/h for current-carrying compact wire from low-carbon ER70S-6 steel of 1.6 mm diameter, and in the case of atomization of a stationary rod from low-carbon Q235 steel of 50 mm diameter it is 20 kg/h. Here, a tendency is also observed to further improvement of productivity at increase of plasma arc power to 200 kW.

Thus, despite a high productivity the above process requires further investigations and development of additional technological measures, which will allow a significant increase of the amount of the fraction, suitable for application in AM and granule metallurgy technologies.

CONCLUSIONS

1. Critical analysis of modern technologies for producing spherical granules showed that in the general case the technologies of gas atomization are characterized by the presence of a large number of satellites and irregularly-shaped particles, lower coefficient of sphericity and intragranular argon-induced porosity, leading to formation of defects in the deposited layers and causing a significant lowering of the values of ultimate strength, impact toughness and other mechanical characteristics of finished products. The Plasma Rotating Electrode Process allows avoiding the majority of these disadvantages. Equipment operation, however, involves considerable difficulties for producing a fine fraction of <100 μm. To achieve more than 50 wt.% yield of the mentioned fraction, there is the need for an essential increase of the billet rotation speed (more than 30000 rpm), which greatly complicates the already not at all simple kinematic diagram of the unit (lowering of the level of vibrations, designing complex bearing systems, etc.). There are also difficulties associated with producing the cylindrical billet of precise dimensions, which has to be polished with a high accuracy, etc.

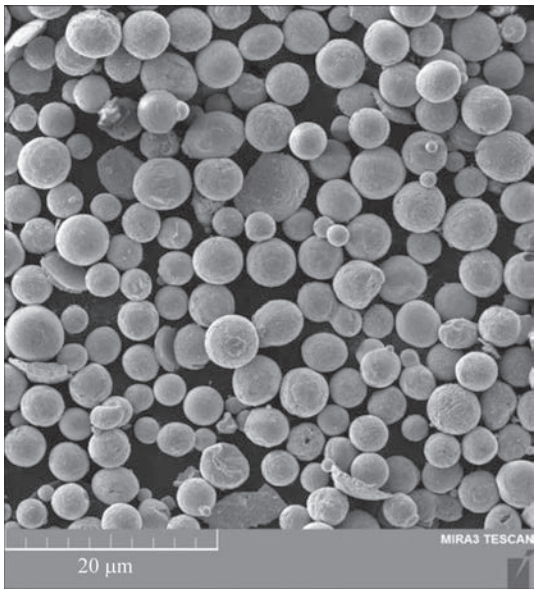

Figure 20. SEM images of granules produced at atomization in air of a current-carrying stationary rod from low-carbon Q235 steel of 50 mm diameter

2. It was found that the technology of plasma-arc atomization has considerable potential for further development and practical application in spherical granule manufacturing. One of its variants is the process of plasma-arc atomization of current-carrying and neutral wires, rods and large-sized ingots of up to 50 mm and greater diameter. The abovementioned process is characterized by higher values of energy efficiency and productivity, which can reach up to 20 kg/h, and relative simplicity of the equipment, and it allows producing spherical granules in a broad range of dimensions of 15–315 μm. Here, the amount of <100 μm fraction may reach 90 wt.%. A new generation PLAZER-50-PL-W unit was developed for

plasma-arc spheroidization of neutral and current-carrying wires and rods. Its feature is application of a plasmatron with higher current load and intelligent system of automatic real-time control and monitoring of a greater number of technological parameters. The designed atomization chamber with shielding atmosphere with gas counter flow allows a significant reduction of overall dimensions of the equipment, namely chamber height from 10–15 to 3 m, enables controlling particle cooling processes to form a finely-dispersed structure, and promotes producing spherical granules in the size range of 20–315 μm with the sphericity coefficient of 0.75–0.85.

3. Plasma-arc technologies developed at PWI allow producing spherical granules from the entire range of materials, widely used in the area of 3D printing of high-quality products by the methods of selective and direct laser melting and sintering, electron beam melting, cold gas-dynamic spraying and granule metallurgy technologies for producing high-quality structural metallic materials by compacting particles (granules) of a microcrystalline structure, which crystallized from the melt at a high rate.

REFERENCES

1. Iliyushchenko, A.F., Savich, V.V. (2017) History and state-of-the-art of additive technologies in Belarus, powders of metals and alloys for them. *Kosmichna Nauka i Tekhnologiya*, 23(**4**), 33–45 [in Russian]. DOI: https://doi.org/10.15407/knit2017.04. 033
2. Singh, D.D., Mahender, T., Reddy, A.R. (2021) Powder bed fusion process: A brief review. *Materials Today: Proceedings*, 46(**1**), 350–355. DOI: https://doi.org/10.1016/j.matpr.2020.08.415
3. Ahn, D.G. (2021) Directed energy deposition (DED) process: State of the art. *Int. J. of Precis. Eng. and Manuf. — Green Tech.*, **8**, 703–742. DOI: https://doi.org/10.1007/s40684-020-00302-7
4. Anderson, I.E. et al. (2018) Feedstock powder processing research needs for additive manufacturing development. *Curr. Opin. Solid State Mater. Sci*., 22(**1**), 8–15. DOI: https://doi.org/10.1016/j.cossms.2018.01.002
5. Chen, G., Zhao, S.Y., Tan, P. et al. (2018) A comparative study of Ti–6Al–4V powders for additive manufacturing by gas atomization, plasma rotating electrode process and plasma atomization. *Powder Technology*, **333**, 38–46. DOI: https://doi.org/10.1016/j.powtec.2018.04.013
6. Sun, P., Fang, Z., Zhang, Y. et al. (2017) Review of the methods for the production of spherical Ti and Ti alloy powder. *JOM*, **69**, 1853–1860. DOI: https://doi.org/10.1007/s11837017-2513-5
7. Heidloff, A.J., Rieken, J.R., Anderson, I.E. et al. (2010) Advanced gas atomization processing for Ti and Ti alloy powder manufacturing. *JOM*, **62**, 35–41. DOI: https://doi.org/10.1007/s11837-010-0075-x
8. Guo, K., Liu, C., Chen, S. et al. (2020) High pressure EIGA preparation and 3D printing capability of Ti–6Al–4V powder. *Transact. of Nonferrous Metals Society of China*, 30(**1**), 147–159. DOI: https://doi.org/10.1016/S1003-6326(19)65187-3
9. Martín, A., Cepeda-Jiménez, C.M., Pérez-Prado, M.T. (2020) Gas atomization of γ-TiAl alloy powder for additive manufacturing. *Adv. Eng. Mater.*, **22**, 1900594. DOI: https://doi.org/10.1002/adem.201900594
10. Drawin, S., Deborde, A., Thomas, M. et al. (2020) Atomization of Ti-64 alloy using the EIGA process: comparison of the characteristics of powders produced in labscale and industrial-scale facilities. *MATEC Web Conf.*, **321**, 07013. DOI: https://doi.org/10.1051/matecconf/202032107013
11. Zhong, C., Chen, J., Linnenbrink, S. et al. (2016) A comparative study of Inconel 718 formed by high deposition rate laser metal deposition with GA powder and PREP powder. *Materials & Design*, **107**, 386–392. DOI: https://doi.org/10.1016/j.matdes.2016.06.037
12. Zhao, Y., Cui, Y., Numata, H. et al. (2020) Centrifugal granulation behavior in metallic powder fabrication by plasma rotating electrode process. *Sci. Rep.*, 10, 18446. DOI: https://doi.org/10.1038/s41598-020-75503-w
13. *Yang* Liu, Xiao-hao Zhao, Yun-jin Lai et al. (2020) A brief introduction to the selective laser melting of Ti6Al4V powders by supreme-speed plasma rotating electrode process. Progress in Natural Science. *Materials Inter.*, 30(**1**), 94–99. DOI: https://doi.org/10.1016/j.pnsc.2019.12.004
14. Strogonov, D.V., Korzhyk,V.M., Jianglong Ti, et al. (2022) Influence of the parameters of the process of plasma-arc spheroidization of current-conducting wire from low-carbon steel on the granulometric composition of the produced powders. *Suchasna Elektrometal.*, **3**, 29–38 [in Ukrainian]. DOI: https://doi.org/10.1037434/sem2022.03.05
15. Yurtkuran, E., Ünal, R. (2022) Theoretical and experimental investigation of Ti alloy powder production using low-power plasma torches. *Transact. of Nonferrous Metals Society of China*, 32(**1**), 175–191. DOI: https://doi.org/10.1016/S1003-6326(21)65786-2
16. Tsantrizos, P.G, Allaire, F., Entezarian, M. (1998) *Method of production of metal and ceramic powders by plasma atomization*. US patent, 5707419 [P], 1998−01−13.
17. Cacace, S., Boccadoro, M., Semeraro, Q. (2023) *Investigation on the effect of the gas-to-metal ratio on powder properties and PBF-LB/M processability*. Prog. Addit. Manuf. DOI: https://doi.org/10.1007/s40964-023-00490-z
18. Korzhyk, V.M., Strogonov, D.V., Burlachenko, O.M. et al. (2023) New generation unit for plasma-arc deposition of coatings and spraying of current-conducting wire materials. *Suchasna Elektrometal.*, **3**, 19–27 [in Ukrainian]. DOI: https://doi.org/10.37434/sem2020.03
19. Korzhyk, V.M., Strogonov, D.V., Burlachenko, O.M. et al. (2023) Effectiveness of the process of plasma-arc spheroidization of current-conducting titanium wire. *Suchasna Elektrometal.*, **1**, 1–9 [in Ukrainian]. DOI: https://doi.org/10.37434/sem2023.01.05
20. Capus, J. (2017) AP&C: moving fast with the rise of AM. *Metal Powder Report*, 72(**1**), 22–24. DOI: https://doi.org/10.1016/j.mprp.2016.12.001
21. Petrunichev, V.A., Kudinov, V.V., Kulagin, I.D. (1965) Production of spheroidized metal powder by wire spraying. *Metally*, **2**, 68–94 [in Russian].
22. Zelenin, V.I., Kavunenko, P.M., Tisenkov, V.V. et al. (2009) Application of plasma-arc metallization for restoration of wheel pairs. *The Paton Welding J.*, **12**, 28–31.
23. Korzhik, V.N., Korob,M.F. (2012) Mechanized line PLAZER 30PL-W for plasma-arc wire spraying of coatings on large-sized parts of "shaft" type. *Svarshchik*, **4**, 13–15 [in Russian].
24. Kharlamov, M.Yu., Krivtsun, I.V., Korzhik, V.N. et al. (2008) Effect of the type of concurrent gas flow on characteristics of the arc plasma generated by plasmatron with anode wire. *The Paton Welding J.*, **6**, 14–18.
25. Kharlamov, M., Krivtsun, I., Korzhyk, V., Demyanov, O. (2015) Simulation of motion, heating and breakup of molten metal droplets in the plasma jet at plasma-arc spraying. *J. of Thermal Spray Technology*, **24**, 659–670. DOI: https://doi.org/10.1007/s11666-015-0216-4

26. Liu, F., Yu, D., Zhang, Q. et al. (2023) Experimental and numerical analysis of a novel reverse-polarity plasma torch with transferred arc hot-wall nozzle for atmospheric plasma spraying of YSZ coatings. *Surface and Coatings Technology*, **459**, 129413. DOI: https://doi.org/10.1016/j.surfcoat.2023.129413
27. Shchitsyn, V.Yu., Yazovskikh, V.M. (2009) Effect of polarity on the heat input into the nozzle of a plasma torch, *Welding International*, 16(**6**), 485–487. DOI: https://doi.org/10.1080/09507110209549563
28. Kharlamov, M.Yu., Krivtsun, I.V., Korzhik, V.N. et al. (2015) Modelling the characteristics of constricted-arc plasma in straight and reverse polarity air-plasma cutting. *The Paton Welding J.*, **10**, 10–18.
29. Bouabbou, A., Vaudreuil, S. (2023) Numerical modelling of SS316L powder flowability for laser powderbed fusion. *Archives of Materials Sci. and Engineering*, 120(**1**), 22–29. DOI: https://doi.org/10.5604/01.3001.0053.6014

ORCID
V.M. Korzhyk: 0000-0001-9106-8593,
D.V. Strohonov: 0000-0003-4194-764X,
O.M. Burlachenko: 0000-0003-2277-4202,
O.M. Voitenko: 0000-0003-4946-6517

CONFLICT OF INTEREST
The Authors declare no conflict of interest

CORRESPONDING AUTHOR
V.M. Korzhyk
E.O. Paton Electric Welding Institute of the NASU
11 Kazymyr Malevych Str., 03150, Kyiv, Ukraine
E-mail: vnkorzhyk@gmail.com

SUGGESTED CITATION
V.M. Korzhyk, D.V. Strohonov, O.M. Burlachenko, O.M. Voitenko, D.V. Kunitskyi (2023) Development of plasma-arc technologies of spherical granule production for additive manufacturing and granule metallurgy. *The Paton Welding J.*, **12**, 3–18.

JOURNAL HOME PAGE
https://patonpublishinghouse.com/eng/journals/tpwj

Received: 19.10.2023
Accepted: 26.12.2023

SUBSCRIPTION–2024

«The Paton Welding Journal» is Published Monthly Since 2000 in English, ISSN 0957-798X, doi.org/10.37434/tpwj.

«The Paton Welding Journal» can be also subscribed worldwide from catalogues subscription agency EBSCO.

If You are interested in making subscription directly via Editorial Board, fill, please, the coupon and send application by Fax or E-mail.

12 issues per year, back issues available.

$384, subscriptions for the printed (hard copy) version, air postage and packaging included.

$312, subscriptions for the electronic version (sending issues of Journal in pdf format or providing access to IP addresses).

Institutions with current subscriptions on printed version can purchase online access to the electronic versions of any back issues that they have not subscribed to. Issues of the Journal (more than two years old) are available at a substantially reduced price.

The archives for 2009–2021 are free of charge on
www://patonpublishinghouse.com/eng/journals/tpwj

ADVERTISING
in «The Paton Welding Journal»

External cover, fully-colored:
First page of cover
(200×200 mm) — $700
Second page of cover
(200×290 mm) — $550
Third page of cover
(200×290 mm) — $500
Fourth page of cover
(200×290 mm) — $600

Internal cover, fully-colored:
First/second/third/fourth page
(200×290 mm) — $400

Internal insert:
(200×290 mm) — $340
(400×290 mm) — $500

- Article in the form of advertising is 50 % of the cost of advertising area
- When the sum of advertising contracts exceeds $1001, a flexible system of discounts is envisaged
- Size of Journal after cutting is 200×290 mm

Address
11 Kazymyr Malevych Str., 03150, Kyiv, Ukraine
Tel./Fax: (38044) 205 23 90
E-mail: journal@paton.kiev.ua
www://patonpublishinghouse.com/eng/journals/tpwj

DOI: https://doi.org/10.37434/tpwj2023.12.02

INFLUENCE OF BLOWING AND LOADING OF WORKING SPACE ON MECHANICAL PROPERTIES OF SAMPLES MANUFACTURED USING SLM TECHNOLOGY

S.V. Adzhamskyi[1,2], **G.A. Kononenko**[1,3], **R.V. Podolskyi**[1,3], **S.I. Badyuk**[1]

[1]LLC "Additive Laser Technology of Ukraine"
31v Str. Serhiy Podolynskyi, 49000, Dnipro, Ukraine
[2]Institute of Transport Systems and Technologies of the NASU
5 Str. Pysarzhevsky, 49000, Dnipro, Ukraine
[3]Z.I. Nekrasov Iron and Steel Institute of the NASU
1 Academician Starodubov Sq., 49000, Dnipro, Ukraine

ABSTRACT

At present, for selective laser melting (SLM, Selective Laser Melting), studying the influence of characteristics of blowing and a loading of the working space on mechanical properties of titanium Ti6Al4V alloy is an urgent task. In the work, tensile samples were studied, for which as a result of a different loading of the building space, there was a pause of different duration between the deposition of powder and return of the laser beam. Based on the analysis of the values of mechanical properties, it was found that characteristics of strength of test samples in the area of the inlet nozzle of inert gas blowing have a value by 3–5 % lower compared to the central area of the platform with a range of values of ± 2 %, in the area of the outlet nozzle, the value is lower by 3–5 % compared to the central area, a range of values is ± 10 %. It was found that an increase in the pause from 50 to 65 s leads to a decrease in strength and ductility characteristics by 23 and 10 %, up to 80 s by 33 and 0.7 %, respectively.

KEYWORDS: selective laser melting, blowing, loading of the working space, Ti6Al4V alloy, mechanical properties

INTRODUCTION

Selective laser melting (SLM) technology consists in building a solid object by multicycle surfacing of thin layers of material on previously produced layers. In such processes, the material is subjected to complete melting to provide its joining with the previous layer and the subsequent reusable heating to high temperatures [1, 2]. SLM technology is a relatively new type of metal treatment that allows implementing an accurate fabrication of complex-shape structures [3, 4].

It should be noted that a large number of research is devoted to the issues of selective laser melting and electron beam fusion of powder layer [5–7]. It should be also taken into account, that each piece of equipment has its own technological aspects, one of which is the environment and the processes occurring during printing. For example, the process of fusion by electron beam gun irradiation is carried out in a vacuum environment, and in selective laser melting, in most cases argon (Ar) or nitrogen (N_2), in other — helium (He) is used [8]. If we consider this issue in more detail, it can be said that in the process of fusion as a result of electron beam gun irradiation, in a vacuum environment, the intensity of cooling the melt pool is lower due to the fact that it is affected only by the temperature gradient and crystallization rate [9]. When using an inert medium, to shield the powder layer with laminar gas flows, in the process of selective laser melting, the rate of cooling the melt pool and adjacent layers is additionally affected by gas due to its corresponding physical properties, velocity and flow direction [10]. Thus, the use of rational parameters of velocity control and distribution of gas flow is an additional method of influencing the mechanical properties of a product.

At present, the issues of velocity and flow direction on mechanical properties and density are paid great attention [11–13]. The interest to this issue is caused by such a common phenomenon in the field of printing as the powder ejection into the area of the outlet [14, 15] due to evaporation, picking up and transferring of particles (Figure 1), which as a result can get into the zone of laser beam effect, melt into and affect the density of a finished product. Changes in the inlet flow (nozzle design) lead to changes in the flow in the printing area and in the cooling rate of the melt pool, which also play a role in influencing the quality of a finished product (Figure 2). It should be noted that fabricating parts by this method is in most cases a single or small batch production, which can also have a significant impact on the repeatability of the results. This is associated with the constant change in the cross-section of parts, their quantity and laser beam intensity.

Copyright © The Author(s)

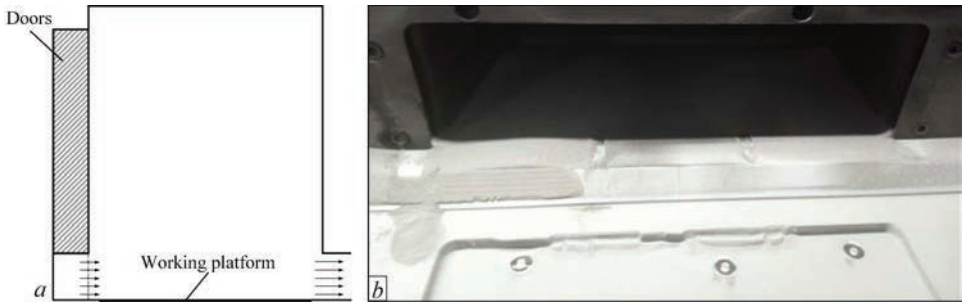

Figure 1. Scheme of outlet and inlet hole location (*a*), ejection of powder particles of Ti6Al4V alloy near the area of inlet hole (*b*)

As a result of the research carried out by the authors of [11], the effect of the inert gas flow on powder particles ejected and returned to the surface of the powder layer during the printing process, which is a general phenomenon in SLM technology, was analyzed. As a result of the study, it was established that the density of parts manufactured by SLM technology was influenced by the morphology of transferred particles. The more important fact is that samples printed by SLM process are not uniform in density due to the effect of gas flow.

In [12] it was established that the uniformity of the gas flow in the SLM process has a significant effect on the density and tensile strength of printed parts. The authors established a rational argon flow velocity in the range of 1.3–2.0 m/s for printing.

Since the authors of [13] did not consider the issue of density and mechanical properties of test samples in real printing conditions (with printing of parts of different cross-section and quantity), the study of witness-samples manufactured in the same printing process together with products is definitely relevant.

It follows from the abovementioned, that the issue of the influence of cooling rate, gas flow circulation and loading of the working space on the density of test samples and mechanical properties is insufficiently studied and is of fundamental and practical importance.

The aim of the work is to study the influence of the working space loading (pause duration between layers formation), velocity and features of the flow circulation on mechanical properties under the conditions of operation of Alfa-150D machine.

MATERIAL AND RESEARCH PROCEDURE

The work examined tensile test samples fabricated in a 3D printing machine Alfa-150D produced by ALT Ukraina LLC [5] from metal powder of titanium Ti–6Al–4V alloy with the following chemical composition, wt.%: A1 – 6.21; V – 4.03; Fe – 0.04; C – 0.1; O – 0.7; N – 0.02; Ti is the base [16], the granulometric analysis is presented in Figure 3.

Alfa-150D 3D printing machine produced by ALT Ukraina LLC with a printing area of 150×150 mm is equipped with an inlet and outlet nozzle for maximum collection of inert gas entering through the inlet nozzle without dispersing it throughout the working chamber. In order to provide inert gas collection and at the same time not to blow powder, the velocity of the flow over the working platform in the printing area was taken to be 1.5 m/s. The working gas is argon with a constant density and temperature. Between the main and auxiliary inlet nozzles, the flow is distributed in such a way that 70 % of the total argon flow rate is on the main nozzle, and 30 % on the auxiliary one. The introduction of the auxiliary inlet nozzle in the upper part of the working chamber led to the fact that dispersion of the flow during its movement from the main inlet nozzle to the outlet is reduced. In this case, the flow has a laminar flowing mode.

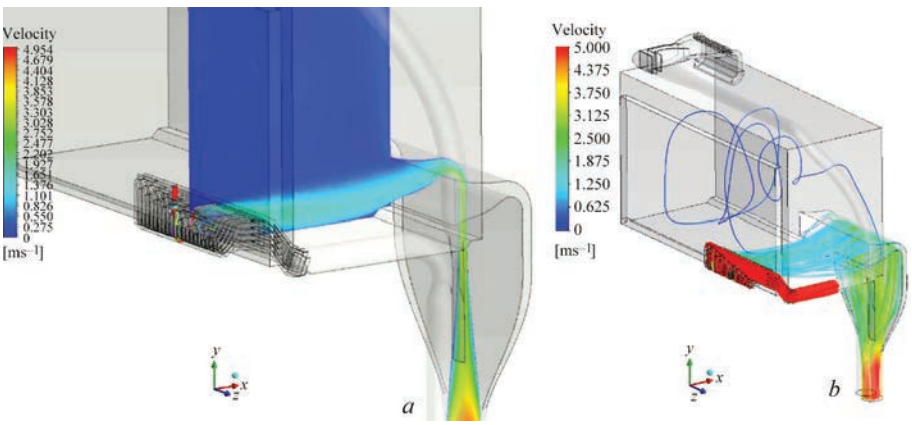

Figure 2. Display of gas movement in the working chamber of Alfa-150D machine: *a* — velocity diagram; *b* — flow lines

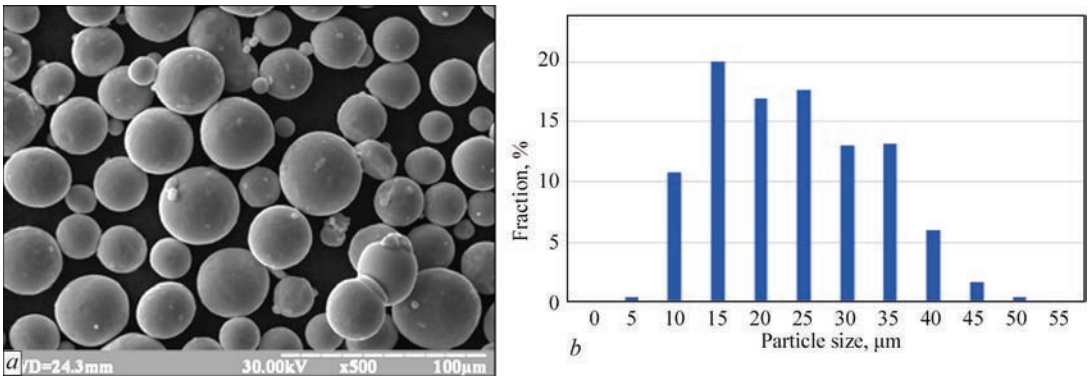

Figure 3. Particles of Ti–6Al–4V initial material at a magnification of 500 (*a*) and results of granulometric analysis (*b*) [16]

The test cylindrical samples for tensile testing with a working zone diameter of 3 mm and a working zone length of 20 mm were produced in the vertical direction (Figure 4). Rational printing parameters were set in [16] with a deposited layer thickness of 40 μm: distance between tracks is 0.03 mm, power is 195 W, beam velocity is 1050 mm/s. Mechanical treatment of samples to finish dimensions was carried out with the use of the HAAS ST10 lathe. The mechanical properties were determined during the tensile test according to the standard procedure in the INSTRON machine.

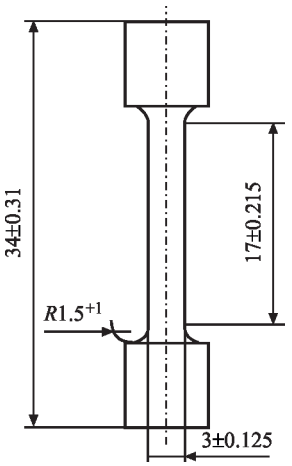

Figure 4. Scheme of location of the place of a controlled stop of printing the test sample

RESEARCH RESULTS

Test samples were made with a full-body part in order to simulate the printing process during operation of the Alfa-150D machine. Depending on the area of a full-body part, there was a pause of different duration between the powder deposition and return of the laser beam, namely: platform 1 — 65 s, platform 2 — 50 s, platform 3 — 80 s, platform 4 — 20 s. On the basis of this simulation, diagrams of the distribution of the printing time of the layer of the working area of the samples were obtained (Figure 5).

From the analysis of the process of samples manufacturing in the working area of the samples (curves along the *Y* axis — 10–20 s, along the *X* axis — layer number 670–787, platforms 3, 4), it was established that with the variable cross-section of parts, the time for the laser to return to the stage of melting the working zone of the samples is reduced by 33 %. It should be noted that during the process of manufacturing parts on the platform 3, printing of the part was completed, and on the platform 4, printing continued without changing the cross-section. From the analysis of the time-layer number dependence, it was established that the completion of printing the main body does not play a role in reducing the time for the laser beam return. Thus, it was established that in the process of

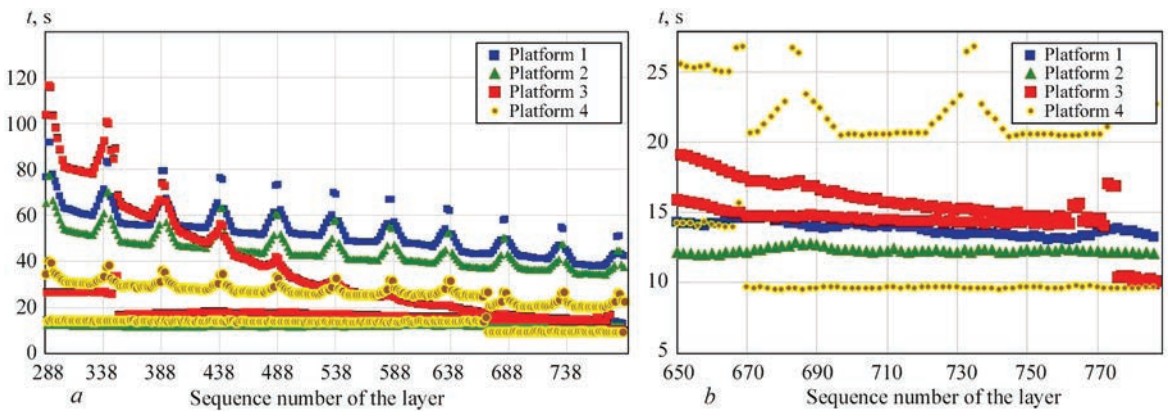

Figure 5. Distribution of time for printing powder layer in the area of the working zone of a tensile sample: *a* — working zone of a test sample from 288 to 787 layer; *b* — working zone of a test sample from 650 to 787 layer; 1 — platform 1; 2 — platform 2; 3 — platform 3; 4 — platform 4

Table 1. Mechanical properties of test samples

Marking	Platform number	Pause duration, s	σ_t, MPa	$\sigma_{0.2}$, MPa	δ, %	ψ, %
1	1	65	1209.7	1093.1	3.3	12.8
2			1168.9	1027.7	3.1	17.6
3			1061.6	997.2	2.0	9.0
4	2	50	1316.1	1178.7	7.0	34.2
5			1313.3	1209.7	7	26.0
6			1305.5	1242.3	9.9	22.3
7	3	80	1237.6	1155.9	4.2	25.0
8			1319.1	1278.8	9.0	28.3
9			1287.5	1201.6	3.2	23.0
10			1316.3	1223.6	5.1	33.9
11			1247.4	1173.0	4.5	28.2
12			1273.3	1188.3	2.1	28.1
13			1342.7	1272.6	7.5	27.3
14	4	20	1380.1	1287.3	2.5	24.3
15			1347.9	1255.7	4.2	23.7
16			1298.9	1178.7	3.6	30.4
17			1345.3	1217.8	4.7	24.3

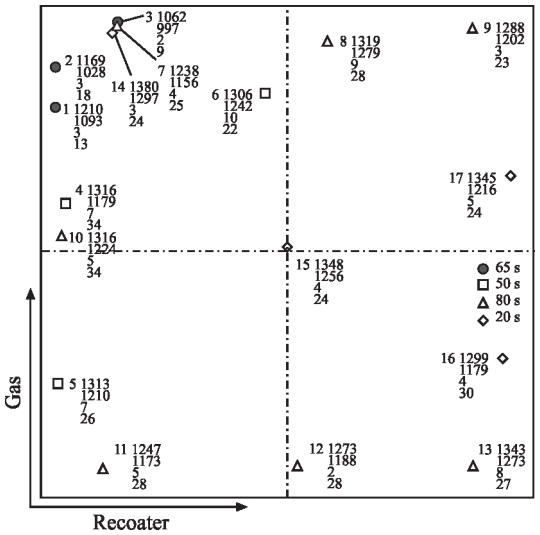

Figure 6. Scheme of samples location on the platform during fabrication: ♦ — 65 s; ● — 50 s; Δ — 80 s; ◊ — 20 s

melting test witness samples, the variable cross-section of a part has a significant influence.

From the results of the analysis of the time-layer number dependence, it was established that the test witness samples of the platforms 1 and 2, depending on the cross-section of a part, are affected by the time of the laser beam return. The printing area of the working zone of the witness sample has a linear nature, and depending on reduction in a part cross-section (platform 2), the change in the time of return is reduced by 18 % for witness samples compared to the platform 1.

Figure 6 shows the location diagram, and the Table 1 shows the values of mechanical properties of the test samples. It should be noted that the samples Nos 3, 7, and 14 were made in the same area of the working platform and differ only in the time of layer deposition and scanning, namely 65, 50 and 20 s, respectively. From the results of research, it was found that with an increase in the time between the deposited layer and the scanning time from 50 s, the strength and ductility characteristics decrease by 23 and 10 %, 33 and 0.7 %, respectively.

As a result of the analysis of the values of mechanical properties, it was established that the strength characteristics of test samples in the area of the inlet nozzle of inert gas blowing have a value by 3–5 % lower compared to the central area of the platform with a range of values of ± 2 %, in the area of the outlet nozzle the value is by 3–5 % lower compared to the central area and have a range of values of ± 10 %. This indicates the influence of the blowing system and the working space loading on the mechanical properties. Thus, it was established that the velocity and circulation of the flow according to the scheme in Figure 2, namely in the area of the output nozzle (Figure 1, *b*), affects obtaining of stable indices of mechanical properties in this area.

CONCLUSIONS

1. As a result of analysis of the values of mechanical properties of the test samples, it was established that their strength characteristics in the area of the inlet nozzle have a value by 3–5 % lower compared to the central area of the platform with a range of values of ± 2 %, in the area of the outlet nozzle, the value is by 3–5 % lower compared to the central area and have a range of values of ± 10 %.

2. It was established that a loading of the working space and the pause between a layer deposition and scanning play a role with an increase in time from 50 s, namely a decrease in the strength and ductility

characteristics at 65 s — 23 and 10 %, 80 s — 33 and 0.7 %, respectively.

3. As a result of research, it was established that a loading of the working space has a significant effect on the mechanical properties compared to the flow rate, but the circulation of the flow plays the greatest role in the area of the outlet nozzle.

REFERENCES

1. Williams, R.J., Piglione, A., Rønneberg, T. et al. (2019) In situ thermography for laser powder bed fusion: Effects of layer temperature on porosity, microstructure and mechanical properties. *Add. Manuf.*, **30**, 100880. DOI: https://doi.org/10.1016/j.addma.2019.100880
2. Grasso, M., Colosimo, B.M. (2017) Process defects and in situ monitoring methods in metal powder bed fusion: A review. *Measurement Science and Technology*, **28**, 044005. DOI: https://doi.org/10.1088/1361-6501/aa5c4f
3. Aage, N., Andreassen, E., Lazarov, B.S., Sigmund, O. (2017) Giga-voxel computational morphogenesis for structural design. *Nature*, **550**, 84–86. DOI: https://doi.org/10.1038/nature23911
4. Wang, P., Song, J., Nai, M.L.S., Wei, J. (2020) Experimental analysis of additively manufactured component and design guidelines for lightweight structures: A case study using electron beam melting. *Addit. Manuf.*, **33**, 101088. DOI: https://doi.org/10.1016/j.addma.2020.101088
5. Adjamskiy, S., Kononenko, G., Podolskyi, R., Badyuk, S. (2022) *Implementation of selective laser melting technology in Ukraine*. Kyiv, Naukova Dumka [in Ukrainian]. DOI: https://doi.org/10.15407/978-966-00-1856-3
6. Fu, D., Li, X., Zhang, M. et al. (2020) Influence of effective laser energy on the structure and mechanical properties of laser melting deposited Ti6Al4V alloy. *Materials (Basel)*, 13(**4**), 962. DOI: https://doi.org/10.3390/ma13040962
7. Gong, H., Gu, H., Zeng, K. et al. (2014) Melt pool characterization for selective laser melting of Ti–6Al–4V pre-alloyed powder. *Solid Freeform Fabrication Sym.*, *Austin Texas*, 256–267. DOI: http://dx.doi.org/10.26153/tsw/15682
8. Amano, H., Ishimoto, T., Suganuma, R. et al. (2021) Effect of a helium gas atmosphere on the mechanical properties of Ti–6Al–4V alloy built with laser powder bed fusion: A comparative study with argon gas. *Add. Manuf.: B*, **48**, 102444. DOI: https://doi.org/10.1016/j.addma.2021.102444
9. Xiao, L., Song, W., Hu, M., Li, P. (2019) Compressive properties and micro-structural characteristics of Ti–6Al–4V fabricated by electron beam melting and selective laser melting. *Mater. Sci. Eng.:A*, **764**, 138204. DOI: https://doi.org/10.1016/j.msea.2019.138204.
10. Herzog, D., Seyda, V., Wycisk, E., Emmelmann, C. (2016) Additive manufacturing of metals. *Acta Mater.*, **117**, 371–392. DOI: https://doi.org/10.1016/j.actamat.2016.07.019
11. Nguyen, D.S., Park, H.S., Lee, C.M. (2018) Effect of cleaning gas stream on products in selective laser melting. *Materials and Manufacturing Processes*, 34(**4**), 455–461. DOI: https://doi.org/10.1080/10426914.2018.1512132
12. Liu, Z., Yang, Y., Wang, D. et al. (2022) Flow field analysis for multilaser powder bed fusion and the influence of gas flow distribution on parts quality. *Rapid Prototyping J.*, 28(**9**), 1706–1716. DOI: https://doi.org/10.1108/RPJ-12-2021-0351
13. Ferrar, L. Mullen, E. Jones, R. Stamp, C.J. Sutcliffe (2012) Gas flow effects on selective laser melting (SLM) manufacturing performance. *J. Materials Proc. Technology*, 212(**2**), 355–364. DOI: https://doi.org/10.1016/j.jmatprotec.2011.09.020
14. Zhao, C., Fezzaa, K., Cunningham, R.-W. et al. (2017) Real-time monitoring of laser powder bed fusion process using high-speed X-ray imaging and diffraction. *Sci. Rep.*, **7**, 3602. DOI: https://doi.org/10.1038/s41598-017-03761-2.
15. Hiroshi, N., Yousuke, K., Koji, N., Seiji, K. (2015) Elucidation of melt flows and spatter formation mechanisms during high power laser welding or pure titanium. *J. Laser Appl.*, **27**, 032012. DOI: https://doi.org/10.2351/1.4922383.
16. Adjamskyi, S.V., Kononenko, G.A., Podolskyi, R.V. (2022) Influence of heat treatment of specimens from Ti6Al4V manufactured by the technology of selective laser melting on structure and mechanical properties. *The Paton Welding J.*, **9**, 21–26. DOI: https://doi.org/10.37434/tpwj2022.09.04

ORCID

S.V. Adzhamskyi: 0000-0002-6095-8646,
G.A. Kononenko: 0000-0001-7446-4105,
R.V. Podolskyi: 0000-0002-0288-0641,
S.I. Badyuk: 0000-0002-1074-3057

CONFLICT OF INTEREST

The Authors declare no conflict of interest

CORRESPONDING AUTHOR

R.V. Podolskyi
LLC “Additive Laser Technology of Ukraine”
31v Str. Serhiy Podolynskyi, 49000, Dnipro, Ukraine
E-mail: info@alt-print.com

SUGGESTED CITATION

S.V. Adzhamskyi, G.A. Kononenko, R.V. Podolskyi, S.I. Badyuk (2023) Influence of blowing and loading of working space on mechanical properties of samples manufactured using SLM technology. *The Paton Welding J.*, **12**, 19–23.

JOURNAL HOME PAGE

https://patonpublishinghouse.com/eng/journals/tpwj

Received: 23.10.2023
Accepted: 26.12.2023

‘DOI: https://doi.org/10.37434/tpwj2023.12.03

METAL-CORED WIRES BASED ON TITANIUM AS MATERIALS FOR ADDITIVE MANUFACTURING OF PARTS

S.L. Schwab[1], R.V. Selin[1], S.V. Akhonin[1], M.M. Voron[2], D.V. Kovalchuk[3]

[1]E.O. Paton Electric Welding Institute of the NASU
11 Kazymyr Malevych Str., 03150, Kyiv, Ukraine
[2]Physico-TechnologicaI Institute of Metals and Alloys of the NASU
34 Acad. Vernadskyi Blvd., 03142, Kyiv, Ukraine
[3]PJSC “NVO ”Chervona Hvilya”
28 Dubrovytska Str., 04114, Kyiv, Ukraine

ABSTRACT

The paper shows the possibility of manufacturing metal-cored wires based on high-strength titanium alloys of different compositions (Ti–5Al–5Mo–5V–1Fe–1Cr and Ti–5Al–5Mo–5V–4Nb–1.5Cr–1Fe–2.5Zr systems), an alloy based on medical grade titanium (Ti–13Zr–13Nb system) and structural titanium VT6 alloy (Ti–6Al–4V system), reinforced with TiC particles. The technological moments of the experimental production of metal-cored wires by the method of drawing and subsequent pulling are shown. A study was conducted on using these materials as a filler metal in WAAM technology both in the methods of argon arc as well as electron beam surfacing.

KEYWORDS: high-strength titanium alloys, metal-cored wire, WAAM, TIG, xBeam 3D Metal Printing

INTRODUCTION

Additive manufacturing technologies became an alternative to conventional methods of part manufacturing with high added cost, including those, related to aerospace industry, and biomedical products, which require very complex and individual approaches at small volumes. Additive manufacturing allows producing these necessary component parts in a short time at a constant cost.

Among different materials titanium-based alloys are more and more often used in Wire Arc Additive Manufacturing (WAAM) method due to their application in the aerospace industry for fabrication of airframe structures. Strong, such as Ti–6Al–4V (VT6), and high-strength two-phase titanium alloys are in great demand in the aerospace industry, due to their high specific strength, corrosion resistance, damage resistance and compatibility with composite materials from graphite fiber [1]. Among the different accessible approaches, the WAAM process has a number of advantages over other 3D printing technologies, including the high coefficient of material utilization (99 % [2]) and energy efficiency (~ 70 % [3], lower capital equipment costs, and high productivity of the printing process [4].

At present, there are a number of titanium-based solid wires, produced by industry. Commercial wires from pure titanium are used as filler material for TIG welding of parts from titanium alloys with a low content of alloying elements. There are also solid wires based on titanium with a higher content of alloying elements. Ultimate strength of metal of such wires is not higher than 870 MPa. Manufacture of sound solid wires from high-strength titanium alloys is very complicated, as higher strength of the metal does not allow producing wires without defects. Attempts at producing wires from Ti–5Al–5Mo–5V–1Fe–1Cr alloy (VT22), with higher than 1000 MPa strength, were made earlier [5]. Cracks and tears were found on this wire surface, which can be a source of deposited metal contamination, and, consequently, deterioration of its quality. That is why there is no commercial production of wires from high-strength titanium alloys.

Despite a large number of studies on part manufacturing by WAAM method, the majority of them are focused only on producing parts with solid wire application. Investigations on flux-cored wire application to produce parts from high-strength titanium alloys by this method are practically absent. Flux-cored wire application to produce parts by WAAM method allows manufacturing parts from high-strength titanium alloys and greatly increasing the range of titanium alloys, which can be used to make parts by this method.

One of the important and complex technological properties in metal-cored wire manufacture is preparation of their core, namely the metal component, i.e. the powder proper. At present in Ukraine there are two methods to produce titanium-based powders.

By the first method crushing of alloyed titanium is performed using the method of thermochemical

Copyright © The Author(s)

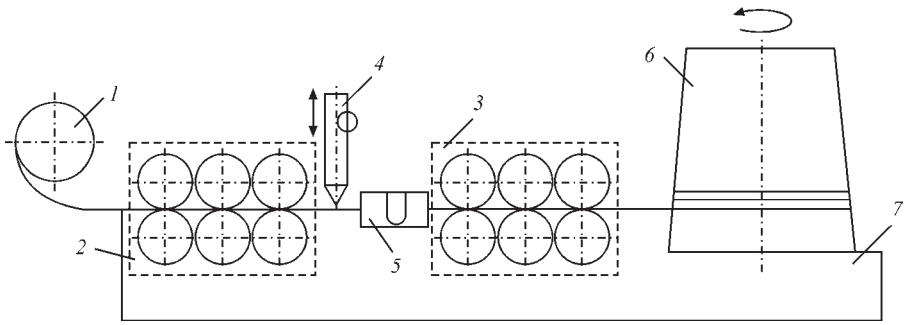

Figure 1. Schematic of a drawing machine for producing titanium flux-cored wire: *1* — cassette; *2*, *3* — roller stands; *4* — dosing unit; *5* — U-shaped strap; *6* — drum; *7* — page

embrittlement with hydrogen application — Hydrogenation-Dehydrogenation (HDH) method [6]. In this process the metal blocks of titanium are subjected to hydrogenation to increase titanium brittleness. Brittle titanium block is crushed mechanically and sieved by fractions. The totality of technological solutions for production of such titanium powders allows producing a denser material with a lower content of impurities, which increases the powder quality and improves its morphology.

Another process to produce powders based on titanium alloys is the method of plasma atomization of the billet — Plasma Rotating Electrode Process (PREP) [7]. The method consists in the following: the electrode of the alloy which is sputtered, turns around a horizontal axis, and its free end is melted by the plasmatron. The molten metal drops fall off the rotating electrode, and crystallize in free flight before colliding with the sputtering chamber walls. The chamber, where the electrode rotates and atomization occurs, should have an atmosphere protecting from oxidation. It allows producing powders with a high surface purity. Powder particles are smooth and spherical, and the average particle size is 200 μm, the yield of particles of 50 to 500 μm size is equal to 75 %. One of the advantages of powders produced by this method is their high fluidity and purity (low oxygen content) [8].

THE OBJECTIVE OF THE WORK,

considering the complexity of making sound solid wires based on strong and high-strength titanium alloys, was production and application of metal-cored wires based on these alloys for additive manufacturing of parts, where powders prepared by HDH and PREP methods, are used as the core.

RESULTS AND THEIR DISCUSSION. PRODUCING METAL-CORED WIRE

Development and production of titanium alloy based metal-cored wires is performed by the methods of drawing and subsequent pulling through the dies in a unit designed for producing of titanium flux-cored wires (Figure 1). Used as the sheath is 0.2 mm titanium foil of VT1-00 grade. Depending on powder type, the respective charge dosing unit is used. When using powder, produced by PREP method, the granules inside the formed tube are not in a sufficiently good contact. That is why, when the arc hits such a wire, the granules are released, and a greater part of them does not fall into the weld pool, but sticks to the tungsten electrode, disturbing the process stability. For this reason, their shape is changed before that through deformation.

Charge dosed feeding into the formed tube is performed through the guide nozzle of the dosing hopper, equipped with a gate regulator (Figure 2, *a*). To ensure prior compacting of the charge, and the required value of overlapping of the strip edges, a rotating die is used, which is mounted after the last pair of forming rollers. The direction of the die rotation should coincide with the direction of strip overlapping for tube closing (Figure 2, *b*, c). Further pulling of the formed

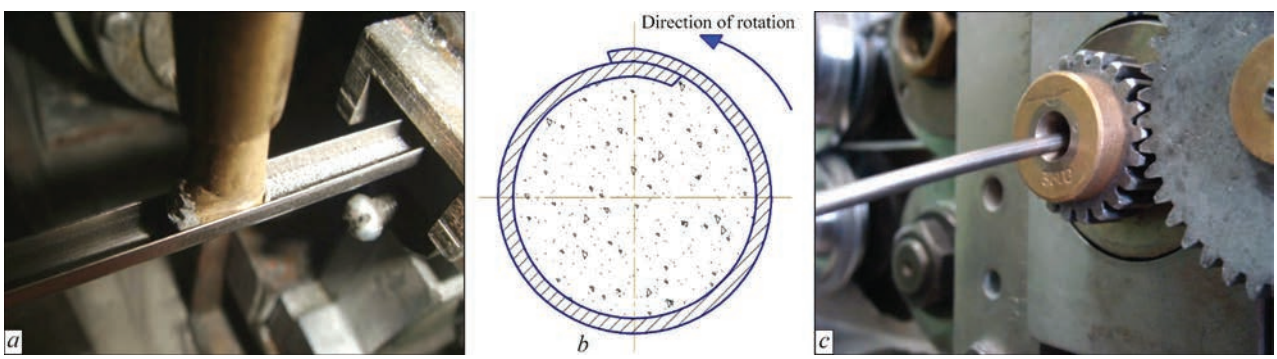

Figure 2. Process of forming and further pulling of metal-cored wire: *a* — charge dosing; *b* — sheath closing scheme; *c* — rotating die

Table 1. Chemical composition of VT22 titanium alloy, wt.% (GOST 19807–91)

Ti	Al	V	Mo	Fe	Cr	[O]	[H]	[N]
Base	4.4–5.7	4.0–5.5	4.0–5.5	0.5–1.5	0.5–2.0	0.18	0.015	0.05

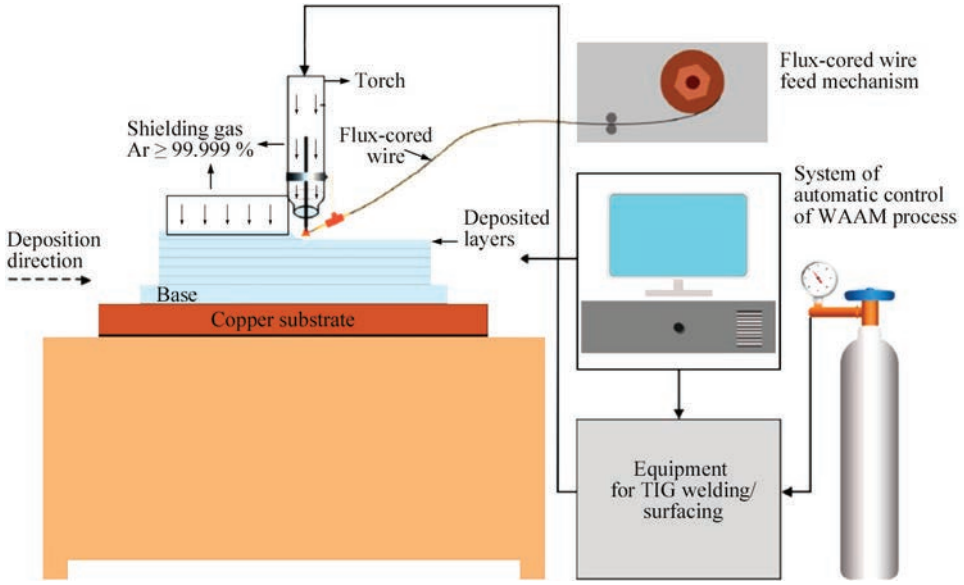

Figure 3. Schematic of a unit for layer-by-layer TIG deposition using metal–cored filler wire

wire is conducted using a set of dies, with 0.1 mm step. The wire is fed into the die so that it is positioned with the seam facing outside on the drum, as tension of outer fibers leads to additional closure of the seam, and prevents distortion (corrugation).

APPLICATION OF METAL-CORED WIRE BASED ON VT22 TITANIUM ALLOY

A 2.9 mm metal-cored wire based on VT22 titanium alloy of PPT-22 grade with fill factor of 65 % was developed earlier [9]. This wire core includes powder of high-strength VT22 titanium alloy and flux of CaF_2–SrF_2–BaF_2 system in the amount of 7 % relative to the filler. This wire is designed for TIG welding and surfacing of VT22 titanium alloy.

This wire was also applied as filler wire at multilayer deposition. Experimental three-layer deposition was performed, using the produced filler wire with granules of high-strength VT22 titanium alloy. Deposition of high-strength titanium alloys is made difficult, primarily, by their high content of alloying elements, such as aluminium, vanadium and molybdenum (Table 1). More over, compared to regular alloys these titanium alloys are more sensitive to interstitial impurities, such as nitrogen and carbon, as the solubility of the latter in BCC lattice of titanium β-phase is much lower. They are more prone to development of chemical and physical heterogeneity in the cast metal and HAZ during deposition, which may result in formation of brittle interlayers. Correct selection of deposition modes in most cases allows producing sound welded joints of high-strength titanium alloys.

The deposition process was conducted in the unit for TIG welding/surfacing titanium alloys, which was adapted for the process of layer-by-layer deposition (Figure 3). The deposition process was conducted in the following mode: I_w = 200 A, U_a = 12 V, V_w = 8 m/h, V_f = 30 m/h; L_a = 4 mm.

Experimental deposition using the produced wire demonstrated a stable running of the process (without spilling of unmelted granules), which pointed to sufficient density of the charge and its uniform distribution

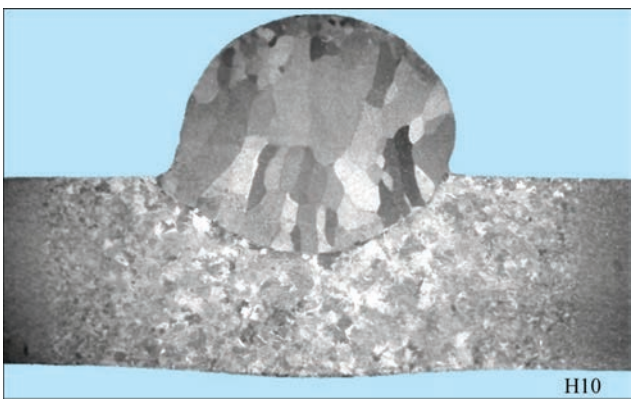

Figure 4. Macrosection of the produced three-layer sample made with flux-cored filler wire based on titanium alloy VT22

Figure 5. Roentgenogram of the deposited sample

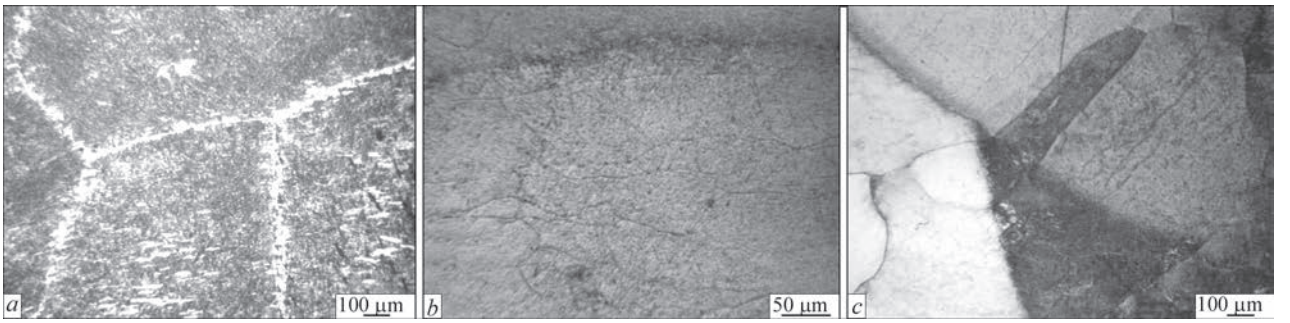

Figure 6. Microstructure of a three-layer sample made with application of flux-cored filler wire based on VT22 titanium alloy: *a* — base metal; *b* — weld metal; *c* — fusion zone

along the wire length. As a result, a sound three-layer sample (Figure 4) without any pores along its entire length (Figure 5) was produced.

VT22 alloy, on which TIG welding was performed with flux-cored wire application, consists of large polyhedral primary β-grains. Alongside equilibrium grains, non-equilibrium grains are present in the base metal structure, and the grain shape factor (grain length to width ratio) is in the range of 1–3, grain width being 1–2.5 μm (Figure 6, *a*).

In the deposited metal the degree of alloying by β-stabilizing elements is somewhat lower compared to VT22 alloy due to weld metal dilution by commercial titanium of the flux-cored wire sheath. It most probably leads to precipitation of dispersed particles of α′-phase from β-solid solution. Formation of a fold in β-grains is probably attributable to delamination of β-solid solution into volumes enriched and depleted in certain alloying elements. Formation of a substructure is observed in the weld metal (Figure 6, *b*). Substructure appearance is attributable to polygonization under the impact of internal stresses in the welded joint. Residual stresses are caused by temperature gradients, phase transformations in the heating zone at welding thermal cycle, as well as processes of liquid metal solidification in the weld area. At substructure formation, rotation of individual volumes of coarse β-grain to a small angle relative to another one, takes place. Presence of a subgranular structure promotes increase of strength and lowering of ductility. Intensity of β-phase decomposition in the HAZ is much lower than that in the weld, which is indicative of higher stability of β-solid solution in VT22 alloy than in the weld metal, due to a high content of β-stabilizing elements (Figure 6, *c*).

After mechanical testing the deposited sample ultimate strength, equal to 1025 MPa, was determined. Gas content in the deposited metal is not higher than their permissible values in the base metal; [O] = 0.098 wt.%, [H] = 0.0027 wt.%, [N] = = 0.014 wt.%.

APPLICATION OF METAL-CORED WIRE BASED ON TITANIUM ALLOY T120

Multilayer samples were also produced using flux-cored filler wire based on high-strength titanium alloy T120 (Ti–5Al–5Mo–5V–4Nb–1.5Cr–1Fe–2.5Zr system), developed at PWI [11]. 2.2 mm metal-cored wire with 50 % fill factor was used as the filler. This wire core was from powder of T120 titanium alloy, produced by HDH method. Deposition was performed by nonconsumable electrode argon-arc process (Figure 2) in the following mode: I_w = 160–180 A, U_a = 12 V, V_w = = 6 m/h, V_f = 40–45 m/h, L_a = 2 mm. A five-layer sample was produced as a result of the conducted work (Figure 7).

Deposited metal ultimate strength is equal to 878.7 MPa, impact toughness is 15.1 J/cm^2, which is much lower than the values of base metal mechanical characteristics: σ_t = 1145.8 MPa, KCV = 30.6 J/cm^2. This is attributable to presence of pores in the deposited metal. In order to prevent pore initiation in the deposited metal, it is necessary to introduce the flux component into the core metal. The high-strength two-phase titanium alloys and the produced joints of these alloys are also subjected to mandatory heat treatment, which, in its turn, allows improving the level of mechanical characteristics [12].

APPLICATION OF METAL-CORED WIRE BASED ON Ti–13Zr–13Nb TITANIUM ALLOY

Titanium alloy application in endoprosthetics has been the most intensively developing over the last thirty

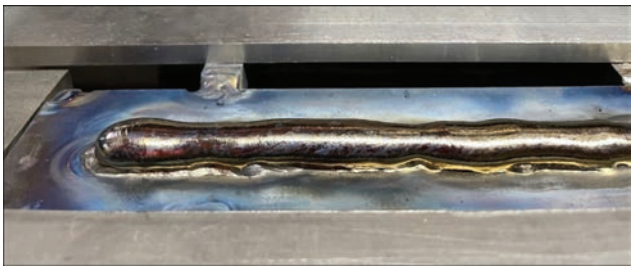

Figure 7. General view of a five-layer sample after the process of deposition with flux-cored filler wire based on T120 titanium alloy

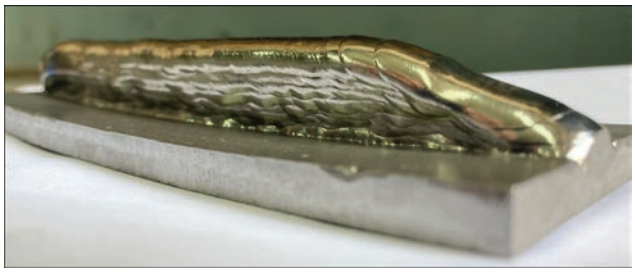

Figure 8. General view of a nine-layer sample after the process of deposition with metal-cored filler wire based on Ti alloy of Ti–Zr–Nb system

years due to unique characteristics of their biocompatibility and the most optimal combination of mechanical and biomechanical properties [13]. The main requirements to manufacturers of titanium alloys for medical purposes include a complex of mechanical properties: low modulus of elasticity, high strength and fatigue fracture resistance. Such a characteristic as modulus of elasticity deserves special attention. Over the recent years, the need to produce alloys for endoprostheses with a low modulus of elasticity has become important, which is related to application of cementless fixation of prostheses and lowering the risks of development of diaphyseal dysplasia and bone fracture after long-term use of the prostheses. These are exactly β-alloys which often have the modulus of elasticity lower than the values for (α+β)-alloys for medical purposes, while being characterized by a high strength. Nontoxic alloying elements are β-stabilizers of titanium or alloy strengthening elements. Therefore, one can judge the wide possibilities for their application in different concentration ranges exactly for creation of biocompatible titanium alloys [14, 15]. Zirconium-containing titanium alloys and ternary Ti–Zr–Nb alloys have the most promising combination of strength and modulus of elasticity. Binary Ti–Zr alloys are characterized by strength in the range of 600–1450 MPa and modulus of elasticity of 72–110 GPa, while Ti–Zr–Nb compositions have the strength in the range of 600–1000 MPa and modulus of elasticity in the range of 58–80 GPa, which is much better than the combination of the same parameters in VT6 alloy [16].

Having analyzed the urgency of application of low-modulus titanium alloys for endoprosthetics and technologies of manufacturing finished products from them, which envisage availability of rods for fixation, or other loaded and massive elements, a conclusion was made about the rationality of WAAM method as an alternative to the currently-available additive manufacturing methods. To achieve the defined objective, a metal-cored wire was developed (3.0 mm diameter, 62 % fill factor), where the core is a powder of 50–70 μm size from titanium alloy of Ti–13Zr–13Nb system. The powder was produced earlier by HDH process.

The produced metal-cored wire based on a titanium alloy for medical purposes was used to conduct multilayer TIG deposition in a predefined mode: I_w = 210 A, U_a = 12.7 V, V_w = 8 m/h, V_f = 34 m/h, L_a = 3.5 mm. As a result, a nine-layer sample was produced (Figure 8).

The deposit height is 15.2 mm, and width is 11.8 mm. At present, analysis of the produced sample metallography, assessment of its mechanical properties (ultimate strength and modulus of elasticity) and determination of gas content in the deposited metal are performed.

APPLICATION OF METAL-CORED WIRE BASED ON Ti–6Al–4V–40 % TiC POWDER

Some of the few disadvantages of titanium alloys are their low hardness and insufficient wear resistance during operation of structures made from them. Such disadvantages can be overcome by development of titanium-based metal matrix composites, reinforced by hard high-modulus phases. One of such examples is reinforcement of the titanium alloy matrix by high-modulus and light particles of titanium carbide (TiC) [17]. To improve the dispersity and homogeneity of titanium carbide powders, they are made by powder metallurgy method [18].

Both in the case of high-strength titanium alloys, and of alloys reinforced by hard particles, there is the problem of producing solid section wires. So, the objective was to obtain metal-cored wire based on strong VT6 alloy (Ti–6Al–4V system), reinforced by

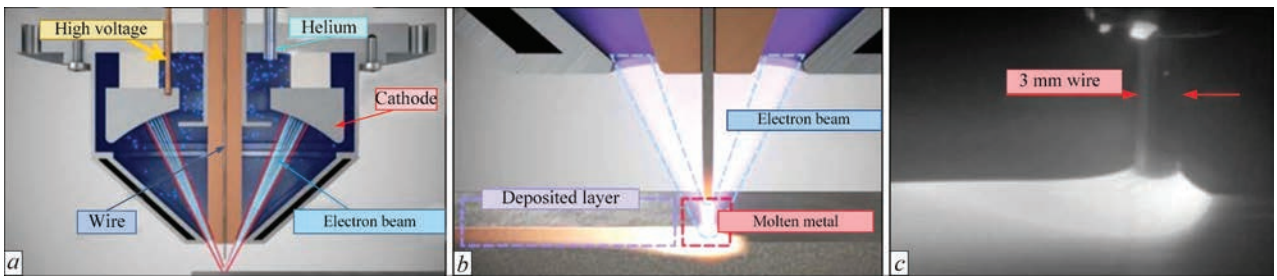

Figure 9. Configuration of xBeam® 3D Metal Printing process: xGun design schematic (*a*); configuration of a heated zone in the feeding point during deposition (*b*); photo of the actual deposition process (*c*) [21]

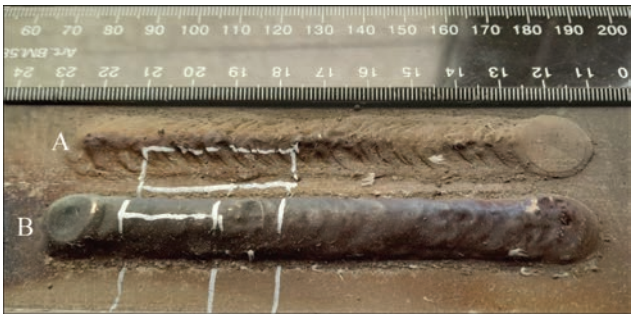

Figure 10. General view of the samples: A — single-layer; B — multilayer

TiC particles. As a result of experiments, test wire of 3.0 mm diameter (fill factor of 62 %) with a core from Ti–6Al–4V + 40 % TiC powder was produced.

Advanced additive manufacturing technology called xBeam 3D Metal Printing (Figure 9), developed by "Chervona Hvilya" Company [19] demonstrated the possibility of manufacturing titanium alloy products with a controlled microstructure, stochiometric chemical composition and also with desirable mechanical characteristics [20]. Deposition with experimental wire was conducted by this technology.

By the results of experiments on 3D printing using metal-cored wire, single- and multilayer samples were produced (Figure 10).

One of the essential advantages of xBeam process is the possibility of simultaneous melting of the filler wire and the substrate, due to the peculiarities of the electron beam. However, at application of metal-cored wire as the filler, part of the electron beam hitting the wire, instantly melted its thin sheath, resulting in the powder being released, scattered and not coming to the weld pool. For this reason, not all the powder, but just part of it got into the weld metal, leading to deviations from the predicted chemical composition of the deposited bead metal. More over, the spilled powder partially penetrated into the electron gun discharge chamber and onto the cathode, leading to failures, which considerably improved the deposition process stability, resulting in an even greater deterioration of the uniformity of TiC component distribution in the deposited metal.

In order to prevent the abovementioned problems, the configuration of relative placement of process elements (profiled electron beam, wire and substrate) was set up so that the electron beam did not directly fall on the wire. For this purpose the substrate was placed closer to the gun. In this configuration, all the electron beam energy hit the substrate, creating a wider and deeper melt pool, than it is usually done using solid section wire. Thus, the flux-cored wire was immersed into the molten pool and melted there, while preserving the sheath in the solid state above the pool during the entire melting process. Due to that, the sheath prevented powder release before it entered the liquid metal of the weld pool. This solution ensured a rather stable process of wire melting. Yet such a solution became possible under the condition of excess heat input into the substrate. However, the influence of such an overheating on the structure still needs to be studied.

CONCLUSIONS

Development of metal-cored wires based on titanium alloys for different purposes solves a relevant problem in the field of modern additive technologies, namely their application allows producing sound multilayer samples. The proposed metal-cored filler wires based on high-strength titanium alloys, as well as alloys for medical purposes, can be used as filler materials in additive manufacturing of parts from titanium alloys both at TIG, and at electron beam 3D printing processes.

REFERENCES

1. Martina, F., Colegrove, P.A., Williams, S.W., Meyer, J. (2015) Microstructure of interpass rolled wire + arc additive manufacturing Ti–6Al–4V components. *Metall. Mater. Transact. A*, 46(**12**), 6103–6118. DOI: https://doi.org/10.1007/s11661-015-3172-1
2. Ríos, S., Colegrove, P.A., Martina, F., Williams, S.W. (2018) Analytical process model for wire + arc additive manufacturing. *Addit. Manuf.*, **21**, 651–657. DOI: https://doi.org/10.1016/j.addma.2018.04.003
3. Bekker, A.C.M., Verlinden, J.C. (2018) Life cycle assessment of wire + arc additive manufacturing compared to green sand casting and CNC milling in stainless steel. *J. Clean. Prod.*, **177**, 438–447. DOI: https://doi.org/10.1016/j.jclepro.2017.12.148
4. Lütjering, G., Williams, J.C. (2007) *Titanium.* 2nd Ed. Springer, Berlin, Heidelberg, Germany.
5. Akhonin, S.V., Schwab, S.L. (2019) Filler flux-cored wire for TIG welding and surfacing of VT22 titanium alloy. *The Paton Welding J.*, **6**, 34–37. DOI: https://doi.org/10.15407/tpwg2019.06.06
6. Yanko, T.B., Ovchinnikov, A.V., Lyutyk, N.P., Korzhyk, V.N. (2018) Technology for obtaining of plasma spheroidised HDH titanium alloy powders used in 3D printing. *Technological Systems*, 85(**4**), 36–41. DOI: http://dx.doi.org/10.29010/085.7
7. Sun, P., Fang, Z.Z., Zhang, Y., Xia, Y. (2017) Review of the methods for production of spherical Ti and Ti alloy powder. *JOM*, 69(**10**), 1853–1860. DOI: https://doi.org/10.1007/s11837-017-2513-5
8. Koshelev, V.Ya., Kuznetsov, V.A., Sukhov, D.I. (2010) To problem of manufacturing of granules of less than 200 μm coarseness from titanium alloys by plasma melting method and centrifugal spraying of cast billet. *Tekhnologiya Lyogkikh Splavov*, **2**, 44–48 [in Russian].
9. Schwab, S., Selin, R., Voron, M. (2023) Welding materials for TIG welding, surfacing, and WAAM technology of titanium alloys. *Welding in the World*, 67(**4**), 981–986. DOI: https://doi.org/10.1007/s40194-023-01464-z
10. Schwab, S., Selin, R., Voron, M. (2023) Welding materials for TIG welding, surfacing, and WAAM technology of titanium

alloys. *Avtomatychne Zvaryuvannya*, **3**, 10–14. DOI: https://doi.org/10.37434/as2023.03.02
11. Akhonin, S.V., Selin, R.V., Berezos, V.A. et al. (2016) Development of new high-strength titanium alloy. *Sovrem. Elektrometall.,* **4**, 22–27. DOI: https://doi.org/10.15407/sem2016.04.04
12. Prilutsky, V.P., Akhonin, S.V., Schwab, S.L., Petrychenko, I.K. (2018) Effect of heat treatment on the structure and properties of titanium alloy VT22 welded joints produced by TIG welding with flux-cored wire. *Materials Sci. Forum*, **927**, 119–125. DOI: https://doi.org/10.4028/www.scientific.net/MSF.927.119
13. Shunxing, L. (2020) Review of the design of titanium alloys with low elastic modulus as implant materials. *Advanced Engineering Materials*, 22(**11**). DOI: https://doi.org/10.1002/adem.202000555
14. Niinomi, M. (2011) *Low modulus titanium alloys for inhibiting bone atrophy*: Biomaterials Science and Engineering. Ed. by R. Pignatello, 249–268.
15. Voron, M., Schwab, S., Selin, R. (2022) Modern approaches in development of biocompatible titanium alloys with higher level of service properties. *Metal ta Lyttya Ukrainy*, 30(**2**), 88–95. DOI: https://doi.org/10.15407/scin15.04.005
16. Xiatong, B. et al. (2022) Exploring the limits of mechanical properties of Ti–Zr binary alloys. *Materials Letters*, **318**, 132091. DOI: https://doi.org/10.1016/j.matlet.2022.132091
17. Miracle, D. (2005) Metal matrix composites – From science to technological significance. *Composites Sci. and Technology*, 65(**15–16**), 2526–2540. DOI: https://doi.org/10.1016/j.compscitech.2005.05.027
18. Ivasishin, O.M., Markovsky, P.E., Savvakin, D.G. et al. (2019) Multi-layered structures of Ti–6Al–4V alloy and TiC and TiB composites on its base fabricated using blended elemental powder metallurgy. *J. Mater. Proc. Technol*., **269**, 172–181. DOI: https://doi.org/10.1016/j.jmatprotec.2019.02.006
19. Kovalchuk, D., Melnyk, V., Melnyk, I., Tugai, B. (2016) Prospects of application of gas-discharge electron beam guns in additive manufacturing. *J. of Elektrotechnica & Elektronica (E+E)*, 51(**5–6**), 37–43.
20. Kovalchuk, D., Melnyk, V., Melnyk, I. et al. (2021) Microstructure and properties of Ti–6Al–4V articles 3D-printed with co-axial electron beam & wire technology. *J. of Materials Eng. and Performance*, 30(**7**), 5307–5322. DOI: https://doi.org/10.1007/s11665-021-05770-9
21. Kovalchuk, D., Melnyk, V., Melnyk, I. (2022) A coaxial wire-feed additive manufacturing of metal components using a profile electron beam in space application. *J. of Materials Eng. and Performance*, 31(**8**), 6069–6082. DOI: https://doi.org/10.1007/s11665-022-06994-z

ORCID
S.L. Schwab: 0000-0002-4627-9786,
R.V. Selin: 0000-0002-2990-1131,
S.V. Akhonin: 0000-0002-7746-2946,
M.M. Voron: 0000-0002-0804-9496,
D.V. Kovalchuk: 0000-0001-9016-097X

CONFLICT OF INTEREST
The Authors declare no conflict of interest

CORRESPONDING AUTHOR
S.L. Schwab
E.O. Paton Electric Welding Institute of the NASU
11 Kazymyr Malevych Str., 03150, Kyiv, Ukraine
E-mail: serg.schwab@gmail.com

SUGGESTED CITATION
S.L. Schwab, R.V. Selin, S.V. Akhonin, M.M. Voron, D.V. Kovalchuk (2023) Metal-cored wires based on titanium as materials for additive manufacturing of parts. *The Paton Welding J*., **12**, 24–30.

JOURNAL HOME PAGE
https://patonpublishinghouse.com/eng/journals/tpwj

Received: 20.10.2023
Accepted: 26.12.2023

DOI: https://doi.org/10.37434/tpwj2023.12.04

STUDY OF THE INFLUENCE OF FDM 3D PRINTING PARAMETERS ON FORMATION PROCESSES, STRUCTURE AND PROPERTIES OF POLYLACTIDE PRODUCTS

O.P. Masiuchok, M.V. Iurzhenko, R.V. Kolisnyk, A.O. Shadrin, V.Yu. Kondratenko, M.G. Korab

E.O. Paton Electric Welding Institute of the NASU
11 Kazymyr Malevych Str., 03150, Kyiv, Ukraine

ABSTRACT

Based on the results of mathematical modeling and theoretical research works, it was established that the most influential factors of 3D printing, affecting the quality and time of end products formation, are extruder die temperature, layers height, speed of printing head movement when forming products, as well as simultaneous fabrication of several products within one cycle. In the work, the modes of the FDM 3D printing process were worked out and the regularities of the influence of the mentioned parameters on the structure and properties of resulted 3D polylactide products were established. The parameters of product formation were experimentally determined, which provide the production of 3D objects with predicted properties: maximum strength (98 % of filament strength), high aesthetic quality (surface smoothness and resolution) and products with minimal investments of time during their production.

KEYWORDS: additive formation, FDM 3D printing technology, polylactide, functional 3D product, filament

INTRODUCTION

Recently, the development of three-dimensional (3D) printing technologies has become explosive [1–3]. Among them, one of the most widespread is the technology of modeling by the deposition method (Fused Deposition Modeling, FDM) [4–6]. On the other hand, in the world (in view of aggravated problem of environmental pollution), the use of biodegradable polymer materials is gaining momentum [7]. Among such materials, a special place belongs to polylactide (PLA) — thermoplastic polyester based on lactic acid, suitable in particular for food packaging [8, 9]. The creation of products from such material, including with the help of 3D printing, is promising for a number of industries. For the research, PLA filament from the MonoFilament Company was chosen [10].

Since FDM 3D printing is a complex process with a great number of parameters that can affect the structure and properties of end products, at the first stage, mathematical modeling of a simplified FDM 3D printing process was carried out in order to reduce the number of experiments to determine its most influential parameters [11].

Thus, taking into account the results of mathematical modeling, which are correlated with the data of literary sources [12, 13], it can be assumed that the basic parameters of the FDM 3D printing process, which affect the quality of end products, include:

- temperature of FDM 3D printing, i.e. extruder die;
- speed of the printing head movement when forming a product;
- layers height (in a certain sense, the volume and mass of the polymer) deposited when forming a product;
- quantity of products formed within one 3D printing cycle.

To experimentally determine the influence of each of these FDM 3D printing parameters on the quality of end products in the work, all samples had the shape of a blade for mechanical research with the cross-sectional dimensions of the thinnest part being 2×4 mm. The total size of the part was 30×6×2 mm. The location of the model relative to the working platform was chosen in a vertical orientation due to the anisotropy of mechanical properties of a formed 3D product along the *X*, *Y*, *Z* axes, since the adhesion strength between the layers can be comparable, but not higher than the strength of the base material.

EFFECT OF 3D PRINTING TEMPERATURE ON THE FORMATION PROCESS AND THE QUALITY OF END POLYMER PRODUCTS

In this part of the work, experimental 3D printing of samples was carried out using commercial PLA filament at five different extruder temperatures — 190, 200, 210, 220 and 230 °C, which are located in the temperature range recommended for similar works by the manufacturing company (190–230 °C). The results of mechanical uniaxial tension tests are presented in Figure 1.

Copyright © The Author(s)

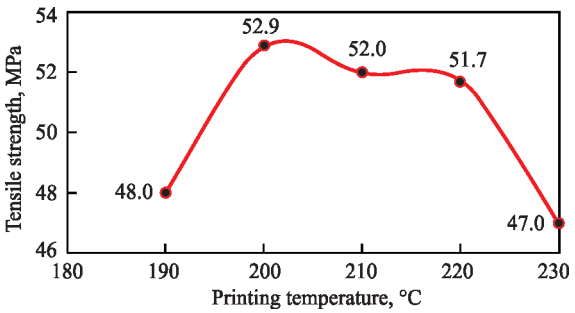

Figure 1. Dependence of mechanical interlayer strength of samples from PLA on temperature of their 3D printing

It is known that shrinkage of the heated polymer after cooling is stronger, the higher the printing temperature. As is seen from Figure 1, the formation of PLA products at a temperature of 200 °C made it possible to subject thermoplastic polymer material to as little thermal expansion as possible. At the same time, layer-by-layer formation of a product with a preset geometric shape and the highest mechanical interlayer strength σ = 52.9 MPa at the strength of PLA itself σ = 57.8 MPa occurred [14]. At a reduced temperature (190 °C), products of a preset geometric shape were formed, but the value of the interlayer strength was σ = 48 MPa, which is explained by the high viscosity of the PLA melt at this temperature and, accordingly, low adhesive ability. Printing of products with an elevated extruder temperature of 230 °C led to a slight deformation and a low interlayer strength at the level of σ = 47 MPa due to overheating of samples during their formation.

INFLUENCE OF THE 3D PRINTING SPEED ON THE FORMATION PROCESSES, APPEARANCE, STRUCTURE AND PROPERTIES OF END POLYMER PRODUCTS

Applying the technology of FDM 3D printing from polylactide, the samples with all the constant parameters of product formation were fabricated, which were described above and correspond to the recommendations of the manufacturing company except for the speed of the head movement when forming products. The MonoFilament Company recommends forming products from PLA plastic at a speed of the printing head movement in the range of 30–80 mm/s, while other manufacturers advise to do that at a speed in the range of 40–110 mm/s [10, 15]. In order to reasonably and objectively determine the influence of different speeds (within the recommended limits) on the quality of fabricated products and to find the optimal speed that ensures the fabrication of the highest quality product, the samples were formed with an interval of 30 mm/s from the lowest to the highest recommended limit. The speed of the printing head movement when forming products was 20, 50, 80, 110 mm/s for the samples Nos 1–4, respectively. The time spent on the formation of each blade varied from 14 to 22 min, depending on the chosen speed of forming products.

After conducting the research and processing of the obtained data, it was determined that the speed of products formation within the studied limits and at keeping other printing parameters constant does not significantly affect the appearance (Figure 2). All the formed samples had a preset geometric shape with clear outlines of a part and a visually high density of the deposited layers adhesion.

The dense inner structure of the produced samples and the absence of defects in them that exceed 5 μm are also demonstrated by pictures made while studying the products using a computer tomography and 3D reconstruction of their inner structure (Figure 3). It was established that the inner structure was typical for all samples, despite the different speed of the printing head movement when forming products. For example, Figure 3 shows the structure in the *X*, *Y*, and *Z* planes of the sample, formed at a maximum speed of 110 mm/s.

To study the influence of the speed of the printing head movement when forming samples on the mechanical characteristics of fabricated products, the

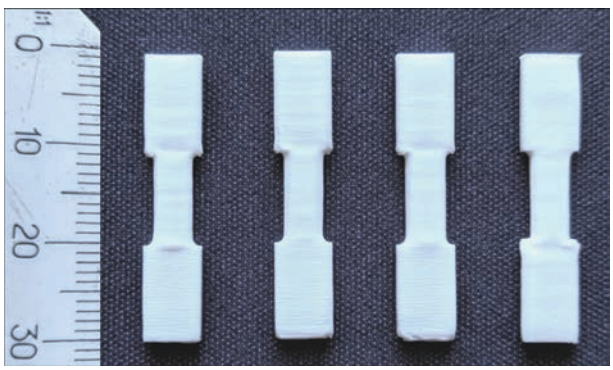

Figure 2. Appearance of the samples Nos 1–4 (from right to left)

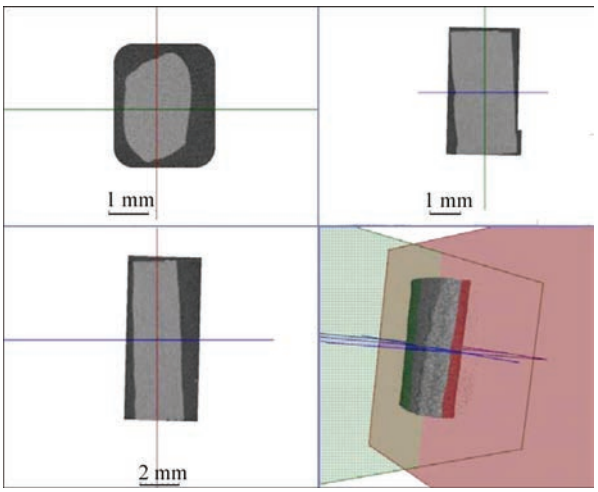

Figure 3. Image of inner structure of the sample No. 4 in different planes, obtained by 3D computer tomography

studies were conducted using the uniaxial tension test of the additively manufactured samples Nos 1–4. The obtained results as for adhesion strength between the layers are shown in Table 1.

The analysis of the results of mechanical studies showed that the best result σ = 56.9 MPa, which is close to the table value of the ultimate tensile strength of PLA σ = 57.8 MPa, was obtained in the case of forming 3D products at a speed of 80 mm/s. The worst result (σ = 39.3 MPa) was shown by the samples, whose formation occurred at the maximum speed of 110 mm/s. The samples, formed at speeds of the printing head movement of 20 and 50 mm/s, had average values of adhesion strength between the layers and close to each other (σ = 51.7 and 52.9 MPa, respectively).

Taking into account the fact that at all investigated speeds of the printing head movement during products creation, the samples of a preset geometric shape and visually with an equally high quality were formed, the choice of a mode that satisfies the needs of the consumer/customer depends on additional requirements specified to the future three-dimensional object, namely its mechanical characteristics and the time spent on the formation of each individual part. Objectively, the best printing mode, which allows fabricating products with high mechanical characteristics at relatively low time consumption — 16 min, is the mode of forming the sample No. 3 (Figure 4).

When the speed of the printing head movement during product formation is increased to 110 mm/s, the time for forming a product is slightly reduced (14 min), but at the same time, a negative effect of the speed on the mechanical strength of a produced object is observed.

When the printing head movement is slower (20 and 50 mm/s), the produced samples have average mechanical strength, but the time for forming products increases significantly — up to 22 and 20 min, respectively.

INFLUENCE OF THE METHOD OF ADDITIVE 3D PRODUCT FORMATION ON THE PECULIARITIES OF THEIR MANUFACTURING PROCESS, STRUCTURE AND PROPERTIES

In order to reduce the time spent on the process of creating products with the 3D printer, it is possible to simultaneously print several models within one cycle. The quantity of products that can be formed simultaneously depends on the characteristics of the 3D printer, namely the dimensions of its building area. For the further studies of the influence of simultaneous additive manufacturing of several samples on

Table 1. Strength of fabricated products depending on speed and time of their formation

Number of sample	Speed of movement of printing head during sample formation, mm/s	Time of one sample formation, min	Adhesion strength σ, MPa	Strength of PLA [14]
1	20	22	51.7	57.8
2	50	20	52.9	
3	80	16	56.9	
4	110	14	39.3	

the characteristics of fabricated products, the process mode of forming the sample No. 3 (Table 1) was chosen, with the use of which, the samples of the highest strength (σ = 56.9 MPa) were produced. As models for building, four similar samples with an identical shape (blades) were chosen, as in the previous research.

After forming the samples, a visual assessment of the fabricated products was carried out and it was established that their shape fully corresponds to the preset digital model, however, the structure of the formed parts is less dense compared to the sample No. 3, which was built separately (one sample per cycle) with the same parameters of forming products. The results of the study with the use of 3D computer tomography of the inner structure of the sample No. 5, whose formation was carried out under the conditions of simultaneous printing of four samples within one cycle, also confirmed a decrease in the density of the adherence of the deposited layers compared to the sample No. 3.

The conducted studies of adhesion strength between the layers of the produced samples using a standardized uniaxial tension test showed a significant decrease in strength (σ = 25 MPa) compared to single samples (σ = 59.6 MPa) formed in the same mode (Table 2).

This is explained by the fact that when forming four parts in parallel, when the extruder die passes

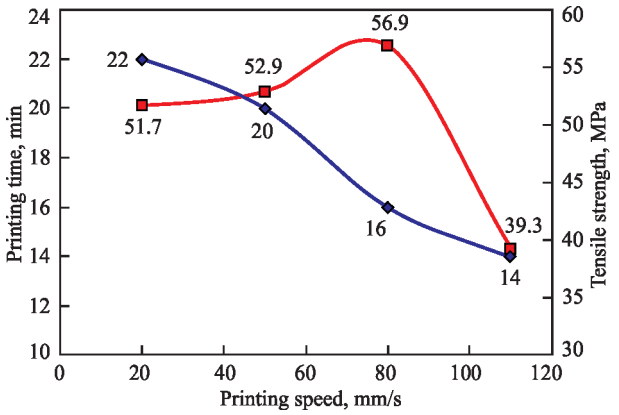

Figure 4. Dependence of time for sample formation and interlayer strength of formed 3D products on speed of their formation

Table 2. Strength of 3D products and time of their fabrication depending on the method of their formation

Time of 3D printing and mechanical properties of produced samples	Sample No. 3 (1 pc)	Sample No. 5 (4 pcs within one cycle)
Time of one sample formation, min	16	8
Interlayer strength σ, MPa	56.9	25
Strength of PLA filament, MPa [4]	51	
Strength of PLA, MPA [2]	57.8	

from one model to another, the temperature and ductility of the upper layers of a product decrease, which is predetermined by an increase in the cooling time, and the following layers of the fused material lie on the base, which had already time to partially solidify. This leads to a decrease in the adhesion and deterioration of the contact mechanical adhesion between the layers of a printed product and, as a result, a decrease in strength. On the other hand, it provides control of the mechanical properties of a product when it is formed by 3D printing and allows obtaining the specified strength in the desired areas of a part. For example, to create a predetermined local area with weakened mechanical properties in a product, along which the fracture of a part will occur when a force loading is applied to it, printing should be carried out in the appropriate mode — with pauses at the height of those layers, the adhesion between which should be predicted to be low. The program for reformatting a 3D model into a control code for 3D printer provides for changing the parameters of products formation according to the height of the model (for example, the speed of the printing head movement when forming products), including performing 3D printing with pauses. In the case of the mode of forming products of four samples within one cycle considered above, the pause between the deposition of the n^{th} and n+1 layers for each sample was the same, since the models on the platform were placed on the outer corners of the square, and was ~10 s for a wider area of the blade and ~8 s for its narrow part.

On the other hand, if the use of a product does not involve its operation under the conditions of significant loads, then the formation of simultaneously several parts by 3D printing allows a significant reduction in the time for the process of their manufacturing. Thus, under the conditions of the same 3D printing parameters, 16 min were spent to create one sample, the formation of which took place separately, and 8 min for a one sample, the formation of which was carried out simultaneously with three other within one cycle (see Table 2).

After uniaxial tension tests, the structure of the samples at the points of fracture was evaluated. Thus, on the microphotographs of the fracture plane of the sample No. 5 (Figure 5, *a*), the trajectory of the printing extruder head movement at the moment of depositing the previous layer material can be clearly traced — it starts from the lower right corner and further follows clockwise in a spiral to the center, which indicates that the fracture of a part occurred along the interlayer region. For comparison, the photomicrograph of the location of the fracture of the blade, the creation of which was carried out using the same printing parameters, only separately one by one, shows that its fracture occurred not between the layers, but in the plane of the layer (Figure 5, *b*), which indicates a higher adhesion between the layers in a formed 3D product.

INFLUENCE OF THE LAYER HEIGHT OF 3D PRODUCTS ON THE PECULIARITIES OF THEIR FORMATION, APPEARANCE, STRUCTURE AND PROPERTIES

Depending on the application of one or another FDM 3D printer and thermoplastic material, as well as the specified tasks (production of 3D parts with high accuracy and detailing, quick printing of end products of large sizes, etc.), it is possible to create volumetric products with surfaces of different quality. In this work, the selection of the parameters of the layer height of a 3D product, which directly affect the qual-

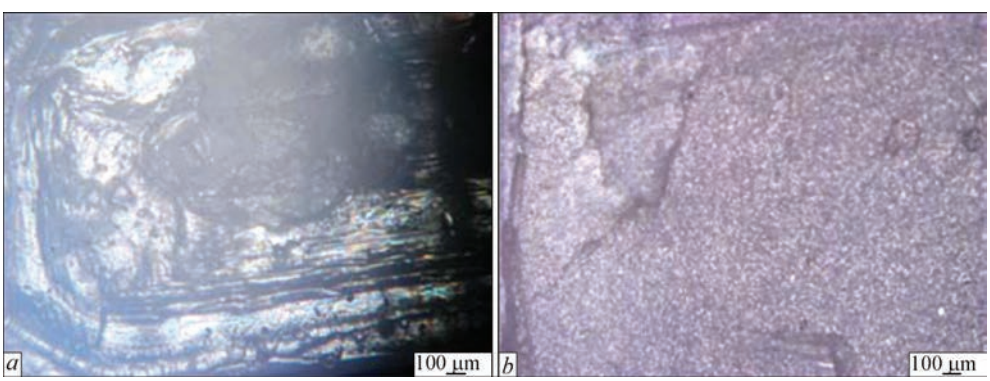

Figure 5. Morphology of the samples in places of fracture after the tests on uniaxial tension of the sample No. 5 (*a*) and the sample No. 3 (*b*)

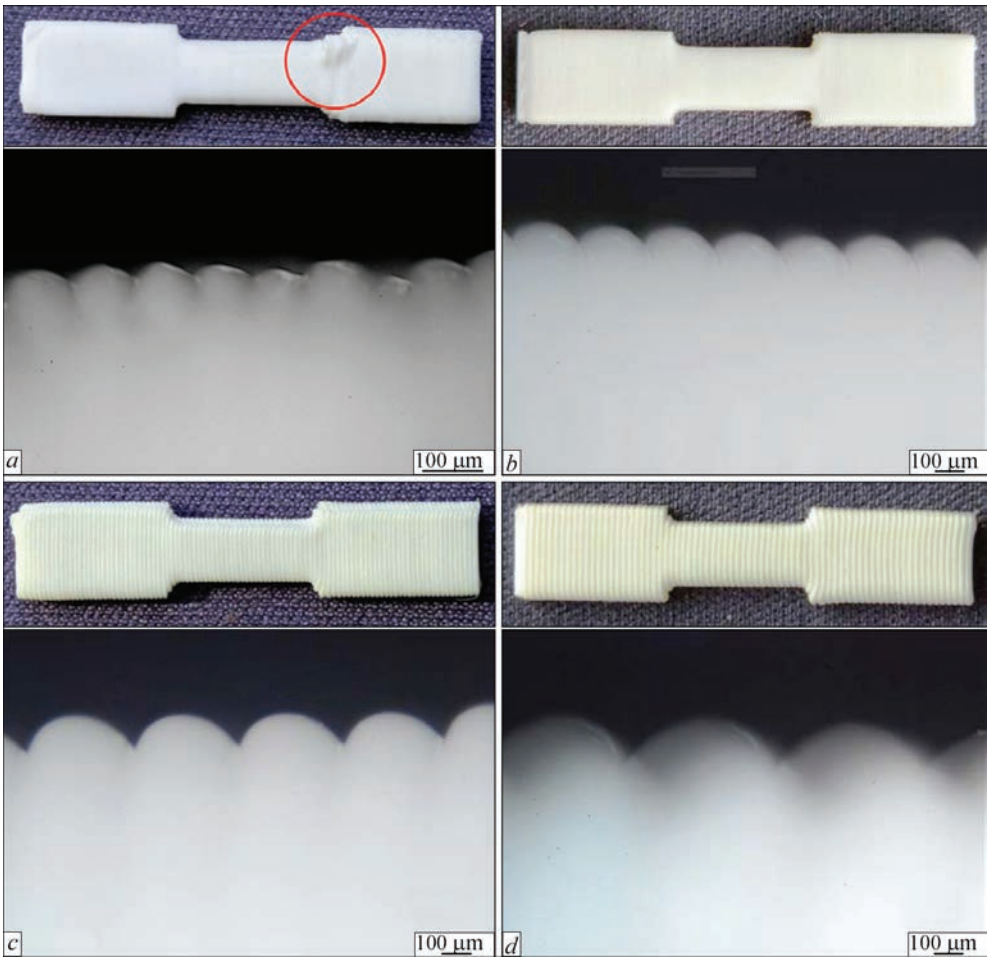

Figure 6. Photos and morphology of the samples of different quality: the sample No. 6 with the layer thickness of 0.08 mm (*a*); the sample No. 7 with the layer thickness of 0.20 mm (*b*); the sample No. 8 with the layer thickness 0.30 mm (*c*); the sample No. 9 with the layers thickness of 0.40 mm (*d*)

ity of produced samples, was based on the extreme admissible values (within the recommended limits) for the CreatorPro 3D printer and PLA filament. Without changing other printing parameters, except for the layer height, which was 0.08, 0.10, 0.20, 0.30 and 0.40 mm for the samples Nos 6–9, respectively, a study of the influence of the selected parameter on the appearance, structure and properties of fabricated products was carried out.

Figure 6 shows photos of the appearance and microstructure of the samples Nos 6 (*a*), 7 (*b*), 8 (*c*) and 9 (*d*), formed by the FDM 3D printing technology in accordance with the printing parameters. The fabricated blades generally have a preset geometric shape with sharp edges and clear outlines of a part. Since the products are formed in layers, it is obvious that the smaller the height of the layer, the less noticeable the transition between them and accordingly, the surface of an object is smoother, and its parts are more expressive. The samples, whose formation was carried out according to the specified thickness of each layer of 0.40 and 0.30 mm (Figure 6, *c*, *d*), have a lower resolution compared to the samples with a fixed height of each layer of 0.08 and 0.20 mm (Figure 6, *a*, *b*). The latter have much smaller visible layer lines and a smoother surface. However, at the minimum possible layer height, some inaccuracies — printing artifacts may be present (Figure 6, *a*). In this case, such inaccuracies may appear around the complex elements as, for example, in a printed sample, when its formation was carried out on the expansion of a part — transition from the narrowest part of a product to the wide one. With such a transition, additive overhang forming takes place, when each previous plane of a formed part is smaller in relation to the next one, which should be formed on its basis, and the more difficult it is to form a quality product in such conditions, the thinner the layers height of a future part. This error may be eliminated by building support structures (including soluble ones) under the overhanging elements of a part.

In this study, it was established that the time spent on the formation of one sample with a height of 0.08 mm layers of the printed products was 29 min. At the same time, printing of a sample identical in shape and sizes with the layer thickness of 0.40 mm made

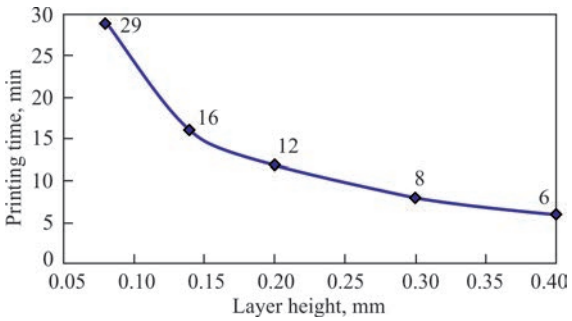

Figure 7. Dependence of time for 3D printing of samples on height of their layers

it possible to reduce the time spent on its creation to 6 min (Table 3).

In a situation where a logical inversely proportional dependence between the layer height — vertical resolution of a part and the time spent on printing the model is clearly visible (Figure 7), the dependence between the resolution and the strength of a part does not look so clear, since the conducted experiments showed that both at the minimum as well as at the maximum specified layer height for this material and the printer, the formed products had a visually high enough quality and density of layers.

It is obvious that the better the layers of a product adhere and wet each other during 3D forming, the higher the strength of a printed part will be. The problem is what layer height, if other settings being equal, will create conditions for forming layers with the highest adhesion between them.

Since the possibility of specifying the minimum and maximum possible value of the layer height for each specific filament in the software settings is limited by the diameter of the extruder die of the 3D printer, it is worth taking into account its influence on the conditions of product formation, structure and properties of fabricated products. Thus, during 3D forming of polylactide samples with a minimum admissible

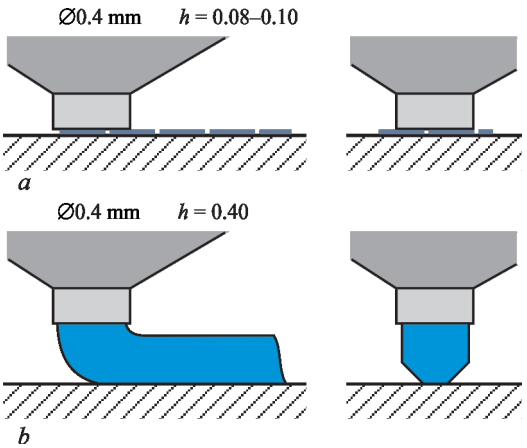

Figure 8. Schematic image of the process of depositing layers of fused polymer when forming 3D models with a different layer height with a diameter of 0.4 mm: h = 0.08–0.10 mm (*a*), h = = 0.40 mm (*b*)

Table 3. Time for printing fabricated products depending on layer thickness of 3D models

Number of sample	Layer height, mm	Time of one sample formation, min
6	0.08	29
7	0.20	12
8	0.30	8
9	0.40	6

layer height of 0.08–0.10 mm in the 3D printer with an extruder die of 0.4 mm diameter, the fused polymer squeezing through the die during product formation will be flatten, taking an oval shape of a preset height. This process is shown schematically in Figure 8, *a.* Adhesion of such layers will obviously be much higher than the layers with a height, for example, of 0.4 mm (Figure 8, *b*) due to the different area of contacting surfaces of the layers. Since the polymer melt at the moment of discharge from the extruder die with a diameter of 0.4 mm is flattened the less, the closer the specified layer height to 4 mm, and their shape at the same time is closer to cylindrical, then due to overlapping of layers of such a shape during forming a 3D product, a reduction in the contact surface between them occurs.

Therefore, the closer the value of the layer height of the future 3D object is set to the diameter of the extruder die in the software settings, the more rounded the shape of the layers will be in a formed product. This, in turn, leads to weakening of interlayer bonds.

To determine the dependence and more fully assess the effect on the mechanical strength of the layer height of formed 3D products with an extruder die diameter of 0.4 mm, mechanical tests on uniaxial tension of the samples Nos 6–9 were conducted. The analysis also used data from the sample No. 3, the formation of which was carried out under the identical conditions. The only difference was the investigated parameter — the layer height, which was 0.14 mm (Table 4).

It is seen that the highest values of the interlayer strength (σ = 56.9 MPa) were obtained in the printing mode No. 3 with a layer height of 0.14 mm. The same results were obtained for the samples Nos 7 and 9. I.e., with a preset minimum height of 0.08 mm, the val-

Table 4. Interlayer strength and time of product formation depending on thickness of their layers

Number of sample	Layer height, mm	Interlayer strength σ, MPa
7	0.08	47
8	0.30	42.5
9	0.20	47
10	0.40	39.6
3	0.14	56.9

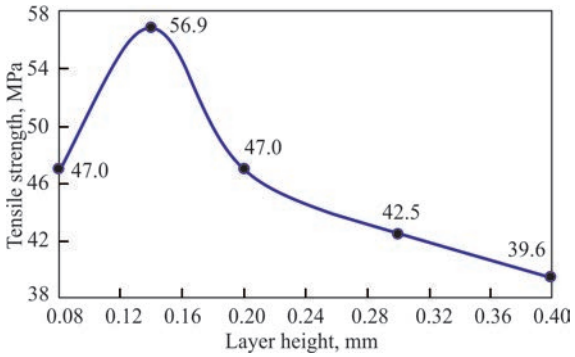

Figure 9. Dependence of interlayer strength of 3D products on height of their layers

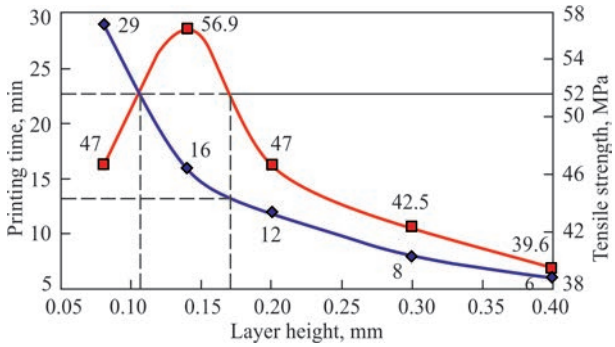

Figure 10. Dependence of time for 3D printing of products and interlayer strength of formed products on height of their layers

ue of the interlayer mechanical strength of products was at a level with products that had a layer height of 0.2 mm. However, in general, a tendency of a decrease in the interlayer strength of fabricated products with an increase in the value of height of their layers is observed. To visualize the obtained results, a diagram of the dependence of the interlayer strength on the layer height of 3D models was built (Figure 9).

In conclusion, it can be noted that such a parameter as the layer height has a significant impact on the strength of fabricated 3D products and the time spent on their formation, and therefore affects the economic indicator of the 3D printing process and resolution of the surface of a three-dimensional part.

If it is necessary to create a product with the minimum possible layering of the surface and the maximum possible detailing, its formation should be carried out according to the specified minimum height of layers, which is possible when forming a part with the 3D printer extruder die of the appropriate diameter. However, it is necessary to take into account the fact that this leads to a significant increase in the time for creating products. In addition, at the minimum thickness of the layers, there is a higher probability of obtaining artifacts on the surface of a product. In order to achieve an even greater minimization of the layered structure on the surface of 3D products, which is obtained during 3D printing using the FDM technology, it is necessary to use a die of a smaller diameter, perform the following surface treatment of finished 3D products, or use another 3D printing technology, for example, SLA, DLP, which allow creating models with higher resolution.

To systematize and summarize the obtained data according to the results of the carried out studies of the impact of the layer height on the time of products formation and their strength, a combining diagram was built (Figure 10). According to its analysis, the optimal height range of 3D products was determined, which should be kept to provide the additive formation of models with the interlayer strength at a level of 90 % of the strength of a consumable. Taking into account that the mechanical strength of polylactide according to the data of literary sources is $\sigma = 57.8$ MPa [14], then at the level of $\sigma = 52$ MPa, which is 90 % of the filament strength, along the axis of the "Tensile strength, MPa" diagram, a straight line was drawn. After that, perpendiculars were lowered from the points of its intersection with the distribution curve to the "Layer height, mm" axis. Therefore, it follows from the diagram that at the layer thickness of 0.108–0.173 mm, formation of 3D objects occurs with the interlayer strength at a level of 90 % of the strength of the source material and at the average time consumption for printing of one part (13.5–23 min).

CONCLUSIONS

1. A study of the influence of the FDM 3D printing process on the structure and properties of polymer filament material — polylactide was conducted. It is shown that the process of 3D printing (its basic parameters: extruder die temperature; height of layers deposited during formation of a product; speed of printing head movement during formation of a product and quantity of products formed in a one 3D printing cycle) significantly affects the appearance, structure, mechanical properties and the time spent on product formation.

2. A rational mode of additive formation of products was determined, which provides fabrication of parts of a preset geometric shape with the interlayer strength $\sigma = 56.9$ MPa close to the strength of the base material $\sigma = 57.8$ MPa and small time consumption (14 min) on the formation of a one part.

3. The mode of formation of 3D polylactide products was determined, which provides the ability to control the indices of mechanical properties of products during their additive manufacturing and obtain an early projected strength in the desired places of a part, for example, create local areas with weakened mechanical properties, along which the fracture will take place.

4. The modes of the process of volumetric product formation were determined that allow producing parts of a preset geometric shape within the shortest possible period of time (6 and 8 min). The time and, as a consequence, the costs on product formation are reduced at the expense of:

- simultaneous fabrication of several products within one cycle,
- formation of parts with the layer height as larger as possible for the studied material, 3D printer and recommended limits.

5. The modes of 3D printing process were determined, which allow creating products with the maximum possible detailing (along *Z* axis) due to software presetting of the minimum possible thickness of a product in 3D printing of the used thermoplastic material and 3D printer.

REFERENCES

1. Ngo, T.D, Kashani, A., Imbalzano, G. et al. (2018) Additive manufacturing (3D printing): a review of materials, methods, applications and challenges. *Composites Pt B: Engineering*, **143**, 172–196. DOI: https://doi.org/10.1016/j.compositesb.2018.02.012
2. *Jan Yang* Jiquan, Zheng Mei, Yang Jianfei et al. (2016) *Introduction to 3D printing technology [M]*. Nanjing, Nanjing Normal University Press.
3. Shahrubudin, N., Lee, T.C., Ramlan, R. (2019) An overview on 3D printing technology: technological, materials and applications. *Procedia Manuf.*, **35**, 1286–1296. DOI: https://doi.org/10.1016/j.promfg.2019.06.089
4. Kristiawan, R.B., Imaduddin, F., Ariawan, D., Ubaidillah, Zainal Arifin (2021) A review on the fused deposition modeling (FDM) 3D printing: Filament processing, materials, and printing parameters. *Open Engineering*, 11(**1**), 639–649. DOI: https://doi.org/10.1515/eng-2021-0063
5. Wilson, S., Thomas, R., Mary, N. et al. (2021) Development and fabrication of fused deposition modelling 3D printer. *IOP Conf. Series: Materials Sci. and Engineering*, **1132**, 012019. DOI: https://doi.org/10.1088/1757-899X/1132/1/012019
6. Masiuchok, O.P., Iurzhenko, M.V., Kolisnyk, R.V., Korab, M.G. (2020) Additive technologies of polymer materials (Review). *The Paton Welding J.*, **5**, 49–55. DOI: https://doi.org/10.37434/tpwj2020.05.08
7. Sikorska, W., Zięba, M., Musioł, M. et al. (2020) Forensic engineering of advanced polymeric materials — Pt VII: Degradation of biopolymer welded joints. *Polymers*, **12**, 1167. DOI: https://doi.org/10.3390/polym12051167
8. Marszałek-Harych, A., Jędrzkiewicz, D., Ejfler, J. (2017) Bio- and chemocatalysis cascades as a bridge between biology and chemistry for green polymer synthesis. *Cell. Mol. Biol. Lett.*, 22(**1**), 28. DOI: https://doi.org/10.1186/s11658-017-0061-1
9. Jalaber, M., Fraschini, C., Prud'Homme, R.E. et al (2007) Synthesis and characterization of poly(L-lactide)s and poly(D-lactide)s of controlled molecular weight. *J. of Polymer Sci. Pt A. Polymer Chemisry*, 45(**10**), 1944–1955. DOI: https://doi.org/10.1002/pola.21960
10. Lunt, J. (1998) Large-scale production, properties and commercial applications of polylactic acid polymers. *Polymer Degradation and Stability*, 59(**1–3**), 145–152. DOI: https://doi.org/10.1016/S0141-3910(97)00148-1
11. *Standard materials: PLA:* https://monofilament.com.ua/products/standartnye-materialy/pla/
12. Senchenkov, I.K., Iurzhenko, M.V., Chervinko, O.P. et al. (2021) Numerical modeling of stress-strain state of elements manufactured by 3D printing. *The Paton Welding J.*, **8**, 21–26. DOI: https://doi.org/10.37434/tpwj2021.08.05
13. Vega, V., Clements, J., Lam, T. et al. (2011) The effect of layer orientation on the mechanical properties and microstructure of a polymer. *J. Mater. Eng. Perform.*, 20(**6**), 978–988. DOI: https://doi.org/10.1007/s11665-010-9740-z
14. Dizon, J.R.C., Espera, A.H., Chen, Q., Advincula, R.C. (2018) Mechanical characterization of 3D printed polymers. *Add. Manuf.*, **20**, 44–67. DOI: https://doi.org/10.1016/j.addma.2017.12.002
15. Garlotta, D. (2001) A literature review of poly(lactic acid). *J. of Polym. and the Environ.*, 9(**2**), 63–84. DOI: https://doi.org/10.1023/A:1020200822435
16. *Table of standard settings for different types of materials for FDM 3D printers.* https://pro3d.com.ua/g75854193-plastik-kotushtsi

ORCID

O.P. Masiuchok: 0000-0002-3302-3079,
M.V. Iurzhenko: 0000-0002-5535-731X,
R.V. Kolisnyk: 0000-0002-0493-894X,
A.O. Shadrin: 0000-0002-2777-0852,
M.G. Korab: 0000-0001-8030-1468

CONFLICT OF INTEREST

The Authors declare no conflict of interest

CORRESPONDING AUTHOR

M.V. Iurzhenko
E.O. Paton Electric Welding Institute of the NASU
11 Kazymyr Malevych Str., 03150, Kyiv, Ukraine.
E-mail: 4chewip@gmail.com

SUGGESTED CITATION

O.P. Masiuchok, M.V. Iurzhenko, R.V. Kolisnyk, A.O. Shadrin, V.Yu. Kondratenko, M.G. Korab (2023) Study of the influence of FDM 3D printing parameters on formation processes, structure and properties of polylactide products. *The Paton Welding J.*, **12**, 31–38.

JOURNAL HOME PAGE

https://patonpublishinghouse.com/eng/journals/tpwj

Received: 23.10.2023
Accepted: 26.12.2023

DOI: https://doi.org/10.37434/tpwj2023.12.05

INVESTIGATIONS OF THE QUALITY OF METAL OF HIGH-MANGANESE STEEL ALLOYED BY ALUMINIUM AND CHROMIUM AFTER ELECTROSLAG REMELTING

V.A. Zaitsev, Yu.V. Kostetskyi, G.O. Polishko, V.A. Kostin, V.P. Petrenko, E.O. Pedchenko

E.O. Paton Electric Welding Institute of the NASU
11 Kazymyr Malevych Str., 03150, Kyiv, Ukraine

ABSTRACT

The paper presents the results of investigation of the influence of electroslag remelting on the properties of metal of ingots of high-manganese steel, alloyed by aluminium and chromium. Features of structure formation in high-alloy manganese steels are considered. These steels demonstrate ductility and lower density, alongside strength, and are difficult for pouring alloys, prone to hot cracking, formation of a coarse structure and development of macro- and microliquation. Studies have been performed, which confirm the conclusions that steels of this type require a thorough control of solidification conditions. Obtained results illustrate a significant influence of the cooling rate on cracking, manganese and aluminium segregation and parameters of the alloy dendritic structure. Electroslag remelting resulted in improvement of the structure and led to reduction of the size of nonmetallic inclusions in the studied metal without any significant changes in Mn, Al and Cr content, which is one of the conditions for producing large-sized homogeneous ingots. Metallographic examinations showed that the microstructure of all the studied steel specimens is characteristic for austenitic steel with dendritic crystal growth. Dendritic structure in the metal of ESR ingot is homogeneous, distances between the first and second order axes in the ingot middle and upper parts are equal to 136.6–146.5 and 60.54–8.92 μm, respectively. Completing formation of the required final microstructure of the studied steel takes place after further heat and thermodeformational treatment. ESR of cast billets allows reaching the required level of metal homogeneity and specified level of properties with a smaller number of stages and duration of thermomechanical treatment, and reducing resource consumption.

KEYWORDS: high-strength lightweight steel, ingot, electroslag remelting, microstructure, liquation, phase composition

INTRODUCTION

The development of modern industry involves not only the development and application of new structural materials, but also the creation of effective technologies for their production. Over the past few decades, many studies have been carried out, devoted to the investigation of the properties of Fe–Mn–Al–C steels [1–5] from the point of view of the possibility of their application in the power, chemical, mining and defence industries, infrastructure construction and transport engineering. For some period of time, Fe–Mn–Al–C steels were considered as a possible replacement for conventional chrome-nickel stainless steels [5]. In the 80s and 90s of the last century, the influence of their corrosion resistance, weldability, oxidation resistance, effect of temperature, chemical composition and microstructure on mechanical properties was actively investigated [4, 5]. One of the most important results of these studies was the awareness and understanding of the relationship between deformation mechanisms and mechanical properties, which attracted the attention of the academic community and ensured rapid progress in the further development and application of Fe–Mn–Al–C steels in the automotive industry. At present, research groups around the world are making efforts for further study of Fe–Mn–Al–C steels to make them more accessible and expand the range of possible applications.

Since the beginning of the 2000s, considerable attention has been paid to the study of Fe–Mn–Al–C steels with reduced density, that were intended for the application in various structures [3–5]. These steels may contain 3–30 % Mn, 3–12 % A1, 0.1–1.5 % C and are distinguished by a unique set of mechanical properties with a yield strength of 0.4–1.0 GPa, a tensile strength of 0.6–2.0 GPa and a relative elongation of 30–100 % [6–9]. Aluminium in the alloy composition provides reduction in the metal density. Each additional percent of aluminium results in a decrease in the metal density by approximately 1.3 %, as well as a decrease in the modulus of elasticity by 2 % and an increase in strength by 40 MPa [6, 10, 11]. Steels of this system with an aluminium content of more than 6 % were allocated to a new class of high-strength lightweight steels (low-density/lightweight steels).

Depending on the chemical composition, high-strength lightweight Fe–Mn–Al–C steels can have an austenitic, ferritic or double (duplex) matrix consisting of ferrite and austenite [4, 10]. Due to the presence of nanosized κ-carbides in the austenite matrix, these alloys show both excellent strength and ductility [4, 5]. Initially, it was assumed that κ-carbides worsen ductility, and to suppress their formation, it was proposed to add boron, titanium and niobium to the

Copyright © The Author(s)

composition of the alloy [9, 12]. However, later it was recognized, that in case of optimizing the morphology, size and distribution of κ-carbides, they may simultaneously improve both strength and ductility [9, 13]. Usually, coarse intercrystalline κ-carbides are undesirable, while intragranular nano-sized κ-carbides contribute to the improvement of mechanical properties [14]. The contribution of nanosized κ-carbides to improvement in the yield strength of steel 1.78 times exceeds the effect of strengthening with dissolved aluminium.

Over the past two decades, new grades of high-strength lightweight steels with an austenitic matrix have been developed, which combine high strength with excellent ductility [2, 6, 7] and are aimed at the needs of the automotive industry.

Austenitic high-strength lightweight steels usually contain 12–30 % of manganese, 0.6–2.0 % of carbon and 5–12 % of aluminium [5, 15, 16]. Their phase structure consists mainly of an austenitic matrix with traces of ferrite, κ-carbides and β-Mn phase. At hot deformation temperatures, these steels have practically one austenitic phase. In the cast state, they show a dendritic microstructure and a tendency to liquation due to a significant content of alloying elements. Slow cooling of these steels leads to the formation of sources of the ferritic phase and coarse κ-carbides mainly along the boundaries of austenitic grains [9, 14]. To reduce micro-inhomogeneities, homogenization is performed with exposure at a temperature of 1100–1250 °C for the required time. The recrystallized microstructure usually contains equiaxial austenitic grains with annealing twins [5]. To avoid precipitation of coarse κ-carbides, these steels are quenched in water at a temperature of 900–1100 °C. During the aging of austenitic Fe–Mn–Al–C steels in the temperature range of 500–900 °C, two types of κ-carbides can also form — intergranular and intragranular [8]. As was mentioned above, the morphology of these carbides significantly affects the properties of steel. In general, these steels show a good combination of strength (600–1700 MPa) and ductility (up to 85 %) [3, 17].

High-strength lightweight austenitic duplex steels may contain 18–28 % Mn, 9–12 % A1 and 0.7–1.2 % C [5]. At temperatures of hot deformation, such steel consists mainly of austenite and a smaller amount of ferritic phase. Due to the significant content of manganese and aluminium, the austenitic phase is quite stable. At room temperature, these steels usually have a stable austenitic phase as a matrix one with precipitations of nanosized κ-carbides dispersed in it (less than 10 vol.%), as well as a small amount of ferritic phase (5–15 vol.%). Steels of this type are a variety of multiphase steels and are known as Triplex steels [6]. They have much better tensile properties than low-density ferritic steels [17].

As research has shown, the cold working of Fe–Mn–Al–C alloys deteriorates significantly with an increase in the aluminium content by more than 10 wt.% due to the propagation of brittleness [9]. Accordingly, the majority of studies of lightweight Fe–Mn–Al–C steels are limited to the compositions with the content of aluminium from 5 to 10 wt.% [6, 18–23]. By the way, it turned out that the addition of Cr can significantly improve the cold working even at a high content of aluminium and carbon [19]. Thus, for example, with the addition of chromium, Fe–20–Mn–13Al–1.3C–5Cr steel was produced with a density of 6430 $kg \cdot m^{-3}$ (a decrease in density is 18.3 %), a yield strength of 915 MPa, a tensile strength of 1140 MPa, and a total elongation of 22 % during uniaxial tensile tests performed at room temperature with a strain rate of $3.3 \cdot 10^{-4} \cdot s^{-1}$. Without the addition of chromium, Fe–20Mn–12Al–l.5C steel has a typical complex microstructure, which mainly consists of austenite with fine dispersed intragranular κ-carbides in it, a small fraction of ferrite and coarse intergranular κ-carbides. It is assumed that Cr, which is a carbide-forming element, suppresses the formation of intergranular κ-carbides and increases the amount of carbon in the austenitic phase.

Thus, acquiring the necessary set of properties by high-strength lightweight Fe–Mn–Al–C steels is determined by the complex relationship between the chemical composition and the micro- and macrostructures formed in the process of solidification of the alloy and during the subsequent heat and thermomechanical treatment. The production of these steels will require compliance with a high culture of production with precise technological control and the introduction of new technologies. As a result, despite the favourable market prospects, the deployment of large-scale commercial production of high-strength lightweight Fe–Mn–Al–C steels is hindered by a number of technical and technological problems that occur at almost all stages of the production process, which makes it quite expensive so far.

High-alloy Fe–Mn–Al–C steels, like other high-manganese steels, are complex alloys for pouring, prone to hot cracking, formation of a rough structure and development of macro- and microliquation [20–24]. A high content of alloying elements significantly affects the nature of the crystallization process, contributes to the development of liquation processes and heterogeneity of the resulting structures. For example, a study of an ingot of medium-manganese steel Fe–5Mn–1.5Al showed that the content of manganese in the central volumes of the ingot is greater than in

the surface volumes, while aluminium shows the opposite tendency to macrosegregation [25]. Studies of the homogeneity of the distribution of impurities at the microlevel in the austenitic steel with a high manganese content showed that, depending on the conditions of crystallization due to the development of liquation, the difference in the content of manganese in different structures can reach 2–7 wt.%, and carbon — 0.06–0.3 wt.% [26]. Against the background of strong liquation, in steels with a complex structure, phases may even form that are not predicted by the equilibrium phase diagram [24]. The liquidation of alloy components and related structural inhomogeneities affect the distribution of mechanical properties, corrosion resistance, efficiency and results of heat and mechanical treatments.

As is shown by special studies, the cooling and the associated solidification rates significantly affect the parameters of the primary structure of the metal at the macro- and microlevels, as well as the degree of segregation of the alloy components, which is predetermined by their different solubility in the formed structures [27, 28]. An increase in the solidification rate helps to obtain a more uniform structure [22, 23], but it is practically impossible to ensure the required cooling rate simultaneously over the entire cross-section of the ingot. In this regard, new and improved continuous pouring technologies were developed and implemented for the production of Fe–Mn–Al–C steel sheets [29, 30]. However, such a solution is not universal, as certain products require pouring of steel into ingots. In this case, before further thermomechanical treatment, it is advisable to subject the produced ingots to the process of electroslag remelting (ESR), which improves the crystalline structure and chemical homogeneity of the cast metal [29, 31]. ESR is widely used in the production of special steels and superalloys to produce ingots that are more pure in terms of nonmetallic inclusions, with minimized macrosegregation and a more uniform microstructure, which allows achieving the required final level of metal homogeneity and a defined level of properties with fewer stages of thermomechanical treatment, reducing time and energy.

This work presents the results of the study of the structure and properties of high-strength lightweight steel (25–28 % Mn, ≤ 3 % Si, 9–11 % Al, 5–6 % Cr, 1.8 % C) in the cast state after pouring into ingots and after the next electroslag remelting in order to determine the effect of remelting on the metal quality.

RESEARCH PROCEDURE

Melting of the experimental metal was carried out in an induction crucible melting furnace with a subsequent pouring into ingots, which were furtheron used as consumable electrodes during electroslag remelting. For melting of experimental steel, the crucible lining of the induction furnace with a setting of 60 kg was made of a mixture of alumina and magnesite, taken in a ratio of 75/25. Casting moulds to produce castings with a diameter of 0.08 m and a length of up to 0.7 m were made from a sand moulding mixture. To reduce the oxidizing effect of the atmosphere during melting, a layer of protective flux was created on the surface of the liquid metal in the crucible of the induction furnace.

Electroslag remelting of the experimental metal was carried out in an ESR furnace of P-951 type with a current-conducting mould with an inner diameter of 0.18 m and a two-circuit power supply. In order to reduce the loss of alloying components with the oxidation during remelting, over the slag surface in the mould, the partial pressure of oxygen was reduced by blowing argon into the space above the slag through a circumferential distributor pipe. Remelting was carried out with the use of ANF-29 flux. During remelting, a stable electrical mode and a minimal immersion of the electrode were maintained. At the same time, the electric power was equally distributed between the electrode and the current-conducting section of the mould. The filling factor of the mould during remelting was 0.2.

Specimens for chemical analysis and metallographic examinations were cut out from the produced castings and ESR ingot. The content of leading alloying elements in the casting and ingot metal after electroslag remelting is presented in Table 1.

The study of the microstructure of the investigated steel in the cast state and after electroslag remelting was carried out in the Neophot-32 optical microscope, equipped with a digital photography attachment. Images were registered using the QuickPhoto computer program. Digital images were processed using the Atlas program at magnifications of 25–500 times in a light field. The study of the results of the process of

Table 1. Content of leading alloying elements in the investigated metal, wt.%

Specimen		Al	Si	Cr	Mn
Cast metal		9.96	0.38	6.10	28.45
ESR ingot	Middle of the height	10.79	2.66	5.77	25.70
	Main part	10.67	1.12	6.27	28.10

crystallization and dispersion of the dendritic structure of the cast metal was carried out by the method of measurement of the distance between the dendrite branches of the first and second order using the Tescan computer program.

The study of the local chemical composition, distribution and composition of phases, distribution of chemical elements, chemical heterogeneity over the section area, morphology and chemical composition of nonmetallic inclusions (NI), as well as obtaining images of the object over a wide range of magnifications in secondary and scattered electrons were carried out using the analytical complex, which is composed of JSM-35CF electron microscope of JEOL Company (Japan) and INCA Energy-350 X-ray spectrometer with dispersion on the energy of X-ray quanta of Oxford Instruments Company (UK). In the work, SEI mode (secondary electrons image) was used to study the morphology and chemical composition of nonmetallic inclusions, as well as building of concentration maps for element distribution. The experiments were performed at an accelerating voltage of 20 kV and at a magnification from 200 to 10000. The elemental analysis was performed in the range from B to U.

According to morphological features and chemical composition, based on the energy dispersion spectral analysis, the inclusions were distributed into types (elemental composition) and their sizes were determined. The results of NI analysis were processed using a special program for quantitative distribution of phases and inclusions (INCA Feature). All results are presented in weight percentages.

Durometric studies were conducted in the durometer Leco-M400. The measurements of Vickers integral hardness were carried out at a load of 50 g.

RESULTS OF METALLOGRAPHIC EXAMINATIONS OF METAL IN THE CAST STATE

Metallographic examinations of specimens of the studied metal in the cast state were carried out in the cross-section in the areas in the central part of the ingot and near the surface.

The study of the structure and distribution of nonmetallic inclusions was carried out on the sections without etching. Analysis of the obtained results showed that it is possible to clearly separate the phase components in the metal structure: of dark (spectrum 1) and two types of light (spectra 2, 4) colours (Figure 1). The matrix has a light colour and has in its chemical composition: 14 wt.% Al, 0.6 wt.% Si, 5 wt.% Cr, 25 wt.% Mn. In the dark component, an increased content of Mn to 34 wt.% and Cr to 8.12 wt.% is observed.

Analysis of the distribution of dispersed NI showed that they are uniformly located in the matrix, have a predominantly regular globular shape, and their size does not exceed 3 μm in the matrix (Figure 2, spectra 1, 2). It is established that the chemical composition of the inclusion is aluminium oxynitride ($Al_2(O, N)_3$) with a slight content of magnesium impurity (up to 1 %).

The metal structure after etching has a similar appearance with the structure, which is observed on non-etched specimens. After etching of the experimental specimens, eutectic precipitations are clearly revealed on them. The structure of the experimental metal is two-phase: austenitic matrix (gray) and eutectic on the boundaries of grains (Figure 3). The eutectoid consists of two phases, in which one of the phases is close as to its composition to the matrix, and the other — has a higher iron content and less alloying elements. According to literary

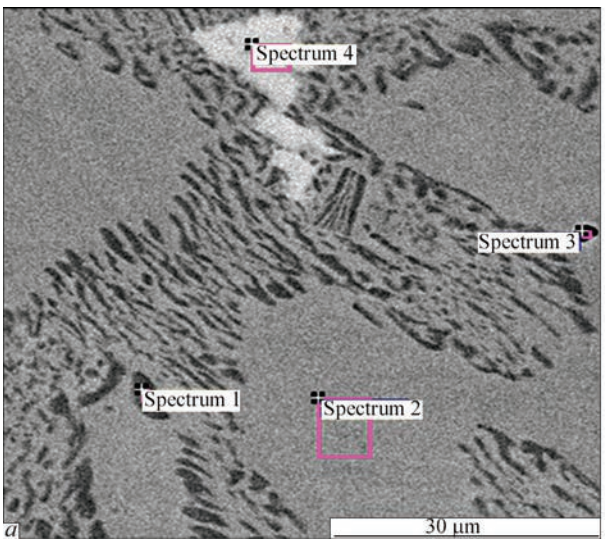

a

Analysis spectrum	Element content, wt.%				
	Al	Si	Cr	Mn	Fe
1	12.61	–	8.06	33.43	45.91
2	13.62	0.56	4.76	24.13	56.93
3	29.63	0.24	2.88	14.09	31.88
4	11.51	0.97	6.92	30.81	49.78

Note. Spectrum 3 — 18.47 % N, 1.98 % O, 0.55 % Mg, 0.28 % S.

b

Figure 1. Structure of metal of investigated steel (*a*) in the cast state without etching (BEI mode) and results of local chemical analysis of specimens (*b*)

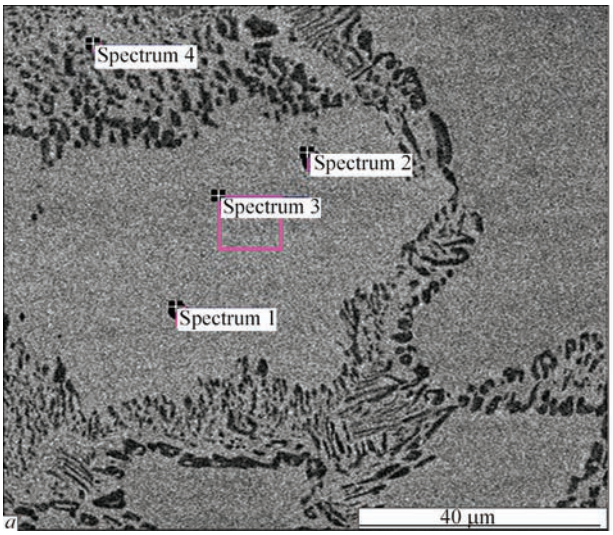

Analysis spectrum	Element content, wt.%				
	N	O	Al	Cr	Mn
1	23.36	3.87	46.4	1.61	7.21
2	27.72	4.49	48.1	1.20	5.26
3	–	–	13.6	4.68	24.08
4	–	–	13.6	8.12	32.05

Note. Spectrum 1 — 0.9 % Mg, Spectrum 2 — 0.98 % Mg. Remnant — iron.

b

Figure 2. Structure of metal of investigated steel (*a*) in the cast state without etching (BEI mode) and results of local chemical analysis of NI (*b*)

sources [1, 10, 17, 19, 21], a two-phase structure can be identified as an ordered ferritic structure and κ-carbide, which is formed at a slow cooling in Fe–Mn–Al–C steels. At elevated carbon concentrations such as in Triplex steels (1.2 % C), an eutectoid reaction of austenite conversion to laminar ferrite and κ-carbide (κ-carbide is FCC carbide of (Fe, $Mn)_3A1C$) type occurs.

In order to determine how uniform alloying elements were distributed in the metal of the studied steel in the cast state after melting in the induction furnace, a linear scanning was carried out according to the selected element on the surface of the specimen. According to the linear distribution of the basic alloying elements on the surface of the specimen in the area of the formed eutectic, a decrease in iron content, an increase in the content of manganese and chromium and some reduction in aluminium content (Figure 4) were established.

As is known [22, 23, 27], the basic parameters of crystallization, which determine the dispersion of the structure, is the crystallization rate and the temperature gradient of the crystallization front. The greater the dispersion of the structure, which may be indicated by the distance between the primary or secondary branches of dendrites, the more homogeneous metal and the better its properties in the cast state and the less banding in the deformed metal. The distance between the primary and secondary branches of dendrites is a direct indicator of the dispersion of the primary structure.

The results of the study of the dendritic (primary) structure are shown in Figure 5. In the interdendritic space, a darker complex component was formed, which is revealed as a two-phase structure of acicular type at a magnification. Dendrites are oriented in different directions relative to the axis of the ingot and have the axes of the first and second order. They

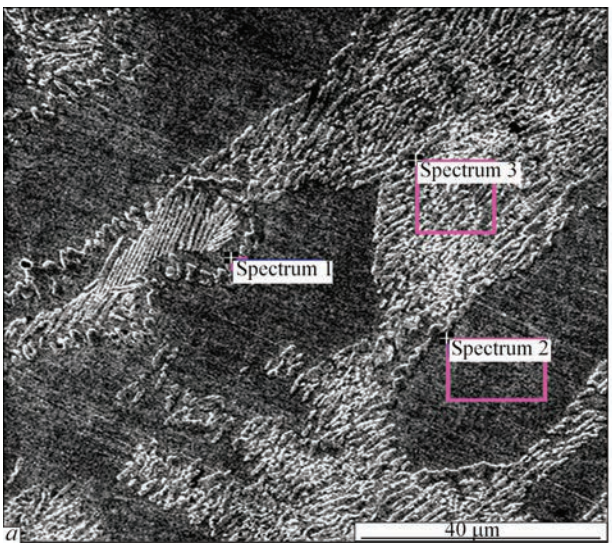

Analysis spectrum	Element content, wt.%				
	Al	Si	Cr	Mn	Fe
1	12.98	0.37	7.12	29.74	49.78
2	13.75	0.61	4.64	24.15	56.85
3	12.51	0.58	6.72	28.21	51.98

b

Figure 3. Structure of metal of investigated steel (*a*) in the cast state after etching (BEI mode) and results of local chemical analysis of specimens (*b*)

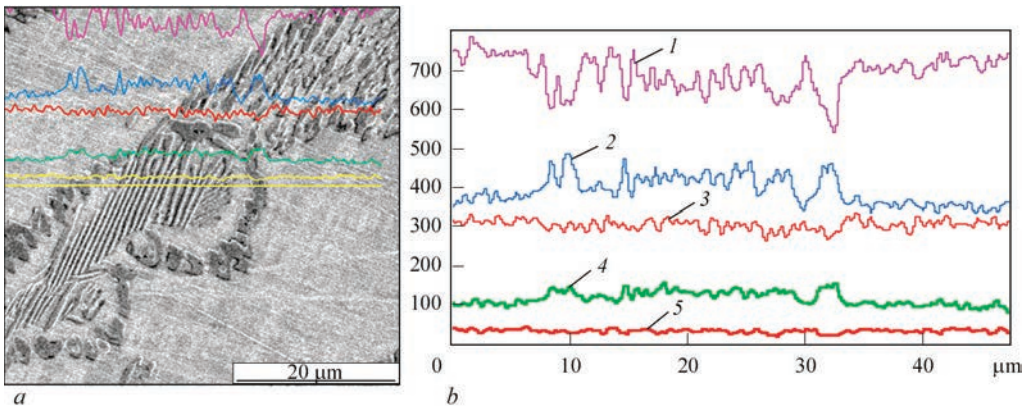

Figure 4. Microstructure (*a*) and linear distribution (*b*) of basic elements over the cross-section of metal specimen in the cast state: *1* — Fe; *2* — Mn; *3*—Al; *4* — Cr; *5* — Si

have an elongated shape with a length to width ratio of 5:1. The distance between the axes of the first order is 281.5–306.5 μm and 44.41–45.19 μm between the axes of the second order.

In the specimen from the area close to the surface of the ingot, the formation of branched cracks along the boundaries of the dendrites is observed, which mainly penetrate into the interdendritic space (Figure 6, *a*). Their formation can be a consequence of the liquation of alloying elements and, first of all, aluminium and manganese, which form brittle eutectics, that can be removed by remelting and appropriate heat treatment. In addition, in the specimen metal, that was taken close to the surface of the ingot, during the measurement of microhardness, cracks were formed already at a load of 50 kg/mm^2, which indicates an increased brittleness of the metal (Figure 6, *b*). The cracks propagated mainly along the boundaries of the dendrites.

According to the results of durometric tests, it was established that in the metal of the ingot produced by casting into a casting mould after induction melting, the dark and light phases have an increased level of microhardness (4219 ± 370 and 4405 ± 375 MPa, respectively) compared to the matrix (3220 ± 300 MPa) and two-phase areas (3219 ± 360 MPa).

RESULTS OF METALLOGRAPHIC EXAMINATIONS OF METAL AFTER ESR

Electroslag remelting, during which there is no large volume of liquid metal that solidifies simultaneously, contributes to a more uniform distribution of alloying elements at the macrolevel during crystallization of large

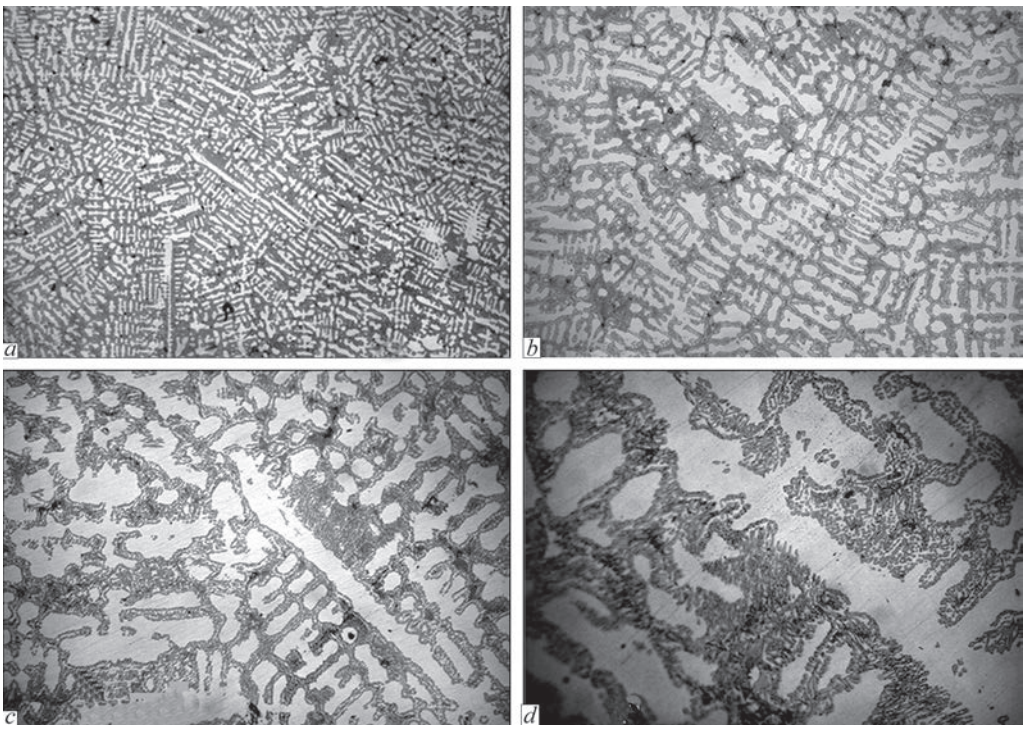

Figure 5. Dendritic microstructure at different magnification of characteristic areas of cast metal specimen from ingot with a diameter of 0.08 m (central part): *a* — ×50; *b* — ×100; *c* — ×200; *d* — ×400

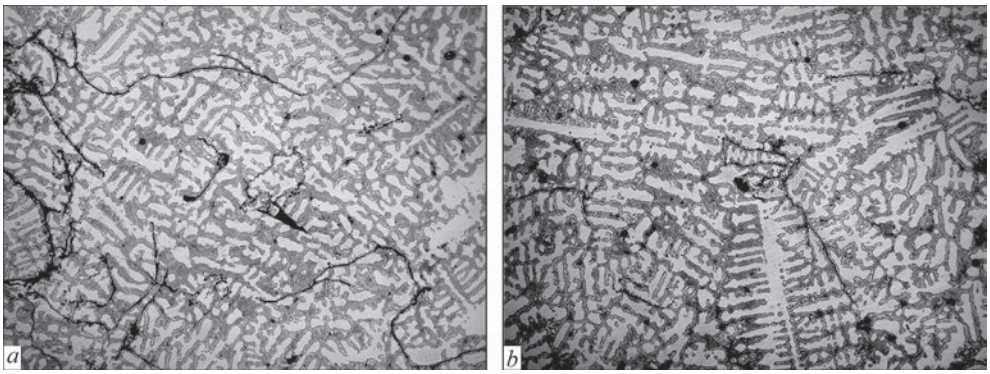

Figure 6. Distribution of microcracks on the areas close to the ingot surface of the cast metal (*a*) and after measurement of microhardness (*b*), ×100

ingots, and the faster growth of a dense dendritic structure suppresses the propagation of microliquations.

The study of the microstructure of the ingot metal by ESR on the specimens without etching showed that, as in the metal of cast ingots, a clear separation of the phase components in the metal structure is observed: of dark (spectrum 3) and two types of light (spectra 1, 2, 5) colour, which differ by the content of Al, Mn, Cr and Si (Figure 7).

The matrix has a light colour and contains up to: 13 wt.% Al, 1.27 wt.% Si, 5 wt.% Cr and 24 wt.% Mn. In the dark component, an increased content of such elements is observed: Mn up to 30 wt.%, Cr up to 10 wt.% (Figure 7), which is typical for the carbide phase of chromium-alloyed κ-carbide $(Fe, Mn)_3A1C$ type.

The studies have shown a uniform distribution of dispersed NI of up to 2 μm in size with a regular globular shape (Figure 7, spectra 4, 6, 7). According to their chemical composition, they represent aluminium oxynitride with magnesium impurities of up to 5.39 % (Figure 7, spectrum 7). Characteristic NI represent aluminosilicates (spectra 4, 6). The last inclusion (spectrum 7) has an extremely high content of magnesium — almost 10 %, which indicates a slag component of the inclusion.

The study of the heterogeneity of distributing alloying elements in the axes of dendrites and interdendritic space showed that the content of aluminium in the axes of dendrites is 12.05–12.85 wt.%, silicon — 1.04–1.11 wt.%, chromium — 4.88–5.06 wt.%, manganese — 23.93–24.53 wt.%, the aluminium content in the interdendritic space decreases to 10.53–10.63 wt.% and silicon to 0.85–0.92 wt.%, the content of chromium grows to 7.02–7.2 wt.% and manganese to 28.23–28.60 wt.%.

The linear distribution of the basic alloying elements on the surface of the specimen (Figure 8) along the dendrite axis and in the interaxial space confirmed the results of the local analysis. In the axes of dendrites, the content of aluminium and silicon grows and the content of chromium and manganese decreases compared to the interdendritic space.

In order to determine the features of the dendritic structure after etching of ESR metal specimens from the upper and middle parts of the ingot with a diameter of 180 mm, the primary structure of the cast metal was revealed, which consists of light-coloured

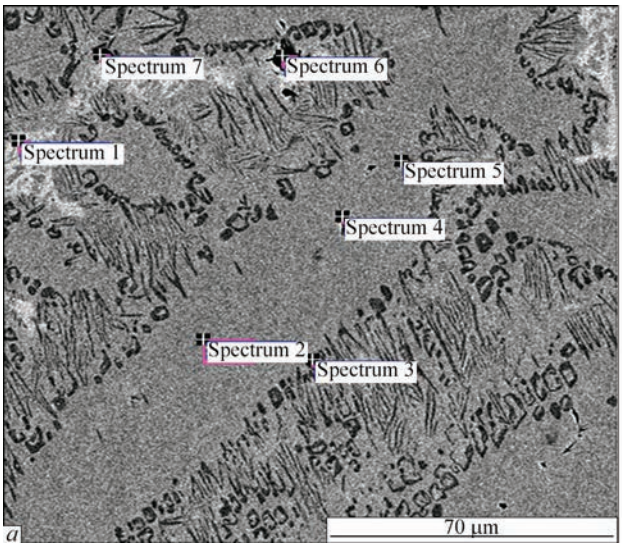

a

Analysis spectrum	Element content, wt.%				
	Al	Si	Cr	Mn	Fe
1	11.40	0.95	6.50	28.17	52.98
2	12.72	1.27	4.75	23.91	57.34
3	12.90	–	9.29	35.31	42.50
4	9.82	5.10	4.25	21.84	50.95
5	13.30	1.49	4.79	23.43	56.99
6	3.43	2.51	9.98	14.38	55.47
7	3.94	1.12	8.74	29.57	41.39

Note. Spectrum 4 — 8.04 % O, Spectrum 6 — 8.76 % O, Spectrum 7 — 9.85 % O, 5.39 % Mg.

b

Figure 7. Structure of investigated metal (*a*) after ESR (BEI mode) and results of local chemical analysis of specimens without etching (*б*)

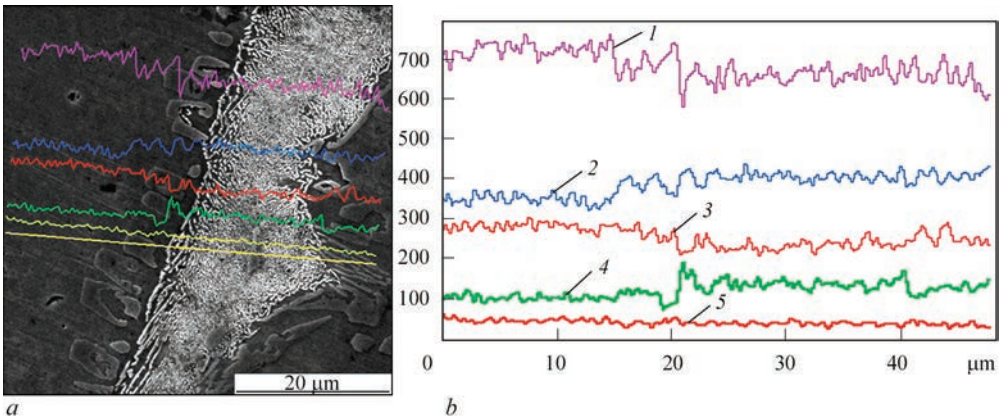

Figure 8. Microstructure (*a*) and linear distribution (*b*) of basic elements over the cross-section of ESR metal specimen: *1* — Fe; *2* — Mn; *3* —Al; *4* — Cr; *5* — Si (dendrite axes — dark; interdendritic space — light)

dendrites, indicating the presence of the austenitic structure, and a dark phase of the interdendritic space (Figure 9). In general, the microstructure is characterized by a homogeneous dense structure. Cracks, slag inclusions and delaminations at the boundaries of dendritic grains, unlike cast metal, are not observed. Dendrites are located in different directions relative to the axis of the ingot and have axes of the first and second order. Dendrites are smaller unlike the initial metal of the electrode (in the cast metal), have an elongated shape with a length to width ratio of 3:1. The dispersion of the dendritic structure in the ESR ingot metal was also evaluated in height. Sufficiently uniform values of the distance between the axes of the first and second order in the middle and upper parts of the ingot were established, which are respectively 136.6–146.5 and 60.54–68.92 μm.

Comparison of the metal microstructure in the specimens from the upper and middle parts of the ESR ingot showed that in the middle of the ingot in the area close to its surface, a number of dispersed nonmetallic inclusions is greater. The predominant size of the inclusions is less than 3 μm, however, single inclusions of up to 5 μm in size are observed. In terms of chemical composition, similar to the initial metal, complex inclusions of aluminium oxynitride and aluminium oxide with calcium (aluminocalcium silicates) are encountered, which can be formed as a result of interaction with slag during ESR.

It was also established that along the boundaries of dendrites axes, there are precipitations of separate

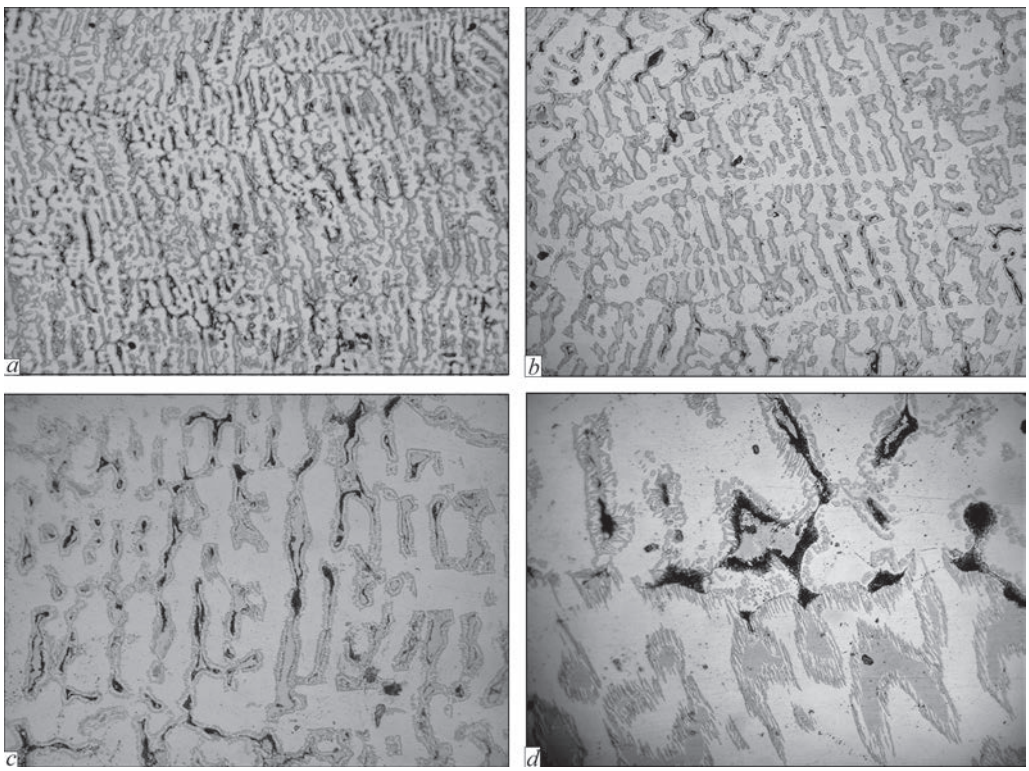

Figure 9. Dendritic microstructure at different magnification of characteristic areas of metal specimen from ESR ingot with a diameter of 0.18 m after etching (upper part): *a* — ×50; *b* — ×100; *c* — ×200; *d* — ×400

areas of light-coloured eutectic, which differs in the chemical composition and level of microhardness and has a reduced melting temperature, which can lead to its premature melting and a decrease in the metal properties under appropriate operating conditions. To eliminate the risk of melting, it is necessary to carry out appropriate heat treatment in order to form a more uniform distribution of alloying elements (Al, Mn, Cr) in the metal matrix. The presence of a eutectic can lead to the formation of primary cracks, as evidenced by dark regions in the middle of the eutectic.

In the upper part of the ESR ingot, as in the initial metal, in terms of the level of microhardness, the dark component and the light phase have an increased level of microhardness — 4427 ± 215 and 4386 ± 560 MPa, respectively, relative to the matrix and eutectic — 3119 ± 400 and 3208 ± 208 MPa, respectively. However, in the middle (in height) of the ingot, an increase in the level of microhardness of the dark component to 6226 ± 140, and of the light component to 4205 ± 420 MPa is observed, which may be a consequence of an uneven distribution of phases.

Evaluation of the dispersion of the dendritic structure in the metal of the ESR ingot over its height showed a sufficiently uniform distribution of the distance between the axes of the first and second order in the middle and upper parts of the ingot, which make up 136.6–146.5 and 60.54–68.92 μm, respectively.

In general, the distribution of alloying elements Al, Mn, Cr and Si, which is observed in the studied metal, is characteristic (according to literary data) for structural components of steels of this type. Obviously, in order to ensure their more uniform distribution and formation of the structure characteristic for high-strength steels, additional thermodeformational and heat treatment should be carried out, which is provided by the standard cycle of their manufacture. The excessive growth of silicon concentration in metal during ESR can be prevented by carrying out the process under the silicon-free fluxes [32].

In general, metallographic examinations showed that the microstructure of all experimental specimens is austenitic with the dendritic shape of crystals. Cracks, slag inclusions and delaminations on the boundaries of grains in the ESR ingot metal were not detected.

The carried out studies show that for steels with a high content of manganese, aluminium and carbon, the controlled conditions of solidification should be provided, at which the cooling rate, on the one hand, should be sufficiently high to form a uniform structure and, on the other, not cause cracks in thermally stressed zones.

The carried out studies have shown that electroslag remelting of cast billets of Fe–Mn–Al–C steel provides improvement of the structure and reduction of the size of nonmetallic inclusions without significant changes in the content of leading alloying components, which makes it possible to produce large-sized homogeneous ingots.

CONCLUSIONS

1. High-strength lightweight Fe–Mn–Al–C steels are high-tech alloys, which simultaneously show excellent ductility along with high strength, as well as reduced density depending on the aluminium content. Acquiring the required level of properties by them is determined by the complex dependence between the chemical composition and the macro- and microstructures formed during the process of solidification of the alloy and during the subsequent heat and thermomechanical treatment.

2. High-alloy Fe–Mn–Al–C steels like other steels with a high content of manganese, are complex alloys for pouring, prone to hot cracking, formation of coarse structure and development of macro- and microliquation. Structural heterogeneities resulting from the segregation of impurities affect the distribution of mechanical properties, corrosion resistance, efficiency and results of heat and mechanical treatments.

3. The performed studies confirm the conclusions that for steels of this type it is necessary to thoroughly control the conditions of solidification so that, on the one hand, to minimize the segregation of impurities, and on the other, to prevent the formation of cracks in the areas of thermal stress. The obtained results illustrate the significant impact of cooling rate on crack formation, distribution of manganese and aluminium at macro- and microlevels and parameters of dendritic structure of the alloy.

4. Electroslag remelting of cast billets provided improvement of the structure and led to a decrease in the size of NI in the studied metal without significant changes in the content of leading alloying elements, which is a prerequisite for producing large-sized homogeneous ingots. Distribution of Mn, Al, Cr and Si at the microlevel according to the values of micro X-ray spectral analysis is characteristic of high-alloy Fe–Mn–Al–C steels according to literary data.

5. Metallographic examinations showed that the microstructure in all specimens of the studied steel is characteristic of cast austenitic steel with a dendritic growth of crystals. The dendritic structure in the ESR ingot is uniform, the distances between the axes of the first and second order in the middle and upper part of the ingot are 136.6–146.5 and 60.54–68.92 μm, respectively. To complete the formation of the required microstructure, it is necessary to carry out appropriate thermodeformational and heat treatment.

6. Prior to further thermomechanical treatment, it is advisable to expose the ingots of high-alloy Fe-Mn–Al–C steels to the ESR process, which provides the improvement of crystalline structure and chemical uniformity of the cast metal, which allows reaching the required level of metal homogeneity, a certain level of properties with a smaller quantity of stages, duration of thermomechanical treatment and reduction in the consumption of resources.

REFERENCES

1. Hansoo Kim, Dong-Woo Suh, Nack J. Kim. (2013) Fe–Al–Mn–C lightweight structural alloys: A review on the microstructures and mechanical properties. *Sci. and Technol. of Advanced Materials*, 14(**1**), 11. DOI: https://doi.org/10.1088/1468-6996/14/1/014205
2. Frommeyer, G., Drewes, E.J., Engl, B. (2000) Physical and mechanical properties of iron–aluminium–(Mn, Si) lightweight steels. *Rev. Met. Paris*, 97(**10**), 1245–1253. DOI: https://doi.org/10.1051/metal:2000110
3. Shangping, Chen, Radhakanta, Rana, Arunansu, Haldar, Ranjit, Kumar Ray (2017) Current state of Fe–Mn–Al–C low density steels. *Progress in Mater. Sci.*, **89**, 345–391. DOI: https://doi.org/10.1016/j.pmatsci.2017.05.002
4. Shao-bin, Bai, Yong-an, Chen, Xin, Liu et al. (2023) Research status and development prospect of Fe–Mn–C–Al system low-density steels. *J. of Materials Research and Technology*, **25**, 1537–1559.
5. Zambrano, O.A. (2018) A general perspective of Fe–Mn–Al–C steels. *J. Mater. Sci*., 53(**20**), 14003–14062.
6. Frommeyer, G., Brüx, U. (2006) Microstructures and mechanical properties of high-strength Fe–Mn–Al–C light-weight TRIPLEX steels. *Steel Res. Int*., **77**, 627–633. DOI: https://doi.org/10.1002/srin.200606440
7. Raabe, D., Springer, H., Gutierrez-Urrutia, I. et al. (2014) Combinatorial synthesis and microstructure-property relations for low-density Fe–Mn–Al–C austenitic steels. *JOM*, **66**, 1845–1856. DOI: https://doi.org/10.1007/s11837-014-1032-x
8. Howell, R.A., Aken, D.C. (2009) A literature review of age hardening Fe–Mn–Al–C alloys. *Iron Steel Technol*., **6**, 193–212. DOI: https://scholarsmine.mst.edu/matsci_eng_facwork/1283/
9. Chen, P., Li, X., Yi, H. (2020) The κ-carbides in low-density Fe–Mn–Al–C Steels: A review on their structure, precipitation and deformation mechanism. *Metals*, 10(**8**), 1021. DOI: https://doi.org/10.3390/met10081021
10. Khaple S., Golla B.R., Prasad V.V.S. (2023) A review on the current status of Fe–Al based ferritic lightweight steel. *Defence Technology*, **26**, 1–22. DOI: https://doi.org/10.1016/j.dt.2022.11.019
11. Frommeyer, G., Drewes, E.J., Engl, B. (2000) Physical and mechanical properties of iron–aluminium–(Mn, Si) lightweight steels. *Rev. Met. Paris*, 97(**10**), 1245–1253. DOI: https://doi.org/10.1051/metal:2000110
12. Frommeyer, G., Jiménez, J.A. (2005) Structural superplasticity at higher strain rates of hypereutectoid Fe–5.5Al–1Sn–1Cr–1.3C steel. *Metall. and Mater. Transact. A*, **36**, 295–300. DOI: https://doi.org/10.1007/s11661-005-0302-1
13. Chen, P., Xiong, X.C., Wang, G.D., Yi, H.L. (2016) The origin of the brittleness of high aluminum pearlite and the method for improving ductility. *Scr. Mater*., **124**, 42–46. DOI: https://doi.org/10.1016/j.scriptamat.2016.06.031
14. Liu, D., Cai, M., Ding, H., Han, D. (2018) Control of inter/intra-granular κ-carbides and its influence on overall mechanical properties of a Fe–11Mn–10Al–1.25C low density steel. *Mater. Sci. Eng. A*, **715**, 25–32. DOI: https://doi.org/10.1016/j.msea.2017.12.102
15. Frommeyer, G., Brüx, U., Neumann P. (2003) Supra-ductile and high-strength manganese-TRIP/TWIP steels for high energy absorption purposes. *ISIJ Int.*, **43**, 438–346.
16. Gutierrez-Urrutia, I., Raabe, D. (2013) Influence of Al content and precipitation state on the mechanical behaviour of austenitic high-Mn low-density steels. *Scripta Mater.*, **68**, 343-347.
17. Gutierrez-Urrutia, I. (2021) Low density Fe–Mn–Al–C steels: phase structures, mechanisms and properties. *ISIJ Int.*, 61(**1**), 16–25.
18. Ding, H., Li, H., Misra, R.D.K. et al. (2017) Strengthening mechanisms in low density Fe–26Mn–*x*Al–1C steels. *Steel Research Int*., **89**, 1700381. DOI: https://doi.org/10.1002/srin.201700381
19. Kim, K.-W., Park, S.-J., Moon, J. et al. (2020) Characterization of microstructural evolution in austenitic Fe–Mn–Al–C lightweight steels with Cr content. *Materials Characterization*, **170**, 110717. DOI: https://doi.org/10.1016/j.matchar.2020.110717
20. Zhuang, C. Liu, J. Li, C., Tang, D. (2019) Study on high temperature solidification behavior and crack sensitivity of Fe–Mn–C–Al twip steel. *Scientific Reports*, 9(**1**), 15962–15977.
21. Lan, P. Tang, H., Zhang, J. (2016) Solidification microstructure, segregation, and shrinkage of Fe–Mn–C twinning-induced plasticity steel by simulation and experiment. *Metallurg. and Mater. Transact. A*, 47(**6**), 2964–2984.
22. Shen, Y. Liu, J. Yang, S. et al. (2019) Dendrite growth behavior in directionally solidified Fe–C–Mn–Al alloys. *J. of Crystal Growth*, **511**, 118–126.
23. Lee, C.-Y., Lee, Y.-K. (2014) The solidification mode of Fe–Mn–Al–C lightweight steel. *JOM*, 66(**9**), 1794–1799.
24. Yaozu Shen, Shufeng Yang, Jianhua Liu et al. (2019) Study on micro segregation of high alloy Fe–Mn–C–Al steel. *Steel Research Int*., **90**, 1800546. DOI: https://doi.org/10.1002/srin.201800546
25. Grajcar, A., Kaminska, M., Opiela, M. et al. (2012) Segregation of alloying elements in thermomechanically rolled medium-Mn multiphase steels. *Mater. Manuf. Eng*., 55(**2**), 256–264.
26. Wietbrock, B., Bambach, M., Seuren, S., Hirt, G. (2010) Homogenization strategy and material characterization of high-manganese TRIP and TWIP steels. *Mater. Sci. Forum*, **638–642**, 3134–3139. DOI: https://doi.org/10.4028/www.scientific.net/msf. 638-642. 3134.
27. Senk, H. Emmerich, J. Rezende, R. Siquieri D. (2007) Estimation of segregation in iron-manganese steels. *Advanced Engineering Materials*, **8**, 695–702. DOI: 10.1002/adem.200700138
28. Shen, Y. Yang, S. Liu et al. (2019) Study on micro segregation of high alloy Fe–Mn–C–Al steel. *Steel Research Int.*, 90(**5**), 2963–2975. DOI: https://doi.org/10.1002/srin.201800546
29. Jan Reitz, Burkhard Wietbrock, Silvia Richter et al. (2011) Enhanced homogenization strategy by electroslag remelting of high-manganese TRIP and TWIP steels. *Advanced Engineering Materials*, 13(**5**), 395–399. DOI: 10.1002/adem.201000322
30. Kang-Wei LI, Chang-Ling ZHUANG, Jian-Hua LIU et al. (2015) Smelting and casting technologies of Fe–25Mn–3Al–3Si twinning induced plasticity steel for automobiles. *J. of Iron and Steel Research Int.*, **22** (Supplement 1), 75–79. DOI: https://doi.org/10.1016/S1006-706X(15)30142-4
31. Sa Ge, Mihaiela Isac, Roderick Ian Lawrence Guthrie (2013) Progress in strip casting technologies for steel; technical developments. *ISIJ Int.*, 53(**5**), 729–742. DOI: https://doi.org/10.2355/isijinternational.53.729

32. Medovar, L., Stovpchenko G., Lisova, L. et al. (2023) Features and restrictions of electroslag remelting with silica-bearing slags for lightweight high manganese steel. *Steel Research Int*., 94(**10**), 202300161. DOI: https://doi.org/10.1002/srin.202300161

ORCID
Yu.V. Kostetskyi: 0000-0003-0742-0684,
G.O. Polishko: 0000-0001-7543-280X,
V.A. Kostin: 0000-0002-2677-4667,
V.P. Petrenko: 0000-0003-2440-1901,
E.O. Pedchenko: 0000-0002-8824-4389

CONFLICT OF INTEREST
The Authors declare no conflict of interest

CORRESPONDING AUTHOR
Yu.V. Kostetskyi
E.O. Paton Electric Welding Institute of the NASU
11 Kazymyr Malevych Str., 03150, Kyiv, Ukraine.
E-mail: y.kostetsky@paton.kiev.ua

SUGGESTED CITATION
V.A. Zaitsev, Yu.V. Kostetskyi, G.O. Polishko, V.A. Kostin, V.P. Petrenko, E.O. Pedchenko (2023) Investigations of the quality of metal of high-manganese steel alloyed by aluminium and chromium after electroslag remelting. *The Paton Welding J*., **12**, 39–49.

JOURNAL HOME PAGE
https://patonpublishinghouse.com/eng/journals/tpwj

Received: 05.09.2023
Accepted: 26.12.2023

NEW BOOK

Igor Ryabtsev, Serhii Fomichov, Valerii Kuznetsov, Yevgenia Chvertko, Anna Banin
Surfacing and Additive Technologies in Welded Fabrication
Springer Nature Switzerland AG 2023, 226 p.
ISBN 978-3-031-34389-6, ISBN 978-3-031-34390-2 (eBook)
https://doi.org/10.1007/978-3-031-34390-2

This book provides a comprehensive overview of a wide range of surfacing methods, detailing their physical basics and technologies.

Each section of the book provides information on the formation of the structure and properties of the deposited metal, the reasons for the formation of defects, and directions for prevention. The book also covers the certification of surfacing procedures, adhering to international standards.

With a focus on practical applications, the book is an essential reference for anyone working in the field of welding and related technologies. It includes detailed illustrations and diagrams, making it easy to understand and follow the concepts.

CONTENTS

DOI: https://doi.org/10.37434/tpwj2023.12.06

MECHANICAL CHARACTERISTICS OF WELDED JOINTS OF HIGH-STRENGTH TITANIUM ALLOYS PRODUCED BY VARIOUS WELDING METHODS

S.V. Akhonin[1], **V.Yu. Bilous**[1], **R.V. Selin**[1], **E.L. Vrzhyzhevskyi**[1], **S.L. Antonyuk**[2]

[1]E.O. Paton Electric Welding Institute of the NASU
11 Kazymyr Malevych Str., 03150, Kyiv, Ukraine. E-mail: belousvy@gmail.com
[2]SC "O.K.Antonov ANTK"
1 Acad. Tupolev Str., 03062, Kyiv, Ukraine. E-mail: info@antonov.com

ABSTRACT

Properties of welded joints of VT19 and Ti–2.8Al–5.1Mo–4.9Fe titanium pseudo-β-alloys and complex T120 titanium (α+β)-alloy, produced by electron beam and argon-arc welding and after several kinds of heat treatment (annealing, controlled annealing, quenching in water, delayed cooling) were studied. In addition to reliable protection of welded joints, another advantage of the technology of electron beam welding of titanium and alloys on its base is the possibility of performing local preheating and further heat treatment in the vacuum chamber. A quality criterion was proposed in order to compare the properties of welded joints in as-welded condition and after additional heat treatment. It was determined that performance of electron beam welding using local heat treatment and preheating, as well as making the joints by argon-arc welding using filler material, which allows lowering by 10–20 % the amount of alloying elements in the weld metal, compared to base metal, ensures a high quality of welded joints of high-strength titanium pseudo-β-alloys in as-welded condition.

KEYWORDS: titanium, titanium alloys, two-phase, (α+β)-, sparsely-doped, pseudo-β-, welded joints, heat treatment, annealing, quenching, aging, microstructure, mechanical properties

INTRODUCTION

A considerable increase of the scope of investigations aimed at producing titanium alloys with a new set of properties has been observed over the recent decades [1–3]. In the leading world materials science centers of the USA, China and EC intensive work is being conducted on development of new titanium alloys with enhanced performance.

Structural pseudo-β-titanium alloys are some of the most promising titanium-based metal materials. One of the advantages of the modern pseudo-β-alloys of titanium is their high manufacturability, which allows them to be deformed at lower forces and temperatures than the traditional high-temperature and high-strength alloys with pseudo-α- and (α+β) structures [3, 4]. In addition, heat treatment of structures from these alloys can be performed without their transferring into the quenching medium, which reduces the deformational and residual stresses and prevents metal oxidation [5]. The possibility of comparing the properties of pseudo-β-alloy welded joints with those of high-strength (α+β)-alloys attracts special attention.

A wider application of titanium alloys in different industries requires both improving their mechanical characteristics [6], and lowering the production cost, which can be achieved by developing new alloys with improved service properties and application of new high-efficient manufacturing technologies, including welding.

As regards pseudo-β-alloys of titanium there is a tendency in the world practice of application of alloying elements, which have a relatively low cost. It allows reducing the cost of the production process and lowering the cost of the semi-finished products, respectively [7]. Such alloys are usually called sparsely-doped. The sparsely-doped titanium alloys include low alloys which do not contain expensive or deficit elements (Mo, Ta, Zr, Nb, W, etc.) and have relatively inexpensive components of commercial purity at the base of their alloying systems (Al, Fe, Cu, etc.). Sparsely-doped alloys can also contain oxygen as an alloying element [8].

Alloys, which harden to β-phase at rapid cooling from β-region temperatures, are considered to be titanium β-alloys. Coefficient of β-stabilization of such alloys is $K_\beta > 1$ [9]. Among these alloys, β-alloys and alloys with a relatively small amount of α-phase — pseudo-β-alloys with $K_\beta = 1.4 – 2.4$ are singled out, the polymorphous transformation running by β→(β+α) scheme here. In a stable condition they have (β+α) structure [10].

A special feature of pseudo-β-alloys is their high ductility, which allows them to be subjected to intense cold deformation. At treatment for β-solid solution, pseudo-β and β-titanium alloys compared to α- or α+β-alloys, have the same yield limit, much higher

Copyright © The Author(s)

ductility and fracture toughness, as well as higher deformability at different kinds of loading. At the same time, their strength properties can be significantly higher due to aging, which leads to decomposition of β-solid solution and precipitation of strengthening phases [11, 12].

Investigations of the properties of welded joints of alloys having a large amount of β-stabilizers, revealed their significant shortcomings: high susceptibility to alloying element liquation, strong dependence of aging duration on the content of alloying elements and impurities, as well as low thermal stability, which is due to precipitation of intermetallics, for instance $TiCr_2$ in these alloy structure [13]. In welding sparsely-doped pseudo-β-alloys the welded joints have the following shortcomings: insufficient level of strength, ductility, instability of properties, as a result of which they are recommended for application in "ground objects" (medical implants, automotive parts and different decorative products).

Therefore, it is rational to assess the properties of welded joints of structural and sparsely-doped titanium pseudo-β-alloys made by electron beam (EBW) and argon-arc welding (AAW), and to compare them with the properties of welded joints of a high-strength complex titanium (α+β) alloy T120 of Ti–5.5Al–2.8. Mo–2.3V–4Nb–1.3Cr–1Fe–2.7Zr system, and well as to determine the level of welded joint hardening due to heat treatment.

The objective of this work is determination of the influence of electron beam and argon-arc welding and of several kinds of heat treatment, such as annealing, quenching in water, controlled annealing, delayed cooling, on the properties of base metal and welded joints of titanium pseudo-β-alloys VT19, Ti–2.8Al–5.1Mo–4.9Fe (LCB-5.1) and (α+β)-alloy T120, made by fusion welding.

EXPERIMENTAL PROCEDURE

To achieve the defined objective, we studied the structure and properties of base metal and joints of titanium pseudo-β-alloys VT19, Ti–2.8Al–5.1Mo–4.9Fe (LCB-5.1) and (α+β)-alloy T120 [14, 15], produced by tungsten-electrode argon-arc welding with through penetration and by electron beam welding, which were subjected to postweld heat treatment.

EBW of 10 mm thick samples from structural pseudo-β-alloy VT19, from sparsely-doped pseudo-β-alloys, such as Timet LCB and Ti–2.8Al–5.1Mo–4.9Fe (LCB-5.1) alloys, and (α+β)-alloy T120. EBW modes are given in Table 1. One of the advantages of the technology of EBW of titanium and alloys on its base, in addition to ensuring reliable protection of the welded joints, is the possibility of performing local preheating and further heat treatment in the vacuum chamber [16, 17]. Modes of EBW with local heat treatment (LHT) of 10 mm thick joints with welding speeds of 7 mm/s are given in Table 1.

AAW of 6 mm thick samples of VT19, Ti–2.8Al–5.1Mo–4.9Fe (LCB-5.1) alloys and (α+β)-alloy T120 was also performed. Modes of through penetration AAW without filler metal application are presented in Table 2. For promising high-strength titanium alloys, such as VT19, sparsely-doped LCB-5.1 alloy and (α+β)-alloy T120, welding wires of the respective chemical composition are not available. Therefore, if required, it is rational to use unalloyed titanium wire of VT1-00sv brand as filler metal, which allows, without changing the weld alloying system, reducing the content of alloying elements in the weld metal, depending on welding conditions. Modes 9-12 (Table 2) are for AAW with filler wire.

Titanium alloy welded joints can be produced in modes with different energy input values. To assess the efficiency of the selected welding mode, as well as after heat treatment of welded joints of high-strength titanium alloys, a criterion of welding mode quality in conditional units was proposed, which consists of the contribution of the modes of welding and heat treatment into comprehensive increase in overall indices of strength, ductility and impact toughness of titanium alloy welded joints relative to base metal of the respective alloy. On the whole

Table 1. Modes of EBW of experimental pseudo-β-titanium alloys VT19, LCB-5.1 and (α+β)-alloy T120

Mode	Alloy grade	Beam current, I_b, mA	V_w, mm/s	T_{pr}, °C	LHT temperature, °C	LHT duration, min
1	VT19	120	7	–	–	–
2	–»–	–»–	11	–	–	–
3	Timet LCB	–»–	7	–	–	–
4	LCB-5.1	–»–	–»–	–	–	–
5	VT19	90	–»–	400	–	–
6	–»–	–»–	–»–	–»–	750	10
7	LCB-5.1	–»–	–»–	–»–	–	–
8	–»–	–»–	–»–	–»–	750	10
9	T120, T110	–»–	–»–	–	–	–
10	T120	–»–	–»–	–	900	10

Table 2. Modes of AAW of high-strength pseudo-β-titanium alloys VT19, LCB-5.1 and (α+β)-alloy T120

Mode	Alloy	I_w, A	U_a, V	V_w, m/h	T_{pr}, °C	$V_{w\,f}$, m/h	Filler metal content in the weld, %
1	VT19	310	12	10	–	–	–
3 (over flux)	–»–	220	11	–»–	–	–	–
5 (over flux)	–»–	320	–»–	16		–	–
6	LCB-5.1	330	12	10	–	–	–
7	–»–	310	–»–	–»–	400	–	–
8 (over flux)	–»–	240	11	16	–	–	–
9	VT19	380	12	8	–	30	10
10	–»–	420	–»–	–»–	–	60	20
11	LCB-5.1	350	–»–	10	–	30	10
12	–»–	–»–	–»–	–»–	–	60	20
13	T120	380	–»–	–»–		–	–
14	–»–	360	11	16	–	–	–
15	–»–	320	–»–	10	–	–	–
16	–»–	350	12	–»–	–	30	10
17	–»–	–»–	–»–	–»–	–	60	20

for titanium alloys increase of some mechanical properties, for instance, strength, cases a respective lowering of ductility and impact toughness values. In some cases, however, it goes out of proportion. Analysis of the obtained results of welded joint mechanical characteristics led to the conclusion that in titanium alloy welded joints having high ductility values, the impact toughness values are at a high level. In the case, if we consider just the strength and impact toughness values, and determine their significance as equal, a coefficient of welding mode quality was proposed, which is defined as follows:

$$K_{w\,m} = 0.5(\sigma_w/\sigma_{BM}) + 0.5(KCV_w/KCV_{BM}).$$

The strength coefficient was also calculated by the following formula:

$$K_{w\,m} = \sigma_w/\sigma_{BM}.$$

RESULTS AND THEIR DISCUSSION

JOINT PROPERTIES AFTER WELDING

Welded joints of sparsely-doped Timet LCB titanium alloy have the highest strength. For this alloy the values of as-welded joint strength are equal to 1068 MPa or 89 % of base metal strength (Table 3). Impact toughness of samples with a sharp notch (*KCV*) of weld metal of Timet LCB alloy welded joints made by EBW, is equal to 3.2 J/cm^2. Strength of LCB-5.1 alloy welded joint is on the level of 95 % of that of base metal in as-rolled condition. On the whole, the strength of welded joints of the considered sparsely-doped alloys in as-welded condition after EBW is on the level of 90 % of that of as-rolled alloy.

Conducted studies led to the conclusion that the strength of VT19 alloy welded joints is the highest in the condition after preheating and LHT, but their quality factor is lower than that of welded joints after EBW without preheating or LHT. This is attributable to high values of impact toughness of VT19 alloy welded joints without preheating or LHT. Lowering of this welded joint strength at calculation of the quality characteristic is compensated by high values of relative elongation and impact toughness. High values of relative elongation and impact toughness are associated with a large amount of metastable β-phase in the weld metal after EBW.

Sparsely-doped pseudo-β-alloys have lower values of quality characteristic in the condition after EBW, compared to structural pseudo-β-alloy VT19. Quality characteristic of EB welded joints of high-strength (α+β)-alloy T120 is lower than the values of this characteristic for pseudo-β-alloys. EB welded joints after LHT have the highest values of quality characteristic of (α+β)-alloy T120 (Table 3).

In terms of mechanical properties, EB welded joints of sparsely-doped LCB-5.1 titanium alloy have lower values of strength in as-welded condition and of quality factor, compared to structural alloy VT19. Welded joints of (α+β)-alloy T120 have the lowest values of strength in as-welded condition and of the quality factor.

The highest values of strength in as-welded condition and of the quality factor are demonstrated by LCB-5.1 alloy joints made by EBW with application of preheating and LHT.

Investigation of mechanical properties of welded joints of titanium pseudo-β-alloys made by tungsten electrode AAW (including use of flux) showed that the strength values in as-welded condition are on the same level, while VT19 alloy joints made without flux application have larger values of the quality factor (Table 4). For LCB-5.1 alloy flux application ensured the highest values of quality characteristic for welds

Table 3. Properties of 10 mm thick EB welded joints of pseudo-β-titanium alloys VT19, LCB-5.1 and (α+β)-alloy T120

Sample	σ_t, MPa	$\sigma_{0.2}$, MPa	δ, %	*KCV*, J/cm^2	$K_{w\,m}$	K_s
VT19, BM	958	887	12	29	–	–
VT19, welded joint: mode 1;	876	842	11.3	28	0.93	0.91
mode 2;	891	847	10.0	27	–»–	0.93
mode 5 (preheat 400 °C);	893	879	12.0	20	0.8	–»–
mode 6 (preheat 400 °C, LHT 750 °C)	937	868	5.3	21	0.85	0.98
Timet LCB, BM	1187	1145	12.7	13	–	–
Timet LCB, welded joint, mode 3	1068	1033	5.1	3.2	0.57	0.89
LCB-5.1, BM	1015	939	1.9	6.4	–	–
LCB-5.1, welded joint: mode 4;	960	921	3.8	3.6	0.75	0.94
mode 7 (preheat 400 °C);	992	959	5.1	3.6	0.76	0.98
mode 4 (preheat 400 °C, LHT 750 °C)	997	964	6.5	5.3	0.9	0.98
T120, BM	1133	1040	10.7	33	–	–
T120, welded joint: mode 9;	1082	1006	6.7	15.2	0.72	0.95
mode 10 (LHT 750 °C)	1061	1012	8.0	24	0.85	0.93
T110, BM	1130	999	6	38	–	–
T11, welded joint, mode 9	1080	–	–	11	0.62	0.96

made without changing the weld metal chemical composition. Application of filler wire and the associated change in the weld metal chemical composition and welded joint properties allowed increasing both the values of strength properties, and those of quality characteristics of the welded joints. Values of quality characteristics of welded joints of (α+β)-alloy T120 are inferior to respective values for pseudo-β-alloys.

The highest values of quality characteristics in as-welded condition were determined for welded joints of VT19 alloy made by AAW with addition of VT1-00sv filler wire in the amount of 20 %, and of sparsely-doped LCB-5.1 alloy, made with addition of VT1-00sv filler wire in the amount of 10 %. Values of quality characteristics of these welded joints are higher than those of EB welded joints.

Table 4. Mechanical properties of welded joints of pseudo-β-alloys VT19, LCB-5.1 and (α+β)-alloy T120 made by AAW, in as-welded condition

Sample	Alloy, sample	σ_t, MPa	$\sigma_{0.2}$, MPa	δ. %	*KCV*, J/cm^2	$K_{w\,m}$	K_s
1	VT19, welded joint	860	839	13.3	19	0.77	0.89
3	VT19, welded joint over a layer of flux	857	815	13.3	14	0.68	–»–
5	–»–	849	813	10.7	13	0.66	0.88
6	LCB-5.1, joint	921	–	–	4.9	0.89	0.85
7	LCB-5.1, joint with 400 °C preheating	799	–	–	4.3	0.77	0.74
8	LCB-5.1, joint over a layer of flux	972	936	10.0	5.7	0.99	0.90
9	VT19, VT1-00sv joint, 10 %	895	868	7.3	28	0.93	0.93
10	VT19, VT1-00sv joint, 20 %	963	942	6	32	1.01	0.89
11	LCB-5.1, VT1-00sv joint, 10 %	1002	–	–	5.5	0.98	0.93
12	LCB-5.1, VT1-00sv joint, 20 %	960	–	–	3.5	0.75	0.89
13	T120, V_w = 10 m/h	1157	1076.9	–	17.6	0.79	1.02
14	T120, over flux, V_w = 16 m/h	1162	1069	–	4.6	0.58	0.12
15	T120 over flux, V_w = 10 m/h	1075	985	15.3	4.9	0.55	0.95
16	T120, VT1-00sv filler, 10 %	1110	1047	–	24.2	0.88	0.98
17	T120, VT1-00sv filler, 25 %	1006	937.8	4.0	14.1	0.67	0.89

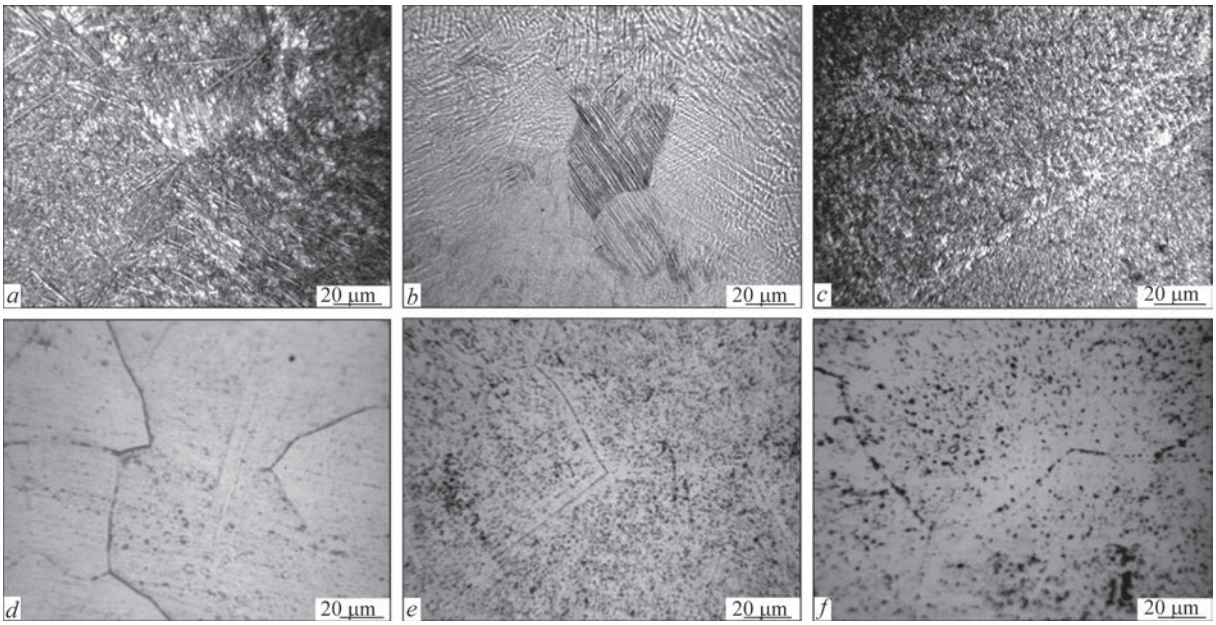

Figure 1. Microstructure of weld metal of EB welded joints: *a* — T120 base metal; *b* — T120 weld metal; *c* — T120 weld metal after LHT at 850 °C; *d* — VT19 weld metal; *e* — Timet LCB weld metal; *f* — LCB-5.1 weld metal

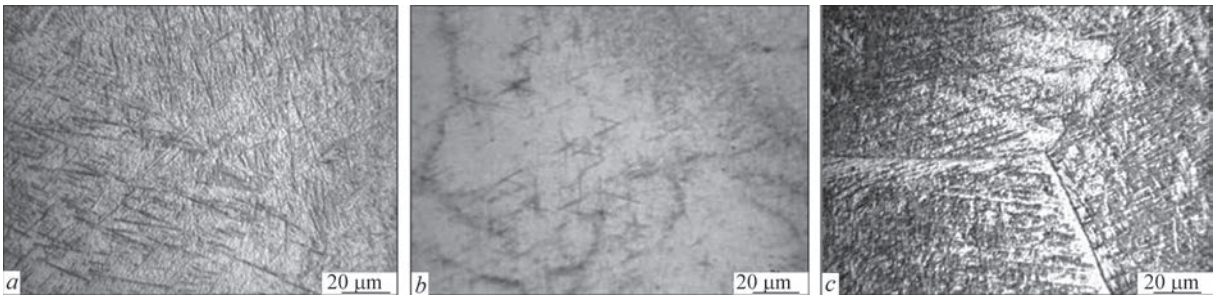

Figure 2. Microstructure of weld metal of AAW welded joints of T120 alloy: *a* — weld metal (mode 13); *b* — weld metal, over flux (mode 14); *c* — metal of the weld made with VT1-00sv filler wire (mode 16)

Lowering of strength in welded joints of all the alloys is attributable to increase of the amount of β-phase in the weld metal after EBW impact (Figure 1, *b*), compared to base metal (Figure 1, *a*). LHT application for T120 alloy allowed reducing the amount of β-phase almost to base metal level (Figure 1, *c*). The largest amount of β-phase in as-welded condition is determined in the weld metal of the welded joint of pseudo-β-alloy VT19, which consists of practically pure β-phase (Figure 1, *d*). In the weld metal of Timet LCB and LCB-5.1 alloys the amount of β-phase is also increased, but it is smaller compared to VT19 alloy.

A larger amount of β-phase is also found in as-welded condition in the structure of the metal of T120 alloy welds made by AAW (Figure 2). Here, flux application leads to increase of the amount of β-phase (Figure 2, *b*), while addition of unalloyed VT1-00sv filler metal and reduction of alloying element content leads to reduction of the amount of β-phase in the weld metal (Figure 2, *c*).

Thus, properties of welded joints of pseudo-β-alloys VT19, LCB-5.1 and (α+β)-alloy T120 made by EBW and AAW were studied, and it was determined that in as-welded condition the highest quality characteristics are typical for joints produced with addition of VT1-00sv filler wire in modes ensuring VT1-00 metal content in the weld on the level of 10 % for LCB-5.1 alloy, and on the level of 20 % for VT19 alloy.

INFLUENCE OF HEAT TREATMENT ON WELDED JOINT PROPERTIES

Heat treatment (HT) of welded joints of pseudo-β-titanium alloys is performed to eliminate internal stresses, achieve optimal physico-mechanical properties and stable structure not prone to a change of phase composition or properties at long-term heating at working temperatures. With this purpose, the influence of furnace annealing, quenching with subsequent aging and delayed cooling with the furnace at the rate of 1 °C/min on the properties of welded joints of pseudo-β-titanium alloys VT19 and LCB-5.1, made by EBW and AAW, in particular with application of filler wire VT-00sv [18, 19] was studied. Heat treatment modes are given in Table 5.

Table 5. Modes of furnace heat treatment of welded joints of pseudo-β-alloys VT19, LCB-5.1 and (α+β)-alloy T120

HT mode	Hardening HT type
1	VT19, LCB-5.1 annealing: heating up to 750 °C temperature, 1 h soaking, cooling with furnace
2	VT19, LCB-5.1 hardening and aging: heating up to 750 °C temperature, 1 h soaking, quenching in water, aging at 450 °C, 4 h soaking, cooling in air
3	VT19, LCB-5.1 delayed cooling: heating up to 750 °C temperature, 1 h soaking, cooling at a controlled rate of 1 °C/min
4	VT19, LCB-5.1 controlled annealing: heating and soaking at the temperature of 750 °C for 1 h; cooling to 680 °C, 1 h soaking; cooling to 380 °C; 8 h soaking, cooling in air; aging at 450 °C, 4 h soaking, cooling in air
5	T120 annealing: heating up to 900 °C temperature, 1 h soaking, cooling with the furnace
6	T120 controlled annealing: heating to 870 °C; 1 h soaking, cooling with furnace to 800 °C; 1 h soaking, cooling in air; aging at 380 °C for 8 h, cooling in air; 550 °C 2 h, cooling in air
7	T120 quenching and aging: heating up to 850 °C temperature, 1 h soaking, quenching in water, aging at 550 °C, 4 h soaking, cooling in air

Studying mechanical properties of welded joints of titanium pseudo-β-alloys VT19 and LCB-5.1 alloy led to the conclusion that in as-annealed condition AAW joints have the highest quality characteristics, for VT19 alloy without the filler wire and for LCB-5.1 alloy with filler wire in the amount of 10 % in the weld metal (Table 6).

On the whole, the strength of many welded joints in as-annealed condition is on the level not lower than that of base metal.

For (α+β) alloy T120, welded joints made by AAW with filler wire in the amount of 10 % in the weld metal have the highest values of the quality characteristic, due to high impact toughness values.

Analysis of mechanical properties of welded joints of sparsely-doped titanium pseudo-β-alloy LCB-5.1 and structural pseudo-β-alloy VT19, subjected to such kinds of thermal hardening as quenching in water with aging and delayed cooling with the controlled rate of 1 °C/min, led to the conclusion that the joints made without a change of chemical composition of the weld metal, namely by EBW and AAW without filler, have the highest values of quality characteristic (Table 7). EBW joints have the highest strength values.

Table 6. Mechanical properties of welded joints of pseudo-β-alloys VT19. LCB-5.1 and (α+β)-alloy T120б made by AAW and EBW. in as-annealed condition

Sample	σ_t, MPa	$\sigma_{0.2}$, MPa	δ, %	*KCV*, J/cm^2	$K_{w\,m}$	K_s
VT19, EBW joint, V_w = 7 mm/s, preheating at 400 °C	1027	986	12.0	26	0.98	1.07
VT19, EBW joint, V_w = 11 mm/s	1024	984.9	8.7	24	0.94	1.06
VT19, AAW joint without filler	981	946	9.7	29.4	1.01	1.02
VT19, AAW joint with filler, 20 % VT1-00sv in the weld	1011	989	9.1	25.9	0.97	1.05
LCB-5.1 BM	1071	971	–	7.2	–	–
LCB-5.1, EBW joint	1169	1141	1.3	4.8	0.87	1.09
LCB-5.1, AAW joint without filler	1082	1033	–	5.3	0.87	1.01
LCB-5.1, AAW joint over flux	1197	1146	–	6.0	0.97	1.11
LCB-5.1, AAW joint with filler, 10 % VT1-00sv in the weld	1463	–	–	7.3	1.18	1.36
T120, EBW joint	1051.3	942.6	14.7	51.9	1.3	0.92
T120, AAW joint without filler	1013	936.3	4.0	42.9	1.13	0.89
T120, AAW joint over flux, V_w = 16 m/h	1151	1074	–	34.6	1.06	1.02
T120, AAW joint with 10 % VT1-00sv	1168	1083.6	4.0	48	1.29	1.03
T120, AAW joint with 25 % VT1-00sv	921	841	5.1	49	1.19	0.81

Table 7. Mechanical properties of welded joints of VT19, LCB-5.1 and T120 alloys made by AAW and EBW, in the condition after hardening HT

Sample	HT mode	σ_t, MPa	$\sigma_{0.2}$, MPa	δ, %	*KCV*, J/cm^2	$K_{w\,m}$	K_s
LCB-5.1, AAW over flux	2, quenching in water and aging	1156	1127	4.2	6.9	1.10	1.13
LCB-5.1, AAW with VT1-00sv filler, 10 %	–»–	1055	1055	2.8	5.3	0.93	1.04
LCB-5.1, AAW with VT1-00sv filler, 10 %	3, delayed cooling	958	958	1.3	6.5	0.98	0.94
LCB-5.1, EBW	2, quenching in water and aging	1204	1199	8.6	4.2	0.92	1.19
LCB-5.1, EBW	3, delayed cooling	964	905	4.7	7.1	1.02	0.95
VT19, EBW	Quenching in water and aging	1285	1234	4.7	23.0	1.06	1.34
VT19, AAW	–»–	1273	–	–	11.0	0.85	1.33
VT19, EBW	EBW, delayed cooling	1068	1012	11.3	23.0	0.95	1.11
VT19, AAW	AAW, delayed cooling	1033	1005	6.0	24.0	0.95	1.07
T120, EBW	7, quenching in water and aging	1348	1275.3	1.3	8.3	0.73	1.19
T120, EBW	6, controlled annealing	1204.6	1109.3	4.5	13.2	0.74	1.06
T120, AAW without filler	7, quenching in water and aging	1350.6	1255	–	9.7	0.75	1.19
T120, AAW without filler	6, controlled annealing	1253.1	1165.2	2	16.3	0.81	1.1
T120, AAW with 10 % VT1-00sv filler	7, quenching in water and aging	1318	1305.7	2.7	10.8	0.75	1.16
T120, AAW with 10 % VT1-00sv filler	2, controlled annealing	1105.6	1040.4	–»–	18.1	0.77	0.98

Comparing the influence of HT without transferring to the quenching medium, namely annealing and delayed cooling, the annealed joints have the highest strength values. Annealing allows ensuring equal strength of the welded joints of titanium alloy VT19 and sparsely-doped LCB-5.1.

All the conducted HT operations lead to formation of a homogeneous structure in the welded joint and reduction of the amount of β-phase in the weld metal (Figure 3). After quenching the intragranular structure of T120 alloy welded joints consists of platelike α-phase, which here forms the basket weave pattern, while the platelike α-phase thickness is the smallest and equal to 0.7–1.0 μm (Figure 3, *b*). After controlled annealing the weld metal forms α-phase plates of different dimensions. They are characterized by a great diversity of structural element parameters with high impact toughness values (Figure 3, *c*).

After HT, the weld metal microstructure in pseudo-β-alloys also consists of equiaxed primary β-grains elongated in the direction of heat removal, where β-phase decomposition occurred at annealing, with formation of a uniform homogeneous (α+β)-structure with platelike α-phase of different length (1–5 μm) and thickness (0.5–1.0 μm) (Figure 4).

After quenching and aging the microstructure of weld metal is the most finely dispersed, the size of decomposition products most often does not exceed 1 μm (Figure 4, *b*). After delayed cooling at a controlled rate of 1 °C/min and controlled annealing, particles of α-phase 1.0–1.5 μm thick are observed in the weld metal structure (Figure 4, *c*, *d*).

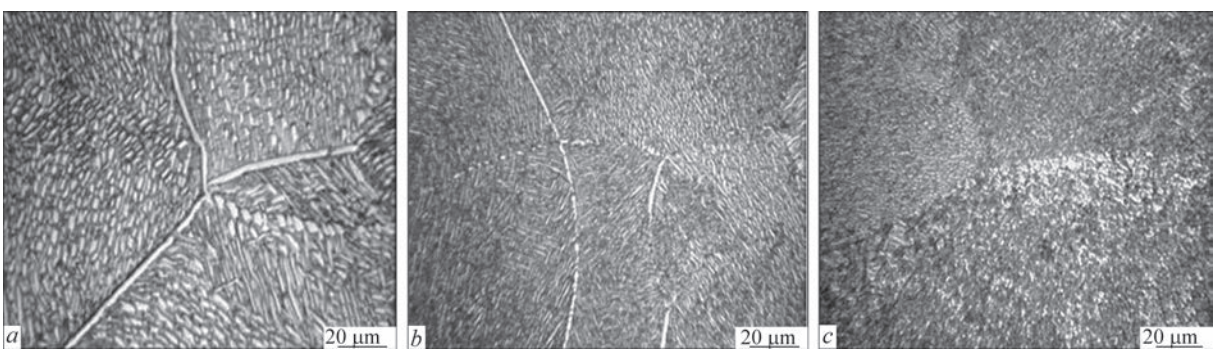

Figure 3. Microstructure of weld metal of T120 titanium alloy joint after HT: *a* — annealing; *b* — quenching; *c* — controlled annealing

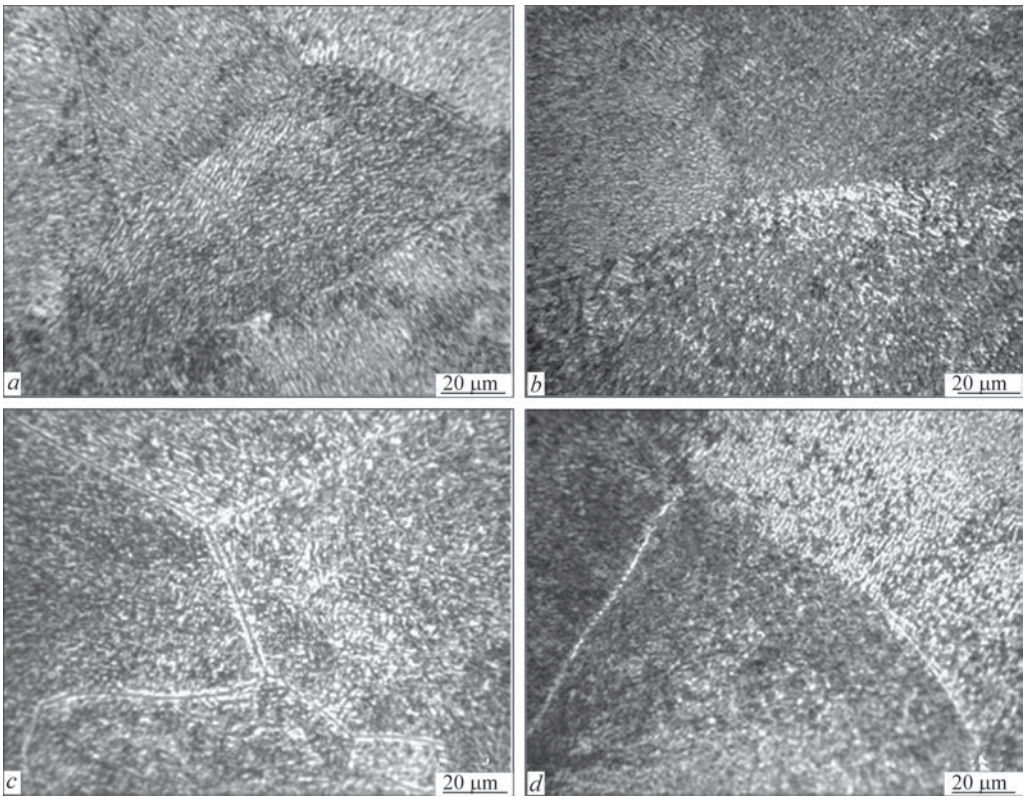

Figure 4. Microstructure of weld metal of EB welded joint of pseudo-β-alloy VT19 after HT: *a* — annealing; *b* — quenching and aging; *c* — delayed cooling; *d* — controlled annealing

Thus, comparison of quality factors of welding modes for pseudo-β-titanium alloy VT19 and LCB-5.1 alloy leads to the conclusion that AAW with feeding of the lower alloyed filler material is the most efficient welding mode for structural alloy VT19 (Figure 5). Here, for structural alloy VT19 it is rational to lower the degree of weld metal alloying by 20 %, and for sparsely-doped pseudo-β-alloy LCB-5.1 — by 10 %. This attributable to a greater amount of alloying element Fe which makes a large contribution to hardening of LCB-5.1 alloy.

Comparison of strength values of EB welded joints of pseudo-β-alloys led to the conclusion that the greatest hardening of welded joints compared with the metal in as-rolled condition is ensured by quenching in water and aging, and the least quenching is provided by delayed cooling at a controlled rate.

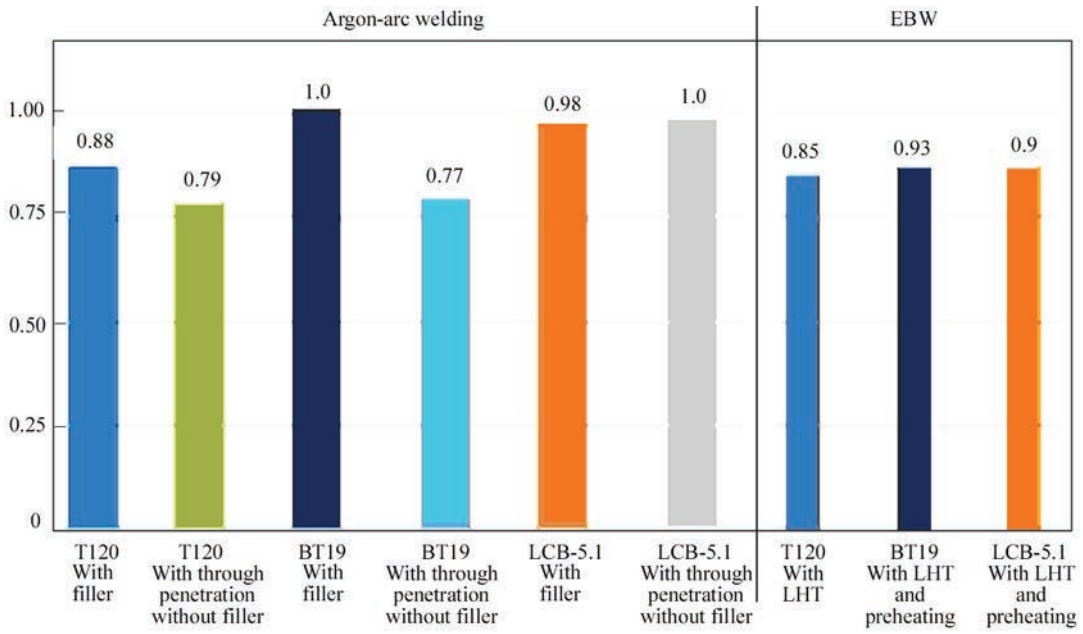

Figure 5. Quality factors of welded joints for some AAW and EBW modes in as-welded condition

CONCLUSIONS

1. It was established that the high quality of welded joints of promising high-strength titanium pseudo-β-alloys in as-welded condition can be ensured by performing EBW with application of LHT and preheating, as well as making the welded joints by AAW with the use of filler material, which allows reducing by 10–20 % the amount of alloying elements in the weld metal compared to base metal.

2. Lowering of strength of welded joints of pseudo-β-alloys is associated with increase of the amount of β-phase in the weld metal and HAZ.

3. It was determined that the highest quality factor of welded joints of structural pseudo-β-titanium alloy VT19 and (α+β)-alloy T120 is provided by AAW with feeding of unalloyed filler material VT1-00sv in the welding modes, which ensure 10 % filler metal content in the weld.

4. The highest quality factor of welded joints of sparsely-doped titanium pseudo-β-alloy LCB-5.1 is provided by EBW, which envisages application of preheating and LHT.

5. Values of quality characteristic and strength coefficient of welded joints of (α+β)-alloy T120 are inferior to the respective values of pseudo-β-alloys.

REFERENCES

1. Boyer, R.R., Williams, J.C. (2011) Developments in research and applications in the titanium industry in the USA. *Proc. of 12th World Conf. on Titanium*, **I**, 10–19.
2. (2013) *Titanium Metal: Market Outlook to 2018*. 6th Ed. Roskill Information Services Ltd, USA.
3. Dobrescu, M., Dimitriu, S., Vasilescu, M. (2011) Studies on Ti–Al–Fe low-cost titanium alloys manufacturing, processing and applications. *Metalurgia Int.*, 16(**4**), 73.
4. Boyer, R.R., Briggs, R.D. (2005) The use of β titanium alloys in the aerospace industry. *J. Mater. Eng. and Performance*, 14(**6**), 681–685.
5. Cotton, J.D., Briggs, R.D., Boyer, R.R. et al. (2015) State of the art in beta titanium alloys for airframe applications. *JOM*, 67(**6**), 1281–1303.
6. Liu, H., Wang, Haomin, Zhang, Zhen et al. (2019) Enhancing the mechanical properties of electron beam welded TC17 titanium alloy joint by post-weld heat treatment. *J. of Alloys and Compounds*, **810**, 151–937.
7. Bolzoni, Leandro, Elisa María Ruiz-Navas, Elena Gordo (2017) Quantifying the properties of low-cost powder metallurgy titanium alloys. *Materials Sci. and Eng.: A*, **687**, 47–53.
8. Kaur, M., Singh, K. (2019) Review on titanium and titanium based alloys as biomaterials for orthopedic applications. *Materials Sci. and Eng.: C*, **102**, 844–862.
9. Froes, F.H. (2015) *Titanium physical metallurgy processing and applications*. USA, ASM Int., 265–269.
10. Weiping, F., Xiao, T, Zhang, Y.P. et al. (2019) Stress corrosion crack sensitivity of ultra-thick TC4 titanium alloy electron beam welding joints. *Transact. of the China Welding Institution*, **40**, 121–8.
11. Tang, B., Kou, H., Zhang, X. et al. (2016) Study on the formation mechanism of α lamellae in a near β titanium alloy. *Prog. Nat. Sci. Mater. Int*., **26**, 385–390. DOI: https://doi.org/10.1016/J.PNSC.2016.06.009
12. Fan, J.K., Kou, H.C., Lai, M.J. et al. (2013) Hot deformation mechanism and microstructure evolution of a new near β-titanium alloy. *Materials Sci. and Eng. A*, **584**, 121–132.
13. Moiseev, V.N., Kulikov, R.F., Kirillov, Yu.G. et al. (1979) *Welded joints of titanium alloys*. Moscow, Metallurgiya [in Russian].
14. Khorev, A.I. (2012) Titanium superalloy VT19. *Tekhnologiya Mashinostroeniya,* **6**, 2–5 [in Russian].
15. Akhonin, S.V., Severin, A.Yu., Belous, V.Yu. et al. (2017) Structure and properties of titanium alloy VT19, produced by the electron beam melting, after thermomechanical treatment. *Sovrem. Elektrometall.*, **3**, 19–24 [in Russian]. DOI: https://doi.org/10.15407/sem2017.03.04
16. Li, Y., Wang, H., Han, K. et al. (2017). Microstructure of Ti–45Al–8.5 Nb-0.2 W-0.03 Y electron beam welding joints. *J. Mater. Proc. Technol.*, **250**, 401–409.
17. Liu, P., Zhang, G.M., Zhai, T., Feng, K.Y. (2017) Effect of treatment in weld surface on fatigue and fracture behavior of titanium alloys welded joints by vacuum electron beam welding. *Vacuum*, **141**, 176–180.
18. Akhonin, S.V., Bilous, V.Yu., Selin, R.V., Petrichenko, I.K. (2020) Heat treatment of high-strength pseudo-β-titanium alloy produced by EBM process and of its welded joints. *Suchasna Elektrometal.*, **1**, 14–25 [in Ukrainian]. DOI: https://doi.org/10.37434/sem2020.01.02
19. Akhnonin, S.V., Bilous, V.Yu., Selin, R.V. et al. (2021) Influence of heat treatment on the structure and properties of welded joints of high-strength titanium alloys based on β-phase. *Suchasna Elektrometal.*, **4**, 51–58 [in Ukrainian]. DOI: https://doi.org/10.37434/sem2021.04.08

ORCID

S.V. Akhonin: 0000-0002-7746-2946,
V.Yu. Bilous: 0000-0002-0082-8030,
R.V. Selin: 0000-0002-2990-1131,
E.L. Vrzhyzhevskyi: 0000-0001-8651-8510

CONFLICT OF INTEREST

The Authors declare no conflict of interest

CORRESPONDING AUTHOR

V.Yu. Bilous
E.O. Paton Electric Welding Institute of the NASU
11 Kazymyr Malevych Str., 03150, Kyiv, Ukraine.
E-mail: belousvy@gmail.com

SUGGESTED CITATION

S.V. Akhonin, V.Yu. Bilous, R.V. Selin, E.L. Vrzhyzhevskyi, S.L. Antonyuk (2023) Mechanical characteristics of welded joints of high-strength titanium alloys produced by various welding methods. *The Paton Welding J*., **12**, 50–58.

JOURNAL HOME PAGE

https://patonpublishinghouse.com/eng/journals/tpwj

Received: 02.10.2023
Accepted: 26.12.2023

“DNEPROMETIZ” — NEW SOLUTIONS FOR WELDERS

“Dneprometiz” is a leading manufacturer of hardware in Ukraine, specializing in the production of low- and high-carbon wire. In order to meet the needs of consumers, the company is actively developing the production of welding wire of the Sv-08G2S and 4Si1 brands. Welding wire produced by “Dneprometiz” successfully competes with the products of European manufacturers in the markets of different countries, thanks to its high reliability and European quality. The range of welding wire packaging offered by the “Dneprometiz” plant has been expanded with a new type — 250 kg barrels. Welding wire in barrels is used for robotic welding complexes. It is impossible to imagine the work of large-scale production without robotic technology. In particular, it is better to entrust welding to special welders. The operation of such equipment is more productive and has stable quality, and it also completely eliminates the risks of injury during welding. Welders automatically join and create metal structures of varying degrees of complexity, from the largest to the smallest. Many models and a variety of software allow you to customize the manipulator for the finest, almost jewelry work. Such devices perform the same type of operations at high speed. They are also capable of performing different types of tasks, either individually or simultaneously.

As part of the implementation of an investment program aimed at modernizing production, in July the plant received new equipment for winding welding wire into 250 kg barrels. Production capacity is 1500 tons per year. The launch of the new line took place in October 2023. All tests were successfully completed, the products demonstrated good welding and technological properties. The use of welding wire in 250 kg barrels in production has a number of advantages:

- The balance of the wire and high-quality copper coating ensures stable current conductivity in the contact (wire-tip).
- Productivity increases due to continuous operation of welding machines.
- Wire is threaded into the torch less frequently and, as a result, its losses for the threading ends are reduced.
- The wire from the barrel goes directly into the hose, thereby protecting it from dust and clogging of the feed channel.
- Layer-by-layer laying of wire along the height of the container facilitates easy feeding into the welding zone and accuracy of its positioning in the weld.
- The packaging is made from fully recyclable materials and does not cause any harm to the environment.

- Impossibility of wire theft due to the large weight and volume of the packaging.
- Continuous feed of wire into the welding zone allows making long welds and improves their quality.
- Welders do not need to strain themselves physically, constantly changing cassettes with wire and wasting working time.
- It reduces the need for maintenance of the welding machine mechanism.

Currently, about 98 % of steel structures are welded. High quality and durability of metal welded structures depend on the quality of welding work and the efficiency of welding materials. One of the main conditions for welding metal structures, which affects their quality and performance, is the correct choice of the welding wire used, which must have high technological and mechanical properties, since it is the main material that provides the necessary chemical composition and properties of the weld metal. In this case, the most widely used welding electrode wire is made of silicon-manganese steel, of type Sv-08G2S grade. Welding wire of Sv-08G2S brand is produced both in a copper-plated version (for protection against corrosion) and without coating. This popularity is explained by a wide range of applications, high versatility and excellent quality of welded joints.

In the production of welding wire, the most modern equipment from the leading Swedish manufacturer Lämneå Bruk AB and high-quality raw materials are used. Quality control of the wire rod used in production, as well as testing of finished products, are carried out in our own accredited laboratory, equipped with instruments and test equipment for chemical analysis, mechanical tests, as well as welding and technological tests.

This allows the plant to produce “extra-class” products, the highest quality of which has been proven when used at leading industrial enterprises. In 2020, 4Si1 welding wire was certified to meet the requirements of EU standards. SV-08G2S and G4Si1 welding wire manufactured by “Dneprometiz” Is delivered in accordance with EN ISO, AWS, TU standards.

The production quality management system complies with ISO 9001 and is certified by the authority of certification of management systems of GLOBAL-CERTIFIC LLC. PrJSC “Dneprometiz” has been granted the right to mark products with the CE mark.

The commissioning of modern production facilities made it possible to expand the product range, satisfy the demand for welding wire and provide the domestic and foreign markets with products of the highest quality. Welding wire produced by “Dneprometiz” successfully competes with the products of European manufacturers in the markets of different countries, thanks to its high reliability and European quality.